TESINA

TÍTOL / TÍTULO

THERMO-HYDRO-MECHANICAL BEHAVIOUR OF YPRESIAN CLAY

AUTOR

PIÑA DIAZ, Yessenia E.

TUTOR

ROMERO MORALES, Enrique
LIMA, Analice

ESPECIALITAT / ESPECIALIDAD

Ingeniería Geotécnica

DATA / FECHA

Barcelona, 11 de Julio de 2011

UPC
Dept. d'Enginyeria del Terreny, Cartogràfica i Geofísica
E.T.S. Enginyers de Camins, Canals i Ports
UNIVERSITAT POLITÈCNICA DE CATALUNYA

UNIVERSITAT POLITÈCNICA DE CATALUNYA

ESCOLA TÈCNICA SUPERIOR D'ENGINYERS DE CAMINS, CANALS I PORTS DE BARCELONA

ETSECCPB

Dept. d'Enginyeria del Terreny, Cartogràfica i Geofísica
E.T.S. Enginyers de Camins, Canals i Ports
UNIVERSITAT POLITÈCNICA DE CATALUNYA

THERMO-HYDRO-MECHANICAL BEHAVIOUR OF YPRESIAN CLAY

MASTER THESIS

IN GEOTECHNICAL ENGINEERING

Presented by: Yessenia E. Piña Diaz

Supervised by: Enrique Romero Morales

Analice Lima

Barcelona, July 2011

To my dear God

and my lovely family

ABSTRACT

Deep geological disposal solution of high-level and long-lived radioactive waste has been internationally recognised as the preferred option. On this regard, Belgium investigates two deep clay formations; the Boom clay at Mol located at around 220 m deep, considered the reference host formation, and recently the Ypresian clay located at around 500 m deep, considered as the alternative one. The main objective of this research is to perform a thermo-hydro-mechanical characterisation of Ypresian clay by a comprehensive experimental program, carried out on undisturbed samples taken from Kallo borehole (370 m deep).

The characterisation program comprised laboratory classification tests, initial total suction and water retention curves (with chilled-mirror dew-point psychrometer), X-ray diffraction, small-strain shear stiffness properties at different orientations (parallel and perpendicular to bedding planes), and mercury intrusion porosimetry (pore size distribution curve of the intact material). Oedometer tests under saturated conditions using step loading and continuous loading approaches were used to characterise the volume change properties of the intact material (yield stress, pre and post-yield compressibility) at different orientations (loading parallel and perpendicular to bedding planes) and at different temperatures (22 and 80 ºC). The material was put in contact with synthetic water at a vertical total stress of 4 MPa (to restore the in situ stress), and then subjected to drained heating (the material underwent some small contraction on this process). The water permeability properties were determined on constant volume and oedometer cells at different orientations (flow parallel and perpendicular to bedding planes) and temperatures (22, 40, 60 and 80 ºC). Temperature cycling effects on water permeability were also examined at constant vertical stress in oedometer cells.

Microstructural changes undergone by the material along the different stress paths followed were analysed by mercury intrusion porosimetry. The microstructural study focused on the double porosity features of the intact material, and how this pore network evolves on loading and heating.

A heating pulse and constant volume equipment was calibrated and upgraded, which included the development of new acquisition software, the adaptation of new pore water pressure transducers, and a new controlled-power cartridge heater. Preliminary results of a heating/cooling pulse test were presented and discussed.

RESUMEN

El almacenamiento geológico profundo como solución en la disposición final de residuos radiactivos de alta actividad y larga vida, ha sido reconocido internacionalmente como la opción preferente. En este sentido, Bélgica investiga dos formaciones geológicas profundas; la arcilla de Boom en Mol ubicada aproximadamente a 220 m de profundidad, considerada la formación de acogida de referencia, y recientemente la arcilla de Ypresian ubicada en torno a 500 m de profundidad, considerada como la formación de acogida alternativa. El principal objetivo de esta investigación es realizar una caracterización termo-hidro-mecánica de la arcilla de Ypresian a través de un completo programa experimental, llevado a cabo en muestras inalteradas extraídas de los sondeos hechos en Kallo (370 m de profundidad).

El programa de caracterización está compuesto por ensayos de laboratorio de clasificación de suelos, succión total inicial y curvas de retención (a través de un psicrómetro de punto de rocío), difracción de rayos X, propiedades de rigidez al corte a pequeñas deformaciones en diferentes orientaciones (paralela y perpendicular a los planos de estratificación) y una porosimetría por intrusión de mercurio (curva de distribución de tamaño de poros del material intacto). Los ensayos edométricos bajo condiciones saturadas utilizando las técnicas de carga continua y por etapas fueron utilizados con el fin de caracterizar las propiedades de cambio de volumen del material intacto (*yield stress, pre and post-yield compressibility*) a diferentes temperaturas (22 y 80 ºC). El material fue puesto en contacto con el agua sintética a una tensión efectiva vertical de 4 MPa (para restablecer la tensión in situ), y posteriormente sometido a un calentamiento drenado (el material sufrió una pequeña contracción en este proceso). Las propiedades de permeabilidad al agua fueron determinadas a volumen constante y en células edométricas a diferentes orientaciones (flujo paralelo y perpendicular a los planos de estratificación) y temperaturas (22, 40, 60 and 80 ºC). Los efectos de los ciclos de temperatura sobre la permeabilidad al agua fueron también examinados a tensiones verticales constantes en células edométricas.

Los cambios microestructurales experimentados por el material a lo largo de las diferentes trayectorias de esfuerzos seguidas fueron analizados mediante porosimetrías por intrusión de mercurio. El estudio microestructural estuvo enfocado en la doble porosidad característica del material intacto y la forma en que esta evoluciona durante los procesos de carga y calentamiento.

Un equipo diseñado para efectuar pulsos de calentamiento a volumen constante fue calibrado y puesto a punto, lo cual incluye el desarrollo de un nuevo programa de adquisición de datos, la adaptación de nuevos transductores de presión de poros y la instalación de una nueva resistencia tipo cartucho controlada por una red de alimentación conectada en serie. Los resultados preliminares de un ensayo con un pulso de calentamiento/enfriamiento son presentados y discutidos.

AGRADECIMIENTOS

El presente trabajo de investigación fue desarrollado dentro del marco del proyecto '*Thermo-Hydro-Mechanical Research on Ypresian clays: Post-Doc for a period of 18 months (NOCA 2009-1027)*' en el período comprendido entre diciembre de 2009 y mayo de 2011; coordinado a su vez por Laurent Wouters (ONDRAF/NIRAS), Xiangling Li (SCK.CEN/EIG EURIDICE) y Enrique Romero (UPC/CIMNE). En este sentido, me gustaría expresar mi agradecimiento a ONDRAF/NIRAS (Belgian Agency for Radioactive Waste and Enriched Fissile Materials) por su financiación durante la ejecución de dichos trabajos. Igualmente a la Dra. Xiangling Li, por sus interesantes discusiones y sugerencias vinculadas a trabajos futuros, expuestas durante las diferentes reuniones celebradas a lo largo del proyecto.

A Enrique Romero, mi tutor, por brindarme la oportunidad de trabajar en este interesante proyecto bajo su coordinación y asesoramiento, la cual ha sido una experiencia sumamente enriquecedora tanto a nivel profesional como personal. De la misma forma a Analice Lima, mi codirectora, por todo su apoyo durante la fase experimental y de interpretación, pero sobre todo por su paciencia, por tomarse el tiempo que fuese necesario para dejar claros los conceptos. A ambos, mi más sincera gratitud.

A todos mis compañeros del laboratorio, quienes realmente comprenden los contratiempos del trabajo experimental y que de alguna manera u otra aligeraron mi carga durante el proceso. En particular a los señores José Álvarez y Víctor Lozano por su ayuda y colaboración durante la preparación de las muestras y ejecución de los ensayos; a Fernando Cortez por su asesoría, en cuanto a electrónica se refiere y a Tomas Pérez, por sus valiosos consejos durante la puesta a punto de la célula de calentamiento.

A mis amigos y compañeros de clase, con los que compartí esa primera etapa del máster llena de asignaturas, trabajos y exámenes. Por los buenos momentos que compartimos dentro y fuera de la universidad, por hacerme sentir que fuera de Venezuela también cuento con otros lugares donde sentirme tan a gusto, como en casa.

A mis padres y a mi Nani querida, por darme siempre el impulso que necesito para llevar a cabo mis proyectos. En especial a mi madre, por ser ese soporte invaluable cuando mi fe flaquea. A mis hermanos y a sus familias, por abrirme las puertas de sus casas durante estos años de estudio, por ser un apoyo en todo sentido y por regalarme tres hermosas razones (Aarón, Miranda y Salomón) por las que disfrutar aun más mi estancia fuera de casa. También me gustaría agradecer a mi prima Katy, quien desde mi llegada a España busco ayudarme en todo cuanto pudo, más que una prima ha sido como una hermana.

Y finalmente, pero sin duda alguna no menos importante, mi eterna gratitud va dirigida a aquel que guía y sustenta mi destino, a mi amado Dios, por hacer siempre de mis sueños una continua realidad.

TABLE OF CONTENTS

LIST OF FIGURES xiv

CHAPTER 1 INTRODUCTION 1
1.1. BACKGROUND 1
1.2. OBJECTIVES 2
1.3. MASTER THESIS LAYOUT 2

CHAPTER 2 STATE OF THE ART 5
2.1. INTRODUCTION 5
2.2. GEOLOGICAL AND GEOGRAPHICAL FRAMEWORK 6
2.2.1. Stratigraphy and lithology 6
2.2.2. Geographical distribution 7
2.3. PHYSICAL PROPERTIES AND BASIC CHARATERISATION 8
2.3.1. Grain size 8
2.3.2. Mineralogical composition 13
2.3.2.1. Bulk mineralogy 13
2.3.2.2. Cation exchange capacity 16
2.3.2.3. Clay mineralogy 16
2.3.3. Basic geotechnical characterization 19
2.4. HYDRAULIC PROPERTIES 22
2.5. GEOMECHANCIAL PROPERTIES 23
2.6. THERMAL PROPERTIES 24

CHAPTER 3 MATERIAL USED IN THE INVESTIGATION 27
3.1. INTRODUCTION 27
3.2. ORIGIN OF THE MATERIAL AND MINERALOGY 27
3.2.1. Origin of the material 27
3.2.2. X-ray diffraction analysis 29
3.3. GEOTECHNICAL CLASSIFICATION TESTS 30
3.4. GEOTECHNICAL PROPERTIES BASED ON PREVIOUS REPORTS 31

CHAPTER 4 EXPERMIENTAL TECHNIQUES AND PROTOCOLS 33
4.1 INTRODUCTION 33
4.2 MERCURY INTRUSION POROSIMETRY TEST 34
4.2.1. Brief description of the equipment 34
4.2.2. Test protocol 35
4.3 WATER RETENTION CURVE FROM PSYCHROMETER MEASUREMENTS TEST 35
4.3.1. Brief description of the equipment 35
4.3.2. Test protocol 36
4.4 RESONANT COLUMN TEST 37
4.4.1. Brief description of the equipment 37
4.4.2. Test protocol 38
4.5 BENDER ELEMENTS TEST 38
4.5.1. Brief description of the equipment 38

4.5.2. Test protocol 39
4.6 ULTRASONIC PULSE TEST 40
4.6.1. Brief description of the equipment 40
4.6.2. Test protocol 40
4.7 CONTROLLED-GRADIENT WATER PERMEABILITY TESTS AT DIFFERENT TEMPERATURES USING CONSTANT VOLUME CELLS 41
4.7.1. Brief description of the equipment 41
4.7.2. Test protocol 43
4.8 CONTROLLED-GRADIENT WATER PERMEABILITY TESTS AT DIFFERENT TEMPERATURES USING THE OEDOMETER CELL 43
4.8.1. Brief description of the equipment 43
4.8.2. Test protocol 44
4.9 STEP-LOADING/UNLOADING OEDOMETER TEST 45
4.9.1. Brief description of the equipment 45
4.9.2. Test protocol 46
4.10CONTINUOUS LOADING/UNLOADING OEDOMETER TESTS 46
4.10.1. Brief description of the equipment 46
4.10.2. Test protocol 47
4.11PULSE HEATING TEST 48
4.11.1. Brief description of the existing equipment 48
4.11.2. Update performed on the cell 49
4.11.3. Test protocol 50

CHAPTER 5 EXPERIMENTAL RESULTS 53
5.1. MERCURY INTRUSION POROSIMETRY RESULTS 53
5.2. WATER RETENTION CURVE 57
5.2.1. Chilled-mirror dew-point psychrometer results 57
5.2.2. MIP-retention curve relationship 58
5.3. WATER PERMEABILITY RESULTS 59
5.3.1. Water permeability results from samples tested under constant volume condition 59
5.3.2. Water permeability results from samples tested under a constant vertical stress 60
5.4. STIFFNESS MODULI 62
5.4.1. Low-strain shear modulus 62
5.4.1.1. Resonant column results 62
5.4.1.2. Bender elements results 63
5.4.2. Young modulus under unloaded consdition 63
5.5. THERMO-HYDRO-MECHANICAL OEDOMETER RESULTS 64
5.5.1. Step-loading/unloading results 64
5.5.2. Continuous loading/unloading results (T=22 and 80ºC) 70
5.6. THERMO-HYDRAULIC HEATING CELL RESULTS 77
5.6.1. Hydration phase 77
5.6.2. Heating and cooling phases 80
5.7. MICROSTRUCTURAL CHANGES INDUCED ON THE DIFFERENT LOADING PATHS FOLLOWED 82
5.8. COMPARISON BETWEEN GEOTECHNICAL PROPERTIES OBTAINED IN THIS RESEARCH AND PREVIOUS REPORTS 84

CHAPTER 6 SUMMARY, CONCLUSIONS AND FUTURE RESEARCH WORK 87
6.1. SUMMARY AND CONCLUSIONS…….....87
6.1.1. Initial geotechnical characterisation of the material 87
6.1.2. General hydraulic and mechanical characterisation…….....87
6.1.3. Hydro-mechanical characterization under oedometer conditions…….....88
6.1.4. Thermo-hydraulic characterisation…….....88
6.1.5. Microscopic analysis…….....89
6.2. FUTURE RESEARCH WORKS 89

REFERENCES 91

APPENDIX A 93
APPENDIX B 103

LIST OF FIGURES

Figure 2.1 Chronostratigraphic position of the lithoestratigraphic units from the Ieper group and correlation with the surrounding areas 6

Figure 2.2 Lithostratigraphic subdivision of the Ypresian according to Steurbaut (1998). ...7

Figure 2.3 Subdivision of the depositional area of the Ieper Group in lithological and delineation of the investigation area....8

Figure 2.4 Grain size distribution in Knokke (a), Tielt (b) and Kallo (c) wells 9

Figure 2.5 Grain size distribution in the Mol well. 9

Figure 2.6 Grain size distribution of some samples from the Ypresian clay sequence in the Doel-1A well 10

Figure 2.7 Variations with stratigraphic position in SR, CR and skewness throughout the Ypresian clay sequence in the Doel-1 A well 11

Figure 2.8 Typical size distribution curves representing the six classified groups of Kallo samples 13

Figure 2.9 Distribution of carbonate, organic matter, iron content and the fraction greater than 50 µm in the cored section of Ypresian clays from borehole Doel-1A analysed by LTGH....14

Figure 2.10 Distribution of carbonate, feldspar and quartz contents in the silt fraction of Ypresian clays from borehole Doel-1A analysed by LTGH....14

Figure 2.11 Clay mineralogy in the clay fraction of Ypresian clays from borehole Doel 1-A analysed by LTGH 16

Figure 2.12 Clay mineralogy in the silt fraction of the Ypresian clays from borehole Doel 1-A analysed by LTGH....17

Figure 2.13 Clay mineralogy of the Ypresian Clay along an East-West section through the Belgian Basin....19

Figure 2.14 Incremental pore area of Ypresian clay from Doel samples obtained by INISMa 21

Figure 3.1 Packing of the Kallo samples delivered to UPC Laboratory....28

Figure 3.2 X-ray diffraction of the studied material 29

Figure 3.4 Situation map of Doel and Kallo towns in Belgium 32

Figure 4.1 Scheme of sample coring and preparation....34

Figure 4.2 Mercury intrusion porosimetry equipment 34

Figure 4.3 WP4-T equipment and sample 36

Figure 4.4 Resonant column equipment....38

Figure 4.5 Bender elements testing equipment 39

Figure 4.6 Drilling equipment and sample 40

Figure 4.7 Ultrasonic pulse test equipment and sample 41

Figure 4.8 Constant volume cell pieces 42

Figure 4.9 Controlled-gradient water permeability setup 42

Figure 4.10 Thermal bath for water permeability determinations at different temperatures 43

Figure 4.11 Experimental layout of the equipment used to perform water permeability tests 44

Figure 4.12 Set-up of the equipment used to perform step loading/unloading oedometer tests 46

Figure 4.13 Scheme of the temperature and suction controlled oedometer cell (Lima et al., 2010) 47

Figure 4.14 Set-up of the equipment used to perform continuous loading/unloading oedometer tests 47

Figure 4.15 Scheme of the existing heating cell (Lima et al, 2010).....49

Figure 4.16 Adapters and transducers. (a) Schematic representation after Pérez (2010). (b) Photographs of the different connectors 50

Figure 4.17 Set-up of the equipment used to perform heating pulse test 50

Figure 5.1 Pore size density function of undisturbed sample 53

Figure 5.2 Pore size density functions of the air dried sample compared to the freeze dried sample 54

Figure 5.3 Pore size density functions of the material after undergoing different stress paths. The reference undisturbed test is included for comparison 56

Figure 5.4 Cumulative void ratio during intrusion/extrusion cycle for the undisturbed sample 57

Figure 5.5 Water retention curve from psychometric measurements 58

Figure 5.6 Water retention curve estimated from MIP data 59

Figure 5.7 Vertical (k_{wv}) and horizontal (k_{wh}) water permeability results obtained from samples tested in the isochoric cell.....60

Figure 5.8 Vertical controlled-gradient water permeability measured during different temperatures under constant effective stress of 4MPa 61

Figure 5.9 Horizontal controlled-gradient water permeability measured during different temperatures under constant total stress of 20 MPa 61

Figure 5.10 Variation of shear modulus G_0 with stress level at vertical and horizontal sample directions 63

Figure 5.11 Step-loading/unloading paths at vertical sample orientation (room temperature).....65

Figure 5.12 Step-loading/unloading paths at horizontal sample orientation (room temperature).....65

Figure 5.13 Step-loading/unloading/reloading on horizontal sample orientation (vertical bedding planes) 66

Figure 5.14 Comparison between vertical and horizontal sample orientations in step-loading/unloading tests 66

Figure 5.15 Cumulative work input per unit volume versus logarithm of total(net)/effective stress in step loading/unloading oedometer tests 67

Figure 5.16 Time evolution of soil deformation on loading stages performed with water contact and known pressure in both vertical and horizontal orientations 68

Figure 5.17 Water permeability under saturated conditions measured during oedometer tests for vertical and horizontal orientations (constant vertical effective stress of 4 MPa and at room temperature) 69

Figure 5.18 Comparison between water permeability results measured and those estimated from consolidation back-analysis 70

Figure 5.19 Continuous loading/unloading paths at vertical sample orientation (room temperature) 71

Figure 5.20 Comparisons between vertical and horizontal sample orientations in continuous loading/unloading tests 71

Figure 5.21 Comparisons between step-loading/unloading and continuous loading/unloading tests: (a) vertical sample and (b) horizontal sample orientation 72

Figure 5.22 Continuous loading/unloading paths on vertical sample orientation at 80ºC..73

Figure 5.23 Continuous loading/unloading paths on horizontal sample orientation at 80ºC 74

Figure 5.24 Comparisons between vertical and horizontal sample orientations in continuous loading/unloading tests at 80ºC 74

Figure 5.25 Volume change response during drained heating on vertical and horizontal sample orientations.....75

Figure 5.26 Comparisons between continuous loading/unloading tests at 22ºC and 80ºC: (a) vertical sample and (b) horizontal sample orientation 76

Figure 5.27 Cumulative work input per unit soil volume versus logarithm of the net(total)/effective stress for the whole oedometer program 76

Figure 5.28 Hydration phase with upper valve open. (a) Time evolution of temperature. (b) Time evolution of pore water pressures at different locations 78

Figure 5.29 Time evolution of (a) water inlet and (b) outlet volumes under steady-state conditions (u_w = 1MPa at the bottom).....79

Figure 5.30 Hydration phase-upper valve closed. (a) Time evolution of temperature. (b) Time evolution of pore water pressures at different locations 80

Figure 5.31 Heating and cooling phases. (a) Time evolution of temperature at different locations. (b) Time evolution of pore water pressures at different locations (u_w = 1.2 MPa at the bottom boundary).....81

Figure 5.32 Heating and cooling phases. (a) Time evolution of temperature at different locations. (b) Time evolution of pore water pressures at different locations (u_w = 1.2 MPa at the bottom boundary). 82

Figure 5.33 MIP comparisons between two samples loaded to an vertical effective stress of 20 MPa and then extracted following different procedures (with water inlet or with valve closed) 83

Figure 5.34 MIP comparisons of samples consolidated to different effective vertical stresses 83

CHAPTER 1

INTRODUCTION

1.1 BACKGROUND

An important and latent problem in modern society is the management and disposal of radioactive wastes. This type of waste is classified according to the level of activity, which is directly related to the potential hazard. In the case of high-level and long-lived wastes, it is necessary to keep them isolated and confined from man and his environment for long periods of time.

Nowadays, the disposal in deep geological repositories is internationally recognised as the preferred option for the management of high-level and long-lived wastes. This alternative is based on a multi-barrier concept, which consists in an integrated system of natural and engineered barriers used to prevent and delay radionuclide migration into the surrounding environment. According to the International Atomic Energy Agency report (IAEA, 2001): the natural barriers include the host rock and surrounding geological formations, with their structural, hydrogeological and geochemical characteristics, whereas the engineered barriers system (EBS) includes among others the conditioned waste form, the waste package and its potential overpack, the backfill, buffer and seal materials.

Based on international experience, the Belgian Nuclear Research Centre (SCK.CEN), the Belgian Geological Survey and the Belgian Agency for Radioactive Waste and Enriched Fissile Materials (ONDRAF/NIRAS) showed particular interest in clay formations, especially in Boom clay, located under the nuclear site of Mol-Dessel at an approximate depth of 220 m. In the early eighties, SCK.CEN initiated a comprehensive research program to evaluate Boom clay potentiality for geological storage of high level nuclear waste. However, recent researches have demonstrated the feasibility of minimising the exposure and increasing safety by installing the repositories at greater depths. It is the case of Finland, France, Germany, Sweden and other countries around the world, which have been assessing this alternative, including laboratory tests, exploratory boreholes, and the construction and operation of underground research laboratories (URLs) in which large-scale in-situ tests are being conducted. Table 1.1 summarises some of the operating URLs.

In view of the aforementioned interest in deeper clay formations, in the mid-nineties ONDRAF / NIRAS considered the Ypresian clay, an argillaceous formation located in the Doel nuclear zone (Belgium) at around 500 m depth, as an alternative host formation for the research and assessment of a deep disposal solution for high-level and long-lived radioactive wastes. Since this clay formation began to be investigated, studies have been focused on in-situ tests, mineralogical analysis, chemical analysis, permeability and migration tests, among others. Nevertheless, the coupled thermo-hydro-mechanical properties of the material based on laboratory tests performed on undisturbed samples have been little studied, which is the main objective of the present research study.

Table 1.1 Main operating URLs around the world (IAEA, 2001).

Country	Region	Facility Name	Host rock/Geological formation	Depth (m)	Status
Belgium	Mol	HADES Underground Research Facility	Boom clay (Rupelian, Lower Oligocene)	223	in operation since 1980
Canada	Pinawa, Manitoba	Lac Du Bonnet Underground Research Laboratory	Granitic pluton; Lac Du Bonnet Batholith	240-420	in operation since 1984
Finland	Olkiluoto	ONKALO	Granite	400	in operation since 1993
France	Bure	Meuse/Haute Marne Underground Research Laboratory	Callovo-Oxfordian argillites	500	in operation since 2000
Sweden	Äspö	Äspo Hard Rock Laboratory	Småland granite (Precambrian)	450	in operation since 1990
Switzerland	Bern Canton	Grimsel Test Site	Central Aar Granite	450	in operation since 1983
Switzerland	Jura Canton	Mont Terri Rock Laboratory	Shale, Opalinus Clay (Lower Aalenian, Dogger)	300	in operation since 1995
USA	Carlsbad, New Mexico	Waste Isolation Pilot Plant	Permian Salado Formation (~214 million years old)	655	in operation since 1982

1.2 OBJECTIVES

The main objective of this research is the study of the thermo-hydro-mechanical behaviour of intact Ypresian clay by a comprehensive experimental and characterisation program.

The research has been divided into four different stages, which would together achieve the overall goal of the investigation. These stages are briefly described below:

- Initial stage of documentation and compilation of available information related to the thermo-hydro-mechanical behaviour of the geologic formation under study.
- Upgrading instruments and laboratory equipment, which will be used in the experimental phase; calibrations of new and existing cells.
- Performing a comprehensive experimental program, which include the characterisation of the material (also from a microstructural viewpoint) and carrying out thermo-hydro-mechanical tests using innovative cells.
- Analysis and interpretation of the results.

1.3 MASTER THESIS LAYOUT

The master thesis is organized in six chapters. The content of each chapter is summarised below:

- Chapter 1. Introduction. It outlines the background of the research and its objectives.
- Chapter 2. State of the art of Ypresian clay. It is related to its THM characterisation.
- Chapter 3. Material used in the investigation. It describes the main properties of the tested material within the context of the results presented in Chapter 2.
- Chapter 4. Experimental techniques and protocols. Presents the layout of the experimental program and the description of the testing protocols followed.
- Chapter 5. Experimental results. Presents the experimental results and their interpretation.
- Chapter 6. Summary, conclusions and future research work. This chapter presents a summary of the research, the conclusions drawn and future research proposals.

CHAPTER 2

STATE OF THE ART OF YPRESIAN CLAY

2.1 INTRODUCTION

This chapter is presented as a compendium of available and updated information, which is directly related to the thermo-hydro-mechanical behaviour of Ypresian clay. This information is used as a reference or starting point for the development of this research, for further analysis of the results and for drawing final conclusions.

This state of the art can be divided into two main sections. The first one, associated with the geological and geographical framework of the clay formation, and the second one with the presentation and discussion of the geotechnical properties of Ypresian clay.

The interest in studying the Ypresian clay formation is relatively recent. The information available before being considered an alternative host formation for radioactive waste disposal was limited and scattered. The Laboratory for Applied Geology and Hydrogeology (LTGH) of the University of Ghent gathered and synthesised this information on behalf of ONDRAF/NIRAS in its 94/30 technical report (1996).

In 1997 and 1998 ONDRAF/NIRAS conducted an exploration program on a site near the Doel nuclear power station, which made possible to obtain a comprehensive database that enables to perform an extensive analysis of Ypresian clay. Samples taken from this campaign were delivered to different organisms and institutions as part of a multidisciplinary analysis. The Laboratory for Applied Geology and Hydrogeology (LTGH, Ghent University, Belgium), the Schlumberger-Doel Research (SDR, Ridgefield, USA), the Institut National Interuniversitaire de Silicates sols et Matériaux (INISMa, Mons, Belgium), the Laboratoire du Gènie Civil (LGC, Katholieke Universiteit Leuven, Belgium) and the Belgian Nuclear Research Centre (SCK.CEN) were the responsible for conducting these analyses. The distribution of samples is presented in Table 2.1.

Table 2.1 Distribution of the samples for the different analyses (T-H-P: thermal, hydraulic and petrophysical).

Stratigraphy	Mineralogy		Geochemistry		T-H-P	Geomechanics	Migration test
	LTGH	SDR	LTGH	SDR	INISMa	LGC	SCK-CEN
Kortemark	4	1	2	1	2	-	25
Aalbeke	3	1	2	1	2	1	
Roubaix	31	3	15	3	15	6	
Orchies	12	2	6	2	6	3	

The documentation and interpretation of the data from this research program was summarised and published by Van Marcke and Laenen (2005).

In addtion, recent studies in terms of grain size and mineralogy, conducted by Katholieke Universiteit Leuven (KULeuven report, 2011), are also available, specifically for the Kallo area.

2.2 GEOLOGICAL AND GEOGRAPHICAL FRAMEWORK

2.2.1 Stratigraphy and lithology

The Ypresian is the lowest stratigraphy stage of the Eocene, which comprises a period of time between 49.6 and 55 million years ago (Fig. 2.1).

The sediments of the Ieper group were deposited during the Ypresian; this is the reason why clays deposited during this period are referred to as the Ypresian clay formation, a term that groups the Kortrijk formation and the Kortemark member of the overlying Tielt formation, which also contains silty clay.

The clays represent the lower part of the Ieper group, a sequence of predominantly marine sediments comprised between the continental deposits at the top of the Landen group and the sandy deposits of the Zenne group.

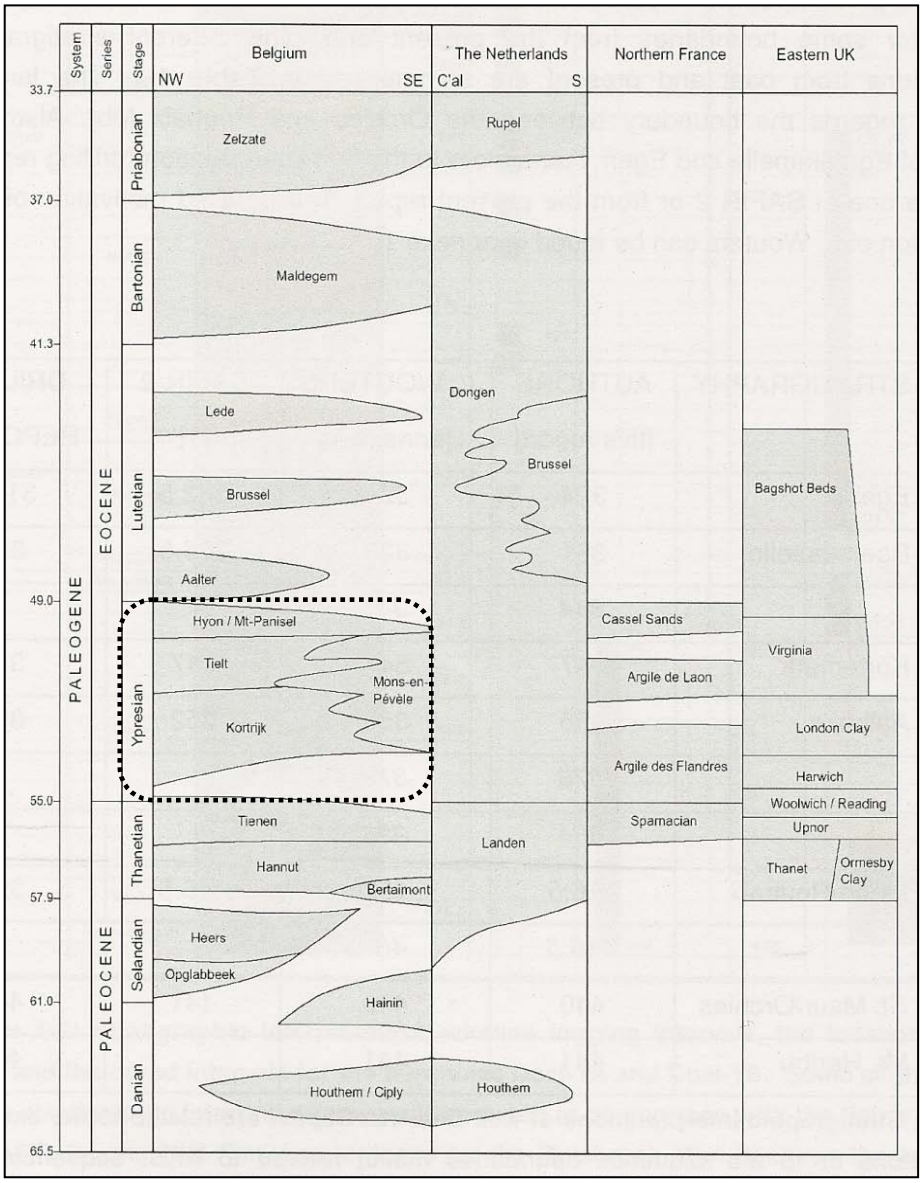

Figure 2.1 Chronostratigraphic position of the lithoestratigraphic units from the Ieper group and correlation with the surrounding areas (enclosed area is enlarged in Fig. 2.2).

According to a recent review of the Belgian lithostratigraphy presented by Steurbaut (1998) (cited in Van Marcke and Laenen (2005)), the Ieper group is subdivided into four formations as shown in Figure 2.2.

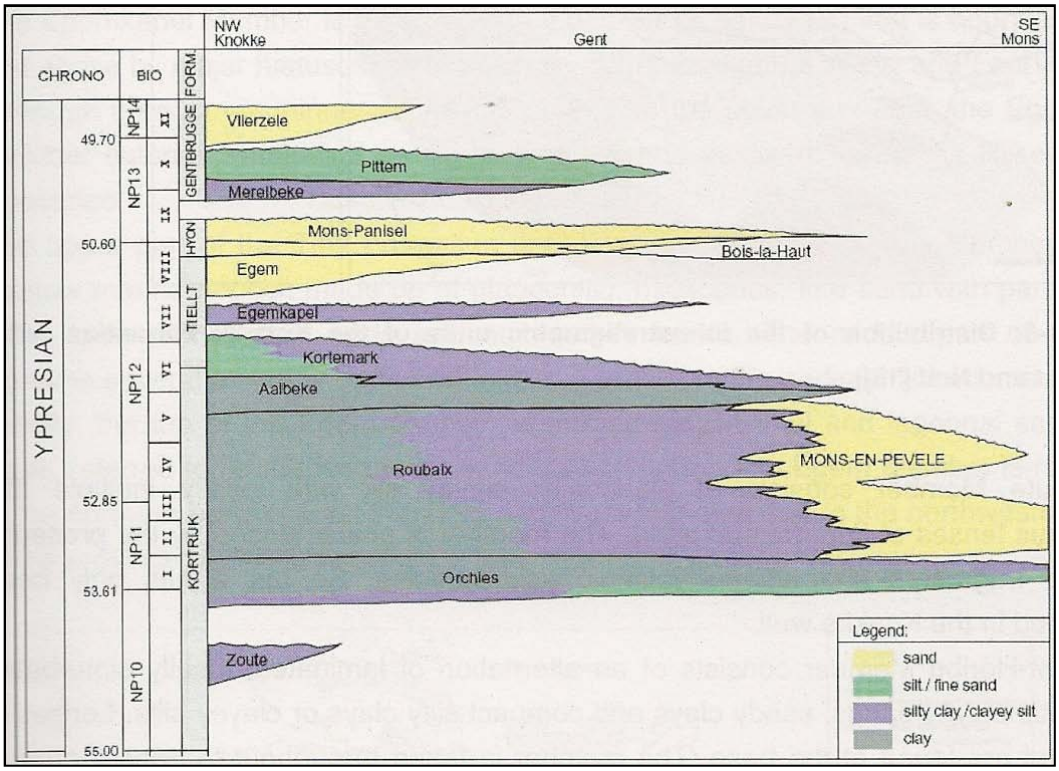

Figure 2.2 Lithostratigraphic subdivision of the Ypresian according to Steurbaut (1998).

The Kortrijk formation, the deepest one, is a predominantly clayey deposit that was formed in a marine environment. The Kortrijk formation is subdivided further into five members, as indicated in Figure 2.2.

The Tielt formation, constituted mainly of silts and sands, is a heterogeneous lithostratigraphic unit of mid-Ypresian age that is subdivided into three members.

The Hyon formation is a unit composed of fine glauconitic and clayey, poorly sorted, bioturbated sands. The Hyon formation is subdivided in a lower, better sorted, claypoor unit, the Bois-la-Haut member, and an upper, poorly sorted, clayey unit with shell and nummulites beds and poorly cemented sandstone layers, the Mont-Panisel member.

The Gentbrugge formation, subdivided into three members, is essentially constituted of marine clayey sediments in the lower part that gradually pass into shallow marine, fine sands. Locally, the top is formed by coastal to lagoonal, glauconitic sands and clays.

2.2.2 Geographical distribution

Since the different transgressions did not extend to the same scale, the succession of the different members and their composition varies from place to place. Based on the presence or absence of certain units and variations in the lithology, the depositional area of the leper group can be subdivided into five subareas (Fig. 2.3).

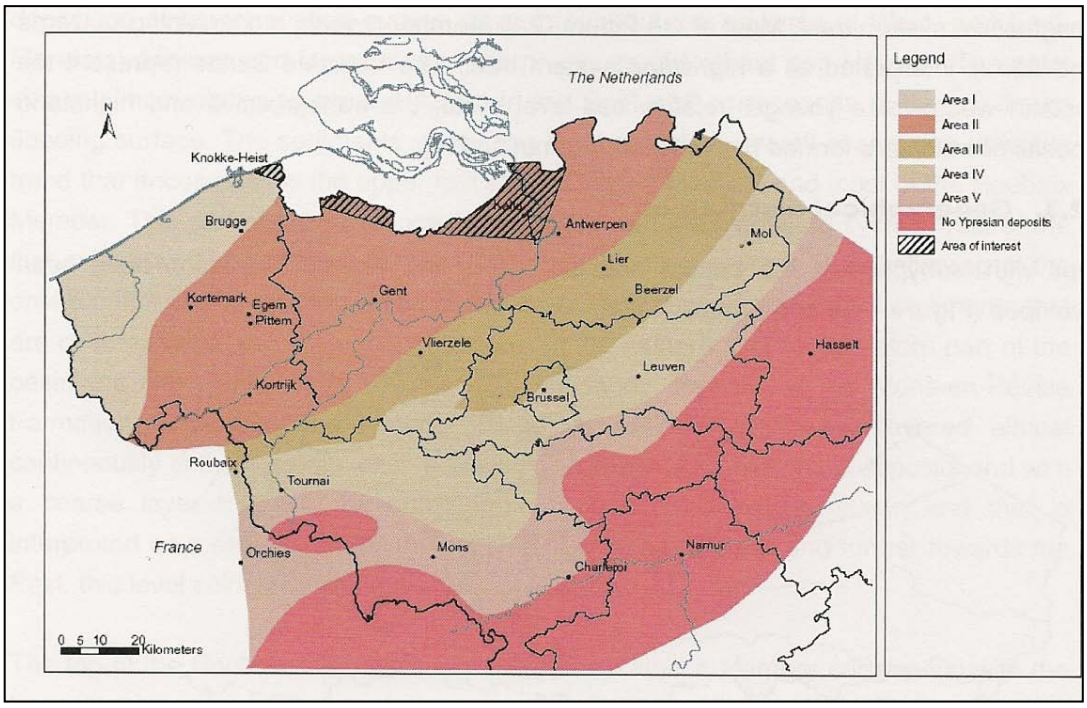

Figure 2.3 Subdivision of the depositional area of the Ieper Group in lithological and delineation of the investigation area.

The hatched area, denominated as "area of interest", was the one selected to focus on the study of the formation within the context of deep disposal of radioactive waste. This area was selected by considering the geometric criteria defined by the ”European Catalogue of geological Formations having Favourable Characteristics for the disposal of solidified high-level and/or long-lived Radioactive Wastes, vol. 2 Belgium” (referred in Van Marcke and Laenen, 2005).

Specifications for the extension and characteristics of these five subareas are found in more detail in Van Marcke and Laenen (2005).

2.3 PHYSICAL PROPERTIES AND BASIC CHARACTERISATION

2.3.1 Grain size

Figures 2.4 and 2.5 presented below, graphically summarise the results of sedimentological analysis performed on areas I, II and III of the Kortrijk formation (Fig. 2.3) presented by Geets in 1988 (cited by LTGH, 1996, report 94/30). Representative wells for each studied area are the following: the Knokke well for area I (Fig. 2.4-a), the Tielt well on West (Fig. 2.4-b) and the Kallo well on East (Fig. 2.4-c), both for area II, and finally the Mol well for area III (Fig. 2.5). In general, the sediment coarsens from West to East and from North to South. EscucharLeer fonéticamente

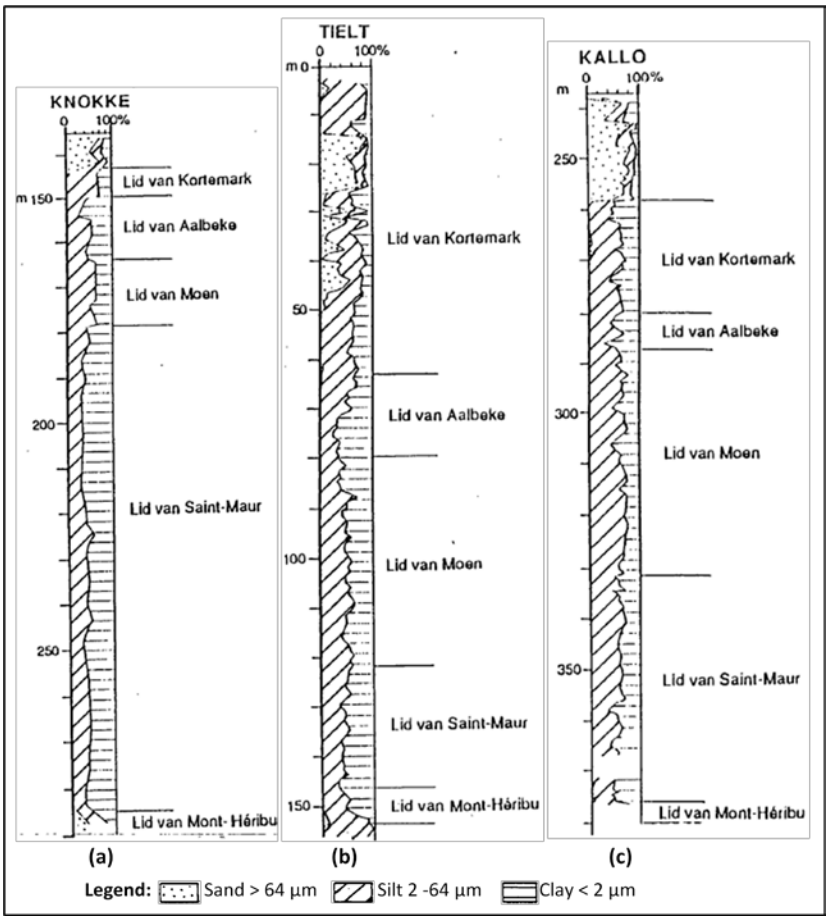

Figure 2.4 Grain size distribution in Knokke (a), Tielt (b) and Kallo (c) wells.

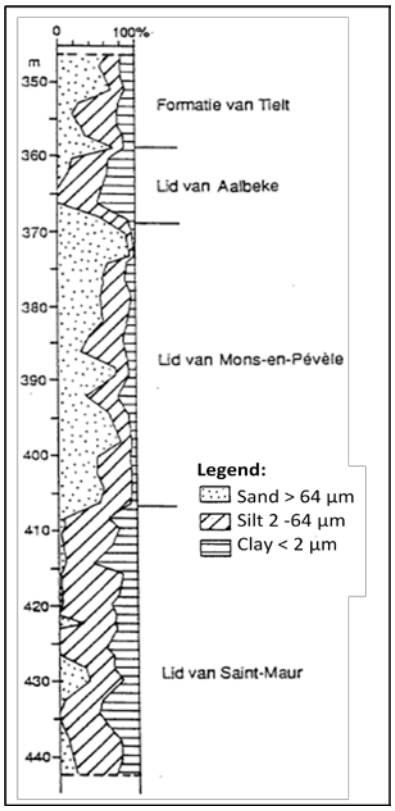

Figure 2.5 Grain size distribution in the Mol well.

According to Van Marcke and Laenen (2005), the detrital fraction of the Ypresian clay sequence can be divided into three different grain size populations: a clay population, a silt to very-fine sand population and a population in the very fine sand to fine sand range. The grain size distribution is indicated in Figure 2.6 for Doel-1A well.

In order to explain the differences between the silty and clayey samples in terms of grain size and based on Figure 2.6, in which the most notable characteristics are the relative contributions of the clay and silt populations and the position of the silt population maximum; Van Marcke and Laenen (2005) used the clay ratio (CR) and the silt ratio (SR). The clay ratio (CR) is the relative contribution of clay-sized particles (< 2 µm) to the detrital sediment population. The silt ratio (SR) is defined as the ratio of the percent contribution of the fraction between 16 µm and 63 µm over the percent contribution of the fraction between 2 µm and 16 µm. SR records the position of the frequency maximum of the silt population.

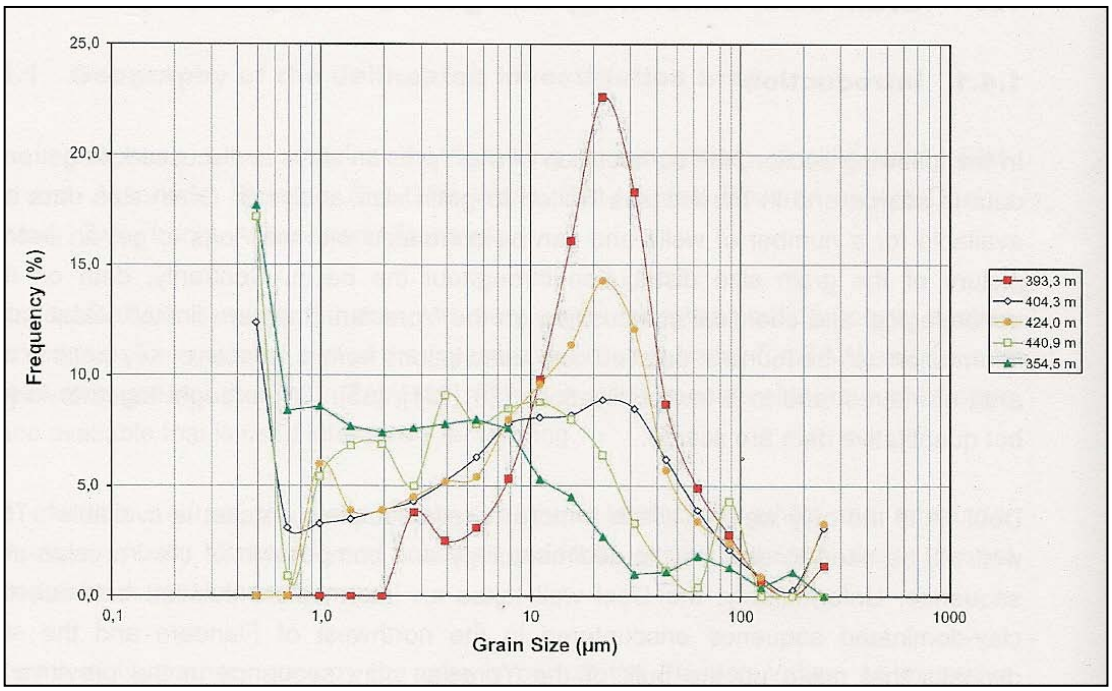

Figure 2.6 Grain size distribution of some samples from the Ypresian clay sequence in the Doel-1A well.

Figure 2.7 shows the variation with depth of CR and SR for the Ypresian clay sequence in the Doel-1A well.

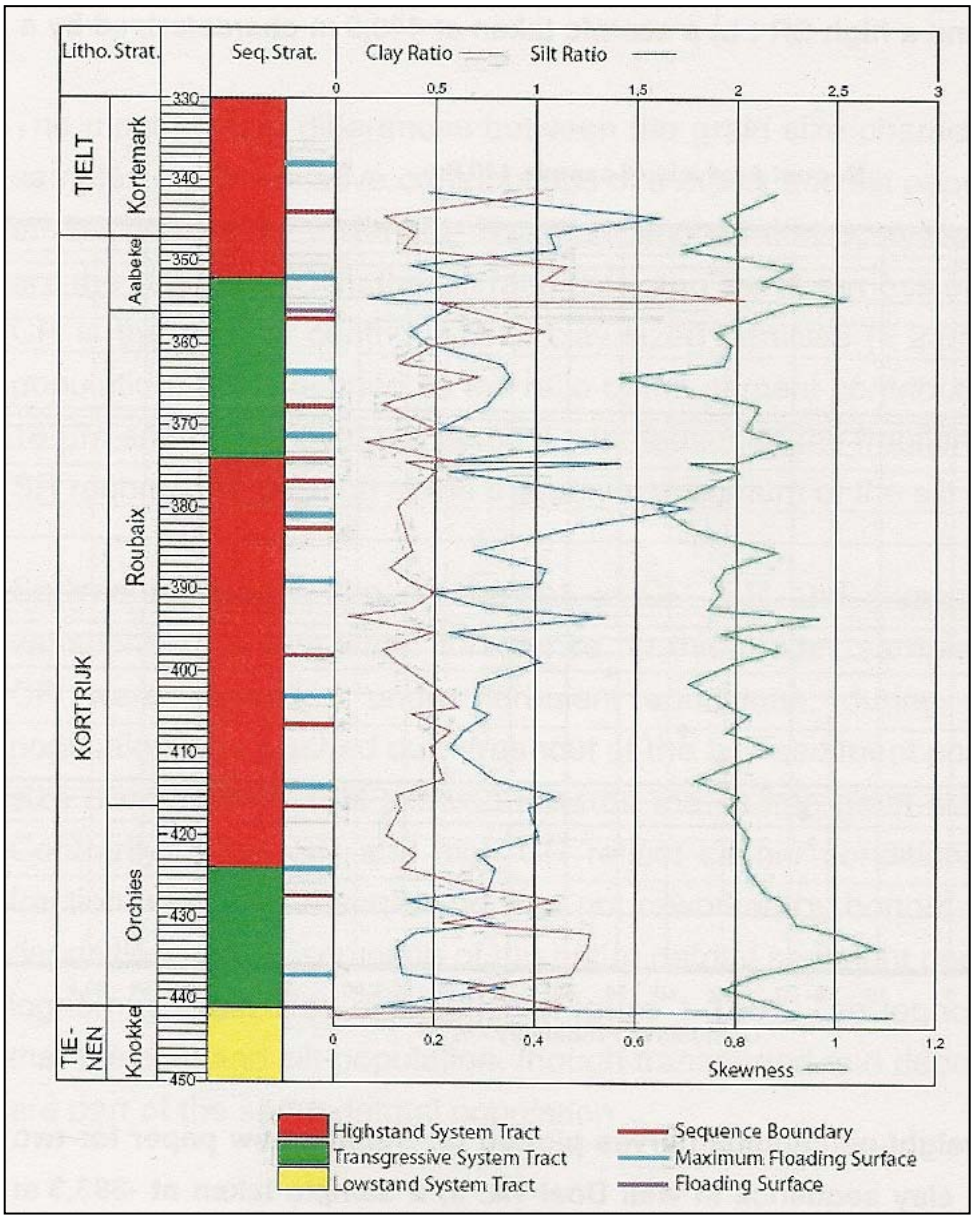

Figure 2.7 Variations with stratigraphic position in SR, CR and skewness throughout the Ypresian clay sequence in the Doel-1 A well.

In relation to the study conducted by KULeuven (report, 2011) on Kallo well (Kallo-1 and Kallo-2), samples were taken from an interval of depth between 259-406 m and tested for grain size analysis using three different methodologies.

The grain size distribution was estimated using the Sedigraph, sieve and Low Angle Laser Light Scattering (LALLS) techniques.

The percentages of sand, silt and clay are also used to identify the texture of the sediments and according to the analysis they belong to six different classes indicated in Table 2.2.

Table 2.2 Granulometric composition according to the textural group of Kallo samples.

Textural group	Sample Nº	Sand 63µm-2mm (%)	Silt 2-63µm (%)	Clay <2µm (%)
Silty clay	Kallo-2 (259.74-259.80 m)	1.18	43.45	55.37
	Kallo-1 (314.47-314.59 m)	0.43	40.47	59.10
	Kallo-1 (322.47-322.59 m)	0.50	45.57	53.93
	Kallo-1 (331.42-331.54 m)	0.28	44.25	55.48
	Kallo-1 (341.35-341.47 m)	0.05	43.79	56.16
	Kallo-1 (350.35-350.47 m)	0.23	43.30	56.46
	Kallo-1 (361.23-361.35 m)	0.06	38.69	61.26
	Kallo-1 (373.07-373.19 m)	1.72	43.56	54.72
	Kallo-1 (382.95-383.07 m)	0.35	26.32	73.33
	Kallo-1 (387.95-388.07 m)	1.94	30.55	67.51
Clay	Kallo-1 (391.91-392.03 m)	0.12	23.16	76.72
	Kallo-1 (396.75-396.87 m)	0.62	23.42	75.96
	Kallo-1 (399.73-399.85 m)	6.98	14.78	78.24
Clayey sand	Kallo-2 (263.73-263.79 m)	57.89	7.52	34.59
	Kallo-1 (400.74-400.86 m)	57.11	12.61	30.28
Clayey silt	Kallo-1 (293.44-293.56 m)	0.82	51.45	47.72
	Kallo-1 (302.82-302.88 m)	2.56	52.02	45.42
	Kallo-1 (405.89-405.95 m)	22.03	54.78	23.19
Silty mud	Kallo-2 (270.70-270.76 m)	32.01	49.56	18.43
Silty sand	Kallo-2 (279.71-279.77 m)	56.48	37.17	6.35
Maximun		57.89	54.78	78.24
Mínimum		0.05	7.52	6.35
Average		12.17	36.32	51.51

The results of the typical size distribution curves are illustrated in Figure 2.8, in which six different groups of materials were considered.

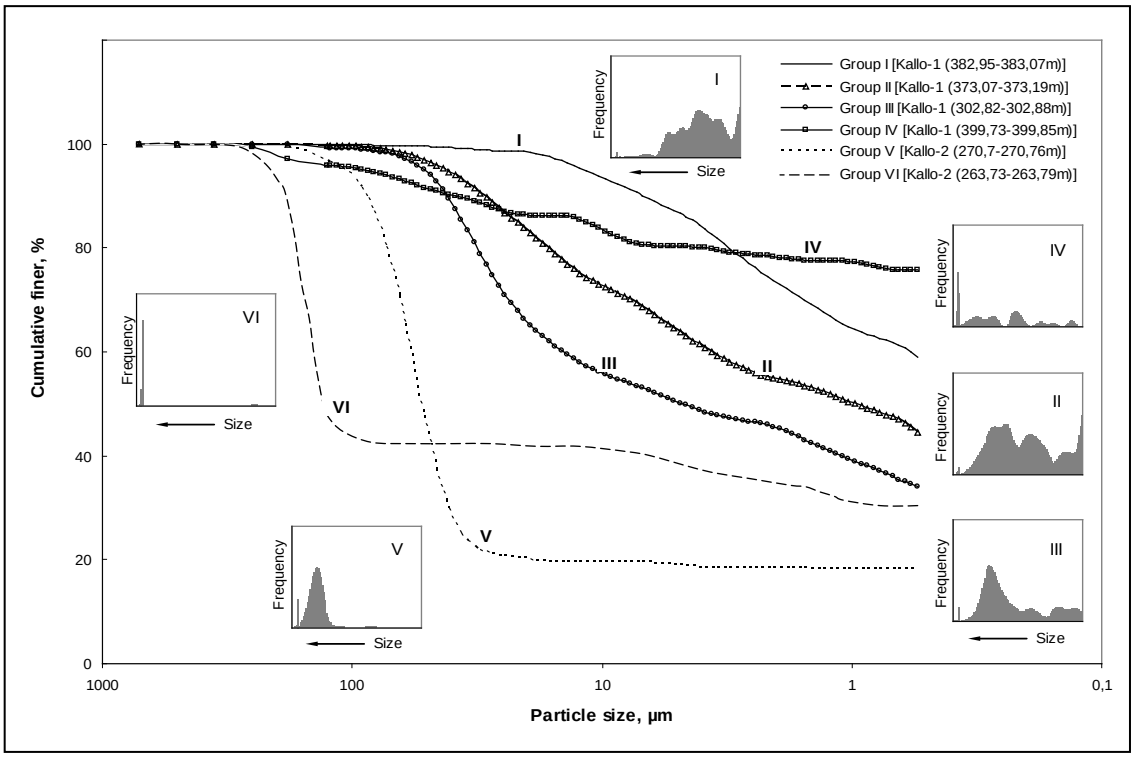

Figure 2.8 Typical size distribution curves representing the six classified groups of Kallo samples.

2.3.2 Mineralogical composition

Samples taken at Doel-1A area were sent for analysis of the mineralogical composition of the Ypresian to LTGH and Schlumberger – Doll Research (SDR). It is necessary to clarify that only results provided by SDR are representative of the whole Ypresian clay mineralogy, because the analysis was conducted on the entire sediment (Van Marcke and Laenen, 2005).

For the Kallo area, the Laboratory for Applied Geology and Mineralogy of the Katholieke Universiteit Leuven analysed the bulk mineralogy, the cation exchange capacity and the clay mineralogy of different samples taken from Kallo-1 between 293-401 m depth.

Below, some of the results from the analyses mentioned above, as well as data from wells in other locations within the Belgian basin, are presented.

2.3.2.1. Bulk mineralogy

The results obtained by the analysis performed by LTGH using x-ray diffraction (XRD) and point-counting techniques are synthesised in Figures 2.9 and 2.10.

The level of carbonate In the Kortrijk Formation is predominantly less than 2%, except for the central section of the Roubaix Member, where values rise over 5%. The content of organic matter is quite low and evenly distributed. Only the basal parts of the Orchies and Aalbeke members show somewhat higher values (Fig. 2.9).

The grain size fraction between 2 µm and 50 µm ("silt fraction") can be subdivided in phyllosilicates on one hand and quartz, feldspars, small fossil fragments and a suite of

secondary and trace minerals including glauconite, apatite, pyrite and other heavy minerals on the other hand. The most important phyllosilicates are illite, kaolinite, smectite and chlorite (Fig. 2.10)

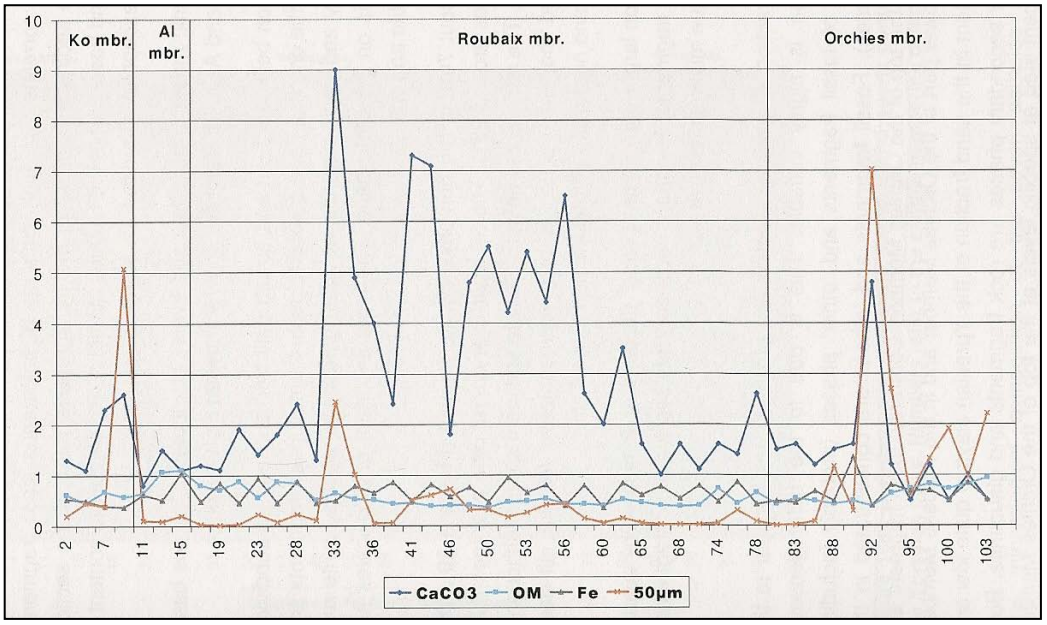

Figure 2.9 Distribution of carbonate, organic matter, iron content and the fraction greater than 50 µm in the cored section of Ypresian clays from borehole Doel-1A analysed by LTGH.

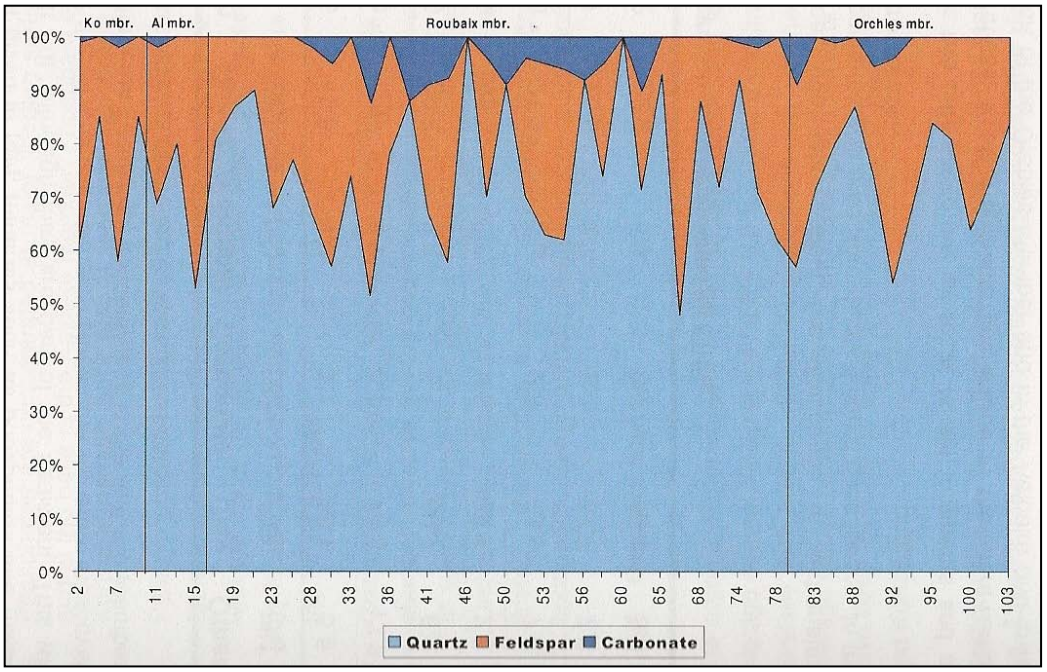

Figure 2.10 Distribution of carbonate, feldspar and quartz contents in the silt fraction of Ypresian clays from borehole Doel-1A analysed by LTGH.

The grain size fraction larger than 50 µm ("sand" fraction) is dominated by quartz, feldspars and fossil fragments. Important secondary phases are lithic fragments, glauconite and opaque minerals.

On the other hand, Table 2.3 provides the results obtained through the dual range Fourier Transform Infrared (FT-IR) supplied by SDR. As in the previous analysis, the silt-rich

Kortemark and Roubaix members contain relatively more quartz and feldspar and less clay. On the contrary, the clay-rich Aalbeke member consists of almost 79% clay minerals. Nearly 62% of the Orchies Member is composed of clay minerals. The highest carbonate contents are measured in samples from the upper part of Orchies member and in samples from the Roubaix member.

Table 2.3 Mineralogy of the Ypresian clays determined by FT-IR in the Doel-1A well.

Stratigraphy	Depth (m)	Quarz (%)	Feldespar (%)	Carbonate (%)	Clay (%)	Other (%)
Kortemark	345.6	40.8	4.2	1.1	48.1	5.6
Aalbeke	353.0	2.6	3.7	0.7	79.6	13.3
Roubaix	358.9	20.4	2.6	1.1	69.7	6.3
Roubaix	379.9	45.7	8.7	4.6	38.9	2.2
Roubaix	399.8	31.2	5.3	2.3	53.8	7.4
Orchies	425.1	16.6	2.7	5.7	67.7	7.3
Orchies	435.2	22.8	5.9	0.7	65.4	5.3

From samples taken on Kallo area, KULeuven (report, 2011) also performed XRD to obtain the bulk mineralogy of the Ypresian clay in this zone, and results are presented in Table 2.4.

Table 2.4 Bulk mineralogy of the Ypresian clays from Kallo wells.

Sample	Depth (m)	Qtz (%)	Kspar (%)	Plag (%)	Cal (%)	Dol (%)	Pyr (%)	Anat (%)	O-CT (%)	Zeo (%)	ΣNC (%)	Kaol (%)	Chl (%)	Σ2:1 (%)	ΣC (%)	Total (%)
6-b	293.44-293.56	39	5	5	0	0	0.7	0.4	4	0	54	1	1	43	46	100
15-a	302.82-302.88	42	5	6	0.8	0	1	0.5	6	0	61	2	0	37	39	100
27-b	314.47-314.59	28	6	4	0	0.8	0.5	0	0	0	39	2	2	57	61	100
35-b	322.47-322.59	39	5	6	0.3	0.7	1	0.7	1	0	55	1	1	43	45	100
44-b	331.42-331.54	32	6	6	1	1	0.4	0	0	0	46	2	3	49	54	100
54-b	341.35-341.47	45	4	5	3	0.2	0.5	0.7	1	1	61	1	3	35	39	100
63-b	350.35-350.47	36	7	6	0.8	0.9	0.7	1	0	0	52	5	3	40	48	100
74-b	361.23-361.35	31	6	5	0	0.8	0.4	0	0	0	43	3	4	50	57	100
86-b	373.07-373.19	43	5	6	0	0.7	0.3	0.8	0	0	56	3	4	37	44	100
96-b	382.95-383.07	27	7	3	3	1	0.3	0.5	0	0	42	3	3	53	58	100
101-b	387.95-388.07	34	8	7	0	0	0.8	0.9	0	0	51	9	6	34	49	100
105-b	391.91-392.03	24	6	3	0	0	0.5	0.8	0	0	35	9	4	52	65	100
110-b	396.75-396.87	25	6	4	0	0	0.9	0.7	0	0	37	7	5	51	63	100
113-b	399.73-399.85	44	6	4	0	0	0.7	0.5	0	0	54	4	5	36	46	100
114-b	400.74-400.86	72	2	1	0	0	0.3	0	0	0	75	1	4	19	25	100

Where: Qtz=quartz; Kspar=K-feldspar; Plag=plagioclase; Cal=calcite; Dol=dolomite; Pyr=pyrite; Anat=anatase; O-CT=Opal CT; Zeo=zeolite; ΣNC=Total Non-Clays; Kaol=kaolinite; Chl=chlorite; Σ2:1=2:1 dioctahedral clays and micas= illite + smectite + illite-smectite + glauconite + micas; ΣC=Total Clays.

2.3.2.2. Cation exchange capacity

The cation exchange capacity (CEC) was determined by LTGH (Doel samples) and KULeuven (Kallo samples). LTGH used the NH_4OAc-method to get CEC measurements, whereas the KULeuven applied the Co-hexamine technique to distinguish between iilite (muscovite) and smectite, since they were quantified together in the group "2:1 dioctahedral clays & micas". Boundary values from both analyses are synthesised in Table 2.5.

Table 2.5 Cation exchange capacity of the Ypresian clays from Doel and Kallo wells.

Drilling	CEC (meq/100g)	
	Min	Max
Doel (LGTH)	17.5	35.6
Kallo (KULeuven)	13.1	34.8

2.3.2.3. Clay mineralogy

In relation to the clay mineralogy analysis, the LTGH carried out XRD, which only provided semi-quantitative data (Figs. 2.11 and 2.12).

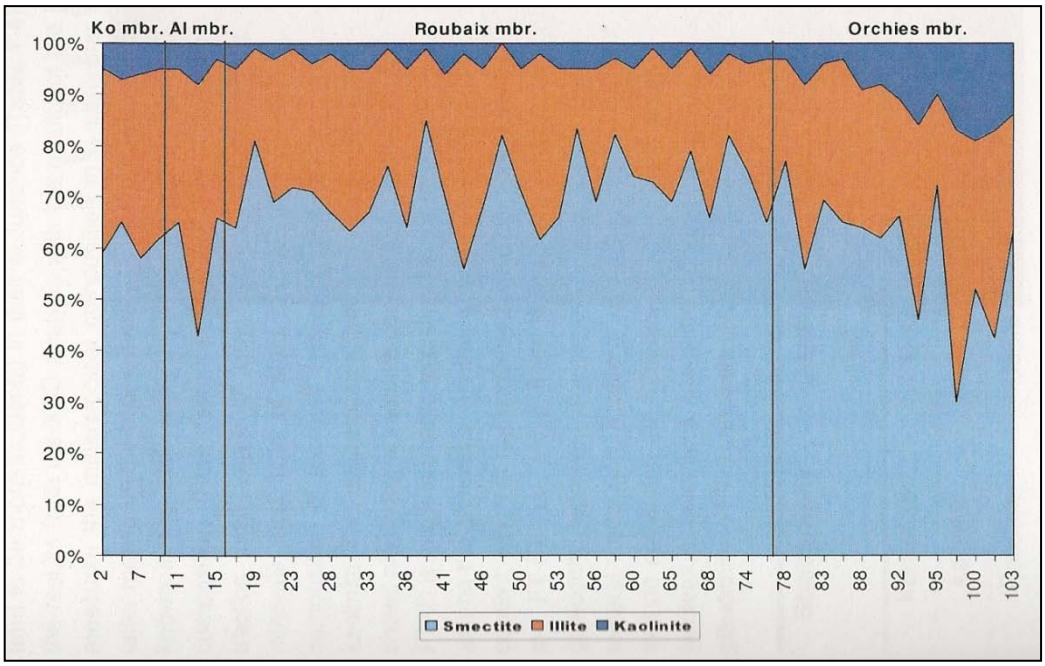

Figure 2.11 Clay mineralogy in the clay fraction of Ypresian clays from borehole Doel 1-A analysed by LTGH.

Clay fraction shows that the dominant mineral smectite, which is mixed with illite with a relative contribution of approximately 28%, kaolinite with a relative contribution of 6% (toward the Orchies member up to 11%), and chlorite that is only present in trace amounts.

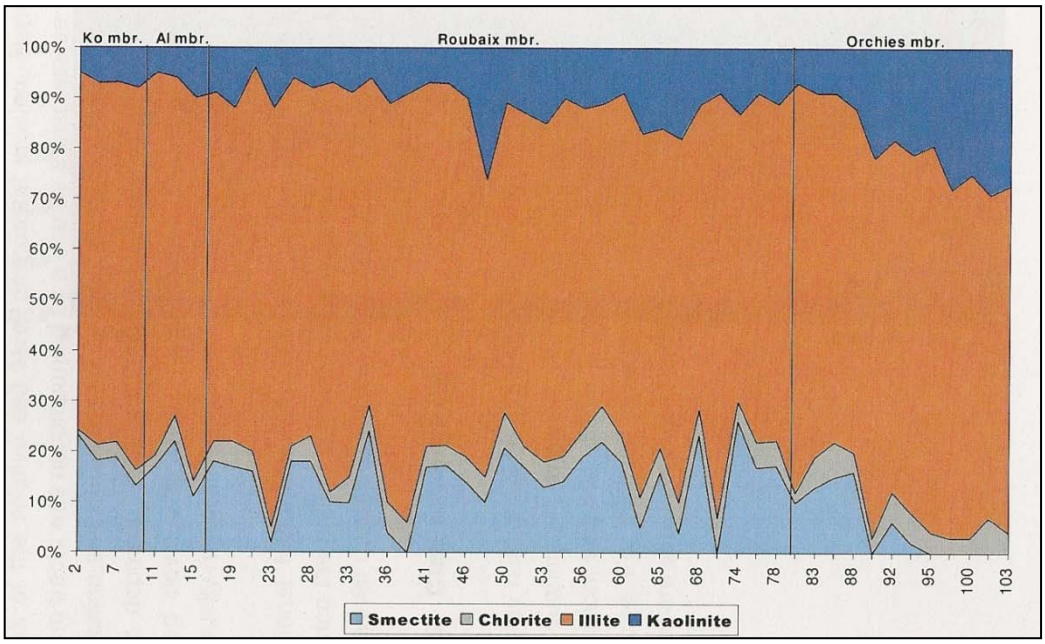

Figure 2.12 Clay mineralogy in the silt fraction of the Ypresian clays from borehole Doel 1-A analysed by LTGH.

Concerning the silt fraction, illite is the mineral in abundance, with a relative contribution of around 70%, mixed with kaolinite in the range of 12 ± 6%, and chlorite with a relative contribution of approximately 4.5 ± 1.5%.

From these last figures it is possible to extract two important conclusions. First, that in the zone of Doel-1A well there is a dominant presence of swelling clays, and second, that the difference between both grain size fractions confirms that illite, chlorite and kaolinite have a coarser grain size distribution than smectite and illite-smectite mixed layers.

Likewise, the results of FT-IR analysis conducted by SDR (Table 2.6) confirms that the predominant clay minerals in the Ypresian clay are illite and smectite in greater proportions followed by kaolinite and glauconite, which tend to be more incidental in their occurrence.

Table 2.6 Clay mineralogy of the Ypresian clays from Doel samples determined by FT-IR.

Stratigraphy	Depth (m)	Illite (%)	Smectite (%)	Kaolinite (%)	Glauconite (%)
Kortemark	345.6	40	49	0	11
Aalbeke	353.0	41	56	0	3
Roubaix	358.9	43	46	0	11
Roubaix	379.9	41	45	0	14
Roubaix	399.8	34	48	0	10
Orchies	425.1	47	45	0	8
Orchies	435.2	53	27	11	9

In the case of the analysis performed by KULeuven on Kallo samples (report, 2011), oriented sedimentation slides were made using XRD at different states (air-dry, ethylene glycol saturated, heated to 550°C/1h). Results from this analyses are summarised in

Table 2.7, which shows the mass% contributions for each clay phase relative to the extracted 2 µm fraction.

The samples were divided into two distinct groups based on their clay mineralogy:

- The shallowest samples (between depths of 293.44 and 383.07m) are dominated by smectite. Also a considerable amount of highly illitic randomly interstratified illite-smectite is present, together with minor amounts of illite, chlorite and kaolinite. The kaolinite is actually mixed-layered kaolinite-smectite with a small amount of expandable layers (max 20%).
- The deepest samples differ from the first group in that they have (sometimes significantly) lower smectite contents, and clearly higher amounts of illite and kaolinite. A similar highly illitic randomly interstratified illite-smectite, as in the first group, is present in similar quantities.

Table 2.7 Clay mineralogy of the Ypresian clays determined from Kallo wells (* slightly swelling).

Sample	Depth (m)	Randomly interstratified illite-smectite		Illite	Smectite	Kaolinite	Chlorite	*Total 2:1*
		wt%	*%S*	wt%	wt%	wt%	wt%	*wt%*
6-b	293.44-293.56	26	*38*	8	64	2*	0	*98*
15-a	302.82-302.88	25	*41*	8	65	2*	0	*98*
27-b	314.47-314.59	23	*41*	11	60	2*	4	*94*
35-b	322.47-322.59	23	*41*	9	63	2*	3	*95*
44-b	331.42-331.54	24	*38*	9	63	2*	2	*96*
54-b	341.35-341.47	24	*35*	8	64	2*	2	*96*
63-b	350.35-350.47	24	*33*	9	62	1*	4	*95*
74-b	361.23-361.35	22	*38*	10	63	2*	3	*95*
86-b	373.07-373.19	24	*37*	7	64	2*	3	*95*
96-b	382.95-383.07	23	*37*	10	59	3*	5	*92*
101-b	387.95-388.07	28	*35*	19	34	15	4	*81*
105-b	391.91-392.03	21	*37*	25	37	12	5	*83*
110-b	396.75-396.87	19	*37*	23	43	11	4	*85*
113-b	399.73-399.85	25	*33*	13	52	8	2	*90*
114-b	400.74-400.86	31	*33*	11	50	8	0	*92*

Where: %*S*= swelling of the mixed-layered phases expressed as %.

Finally, as mentioned before, data related to the clay mineralogy of the Ypresian clay of others zones throughout the Belgian basin is scarce and purely qualitative. Van Marcke and Laenen (2005) gathered the analysis of three different areas previously published in Mercier-Castiaux and Dupuis (1988 and 1990). The results of the above analysis are summarised in Figure 2.13.

In the Knokke well, the Ypresian clay sequence can be subdivided into three mineralogical zones:

- Between 288 m and 180 m, the clay mineralogy is similar to the one observed in the underlying Paleocene beds. The average contents are 12% chlorite, 24% illite, 10% kaolinite, 52% smectite and trace amounts illite-smectite and chlorite-smectite mixed

layers. This zone encompasses the Kortrijk formation and the lower part of the Kortemark silt.

- Between 146 m and 180 m the contents in illite, chlorite and kaolinite decrease to the benefit of smectites. The average contents are 4% chlorite, 19% illite, 3% kaolinite and 74% smectite. This zone corresponds to the silty part of the Kortemark member and to the overlying Egemkapelle clay member.

- Between 130 m and 146 m chlorite and kaolinite disappear and the content in smectite is very high. The average content of chlorite reaches 11% and the one of smectite almost 88%. This zone corresponds to the Egem sand member and the Vlierzele formation.

At other locations within the Belgian Basin, a similar zoning is observed, although it becomes less pronounced towards the East (Fig. 2.13). When comparing the Knokke, Kallo and Mol sections, a decrease of chlorite, illite and kaolinite towards the East is noticed.

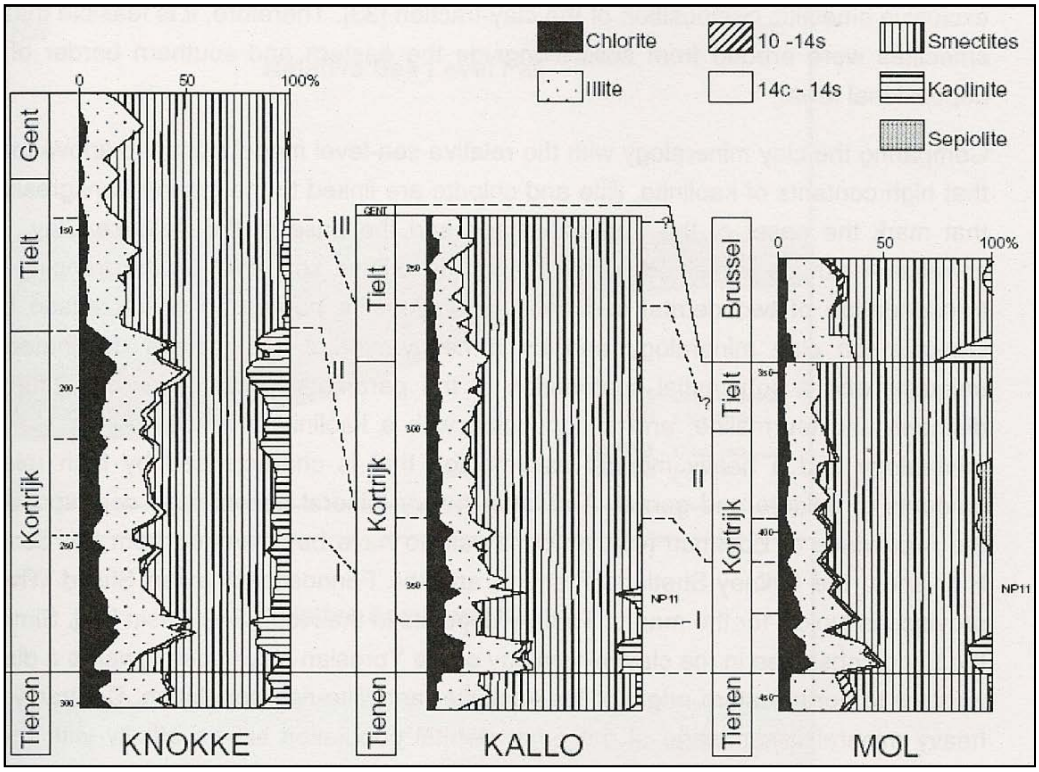

Figure 2.13 Clay mineralogy of the Ypresian Clay along an East-West section through the Belgian Basin.

2.3.3 Basic geotechnical characterisation

To get an overall picture of the basic geotechnical characterisation of Ypresian clay, Table 2.8 summarises the results of the analysis of samples taken from Doel-1A and performed by INISMa and LGC.

Table 2.8 Comparison of the basic geotechnical characterisation of Ypresian clay from Doel samples presented by INISMa and LGC.

Stratigraphy	Depth (m)		Bulk density (Mg/m3)		Density of soil solids (Mg/m3)			Porosity (%)		Water content (%)	
	INISMa	LGC	INISMa	LGC	INISMa	LGC water	LGC toluene	INISMa	LGC	INISMa	LGC
Aalbeke	349.9	351.4	1.901	1.850	2.725	2.791	2.742	48.1	50.7	34.4	34.5
Roubaix	361.8	363.3	1.935	1.913	2.689	2.750	2.694	44.1	46.9	28.7	30.9
Roubaix	369.8	371.3	1.978	1.973	2.703	2.745	2.710	43.1	43.8	28.6	27.9
Roubaix	376.8	378.3	1.996	1.955	2.692	2.756	2.694	42.0	44.5	27.9	27.9
Roubaix	386.8	388.3	1.997	1.955	2.695	2.744	2.702	41.5	44.0	26.9	27.2
Roubaix	396.7	398.2	2.013	1.986	2.715	2.756	2.702	41.5	43.2	26.7	26.8
Roubaix	404.7	406.1	2.031	2.000	2.741	2.768	2.725	41.3	41.6	26.3	23.8
Orchies	419.4	420.9	1.985	1.993	2.714	2.769	2.724	42.1	42.6	26.4	25.5
Orchies	431.3	432.8	2.035	2.009	2.708	2.748	2.707	37.2	36.3	19.6	19.9
Orchies	440.3	439.8	2.067	2.119	2.682	2.765	2.725	33.5	36.0	15.9	19.8

Results provided by both analysis, matched quite well. There is also information available on the granulometric composition and the Atterberg limits obtained by LGC (Table 2.9) and the specific surface (Table 2.10) and the porosimetry (Figure 2.14) determined by INISMa through BET method and mercury intrusion porosimetry (MIP) tests, respectively (INISMa, 1998, report 74.252).

Table 2.9 Granulometric composition and Atterberg limits of Ypresian clay from Doel samples obtained by LGC.

Stratigraphy	Depth (m)	Granulometry (%)			Atterberg limits (%)		
		>60 µm	2-60 µm	<2 µm	W_L	W_P	I_P
Aalbeke	351.37	3.3	40.7	56.0	189.9	39.6	150.2
Roubaix	363.33	0.7	59.5	39.8	129.5	34.5	95.0
Roubaix	371.29	0.3	73.5	26.2	96.3	29.8	66.5
Roubaix	378.28	0.8	67.4	31.8	120.7	33.9	86.8
Roubaix	388.27	0.7	76.5	22.8	101.4	31.2	70.2
Roubaix	398.19	0.7	71.0	28.3	134.8	30.2	104.6
Roubaix	406.14	1.8	66.0	32.2	139.5	31.2	108.3
Orchies	420.89	0.4	72.6	27.0	136.1	30.0	106.1
Orchies	432.79	1.0	43.0	56.0	93.8	24.1	69.7
Orchies	439.81	0.5	43.5	56.0	91.5	27.9	63.6

At this point it would be worthwhile to remark that the results of granulometric composition and the Atterberg limits are consistent with the conclusions indicated in section 2.3.1. The Aalbeke member and the lower part of Orchies member are mainly clayey materials, while the samples of the Roubaix member and the upper part of the Orchies member are richer in silt. The sand fraction is in all samples very low.

Table 2.10 Specific surfaces of Ypresian clay from Doel samples obtained by INISMa.

Depth (m)	Specific surface (m^2/g)
340.87	50
345.87	50
349.87	41
353.87	58
357.83	57
361.83	47
366.81	50
369.79	58
373.73	42
376.78	85
381.78	52
386.77	34
389.74	48
392.74	27
396.71	38
400.69	35
404.68	24
408.64	43
414.48	23
419.42	40
423.39	45
427.35	42
431.29	42
436.29	40
440.31	77

MIP results are presented only for two representative samples of the entire set of tests performed by INISMa.

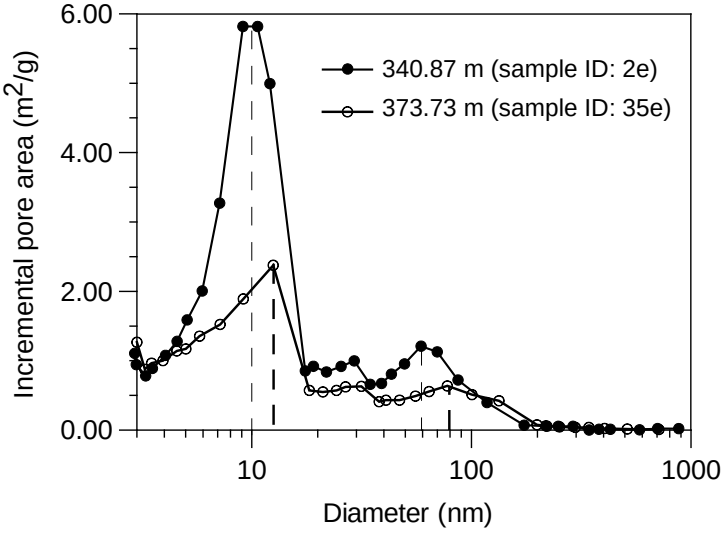

Figure 2.14 Incremental pore area of Ypresian clay from Doel samples obtained by INISMa.

2.4 HYDRAULIC PROPERTIES

In this section, the results of water permeability from samples taken in Doel-1A well (SCK. CEN) and pressure pulse tests performed in Doel-1B borehole (ONDRAF/NIRAS), are summarised.

By pulse injection experiments with the water flow direction being perpendicular to the bedding planes, the SCK.CEN estimated the water permeability results for tritiated water (HTO) and Iodide (I^-), which are summarised in Table 2.11.

Table 2.11 Results of pulse injection tests performed by SCK-CEN on Doel-1A samples (SCK-CEN, 2005, report 3589).

Stratigraphy	Depth (m)	Water permeability (m/s)
Kortemark	340	6.4E-12
Kortemark	346	8.0E-12
Aalbeke	350	1.4E-12
Aalbeke	353	8.2E-13
Roubaix	358	1.6E-12
Roubaix	362	1.9E-12
Roubaix	367	2.0E-12
Roubaix	370	4.6E-12
Roubaix	374	3.4E-12
Roubaix	377	1.6E-12
Roubaix	382	1.5E-11
Roubaix	387	1.3E-11
Roubaix	390	5.7E-11
Roubaix	391	5.6E-12
Roubaix	397	1.3E-12
Roubaix	401	6.4E-12
Roubaix	405	1.2E-12
Roubaix	409	1.6E-12
Roubaix	415	3.4E-12
Roubaix	420	2.5E-12
Orchies	424	1.2E-12
Orchies	428	8.7E-13
Orchies	432	1.1E-12
Orchies	437	8.4E-13
Orchies	442	3.2E-12

In addition, pressure pulse tests (PPTs) were performed in the open-hole section of the Doel-1B boreholes to provide an approximation of the in-situ permeability. Results are shown in Table 2.12.

Table 2.12 Results of pressure pulse tests performed in Doel-1B boreholes.

Stratigraphy	Water permeability (10^{-12} m/s)
Kortemark	170; 110
Aalbeke	100
Roubaix	130; 100
Orchies	90; 100

It is noteworthy to remark that the results of pressure pulse tests are higher than laboratory tests, an effect that can be associated with the different scales involved, to the measurement method itself and to the fact that laboratory tests measure the vertical water permeability, whereas the pressure pulse tests measure the horizontal one.

2.5 GEOMECHANICAL PROPERTIES

In Tables 2.13, 2.14 and 2.15 the results of the geomechanical properties of Ypresian clay derived from uniaxial compression, triaxial and swelling tests carried out by LGC on different samples taken from Doel-1A, are presented.

The uniaxial compression tests on specimens prepared from drill cores, allowed determining the uniaxial compressive strength σ_c and the elastic constants, Young's modulus E and Poisson's ratio v.

Table 2.13 Results of the uniaxial compression tests performed by LGC.

Stratigraphy	Depth (m)	σ_{max} (MPa)	ε at σ_{max} (-)	E (MPa)	v (-)
Aalbeke	351.37	0.485	2.40	40.72	0.10
Roubaix	363.33	0.744	2.57	28.43	0.14
Roubaix	371.29	0.591	2.63	39.15	0.41
Roubaix	378.28	0.761	3.45	32.93	0.28
Roubaix	388.27	0.791	4.60	27.95	0.30
Roubaix	398.19	0.509	4.50	24.56	0.21
Roubaix	406.14	0.780	3.56	18.32	0.22
Orchies	420.89	0.827	2.51	37.97	0.24
Orchies	432.79	1.942	1.97	86.99	0.28
Orchies	439.81	1.255	3.18	86.22	0.31

The Young's moduli given in the above table are secant Young's moduli taken at 33% of the peak strength.

To obtain cohesion and friction angles, the LGC performed undrained triaxial compression tests on several specimens of core samples previously consolidated. The highest values for the cohesion and the friction angle were obtained in the Roubaix member.

Table 2.14 Results of undrained triaxial compression tests conducted by LGC.

Stratigraphy	Depth (m)	Cohesion (MPa)	ϕ (deg)
Aalbeke	350.87	0.23	8.1
Roubaix	362.83	0.22	12.3
Roubaix	370.79	0.47	11
Roubaix	377.78	0.32	12.4
Roubaix	387.77	0.42	12.1
Roubaix	397.69	0.33	11.1
Roubaix	405.64	0.56	9.1
Orchies	420.39	0.34	10.2
Orchies	432.29	0.31	9.8
Orchies	439.31	0.35	9.5

Finally, the swelling properties of the Ypresian clay were determined allowing vertical swelling and measuring the swelling strain ε_s. Then, the samples were loaded up to their initial void ratios, thus determining the swelling pressures σ_s. The values of swelling strain and swelling pressures, presented in Table 2.15 are consistent with the clay and silt content, as well as with the amount of smectite presented in the previous sections.

Table 2.15 Swelling properties of the Ypresian clay determined by LGC.

Stratigraphy	Depth (m)	σ_S (MPa)	ε_s (-)
Aalbeke	350.87	1.72	31.2
Roubaix	362.83	1.17	14.3
Roubaix	370.79	0.08	1.3
Roubaix	377.78	0.31	2.3
Roubaix	387.77	0.27	1.7
Roubaix	397.69	0.95	14.8
Roubaix	405.64	1.82	11.4
Orchies	420.39	1.28	17.3
Orchies	432.29	1.37	19.2
Orchies	439.31	1.44	17.8

The geomechanical characterisation programme was performed on samples with horizontal bedding planes.

2.6 THERMAL PROPERTIES

INISMa analysed the thermal behaviour of the Ypresian clay, by determining the heat capacity and the thermal conductivity in some selected samples taken from Doel-1A well.

The specific heat was determined on dry samples at different temperatures. Taking into account the water content of a saturated sample and a specific heat for water of 4186J/kg (considered as a constant value in the range of temperature), it is possible to calculate the

specific heat and the heat capacity per unit volume for wet samples. The results are shown in Table 2.16.

Table 2.16 Thermal properties of the Ypresian clay determined by INISMa.

Parameter	Min	Max	Mean	Standard deviation
Specific heat dry (J/(kg. K))	927	1017	974	22
Specific heat saturated (J/(kg. K))	1452	1796	1660	18.80
Thermal capacity dry (MJ/(m^3. K))	1.38	1.81	1.52	0.10
Thermal capacity saturated (MJ/(m^3. K))	3.00	3.42	3.28	0.10
Thermal conductivity (W/(m. K))	0.62	1.12	0.80	0.13

CHAPTER 3

MATERIAL USED IN THE INVESTIGATION

3.1 INTRODUCTION

In the previous chapter, the overall Ypresian clay formation context related to its thermo-hydro-mechanical THM behaviour gained from latest investigations was presented. This chapter places the attention on the general characterisation of the material received at the UPC Geotechnical Laboratory and used in this research. The tested intact material corresponds to two cores samples obtained from Kallo borehole at depths around 340 and 370 m.

As a first step of the comprehensive geotechnical characterisation program of the material described in next chapters, the present one introduces the material by describing its mineralogical composition obtained from X-ray diffraction analysis and the presentation of some index properties determined by basic geotechnical characterisation tests. Additionally, an initial total suction value using a chilled-mirror dew-point psychrometer was determined.

Finally, tables with results from previous analyses carried out on samples taken in areas close to those analysed in this research are presented and compared.

3.2 ORIGIN OF THE MATERIAL AND MINERALOGY

3.2.1 Origin of the material

The soil used in the investigation comes from the Kallo drilling campaign performed by ONDRAF/NIRAS to provide continuity to the study performed in the Doel nuclear zone and to get a better understanding of the Ypresian clay THM response. From this campaign, two undisturbed core samples arrived at the UPC Geotechnical Laboratory in their respective casing tubes, both inside a sealed box, in December 2009 (Fig. 3.1).

Figure 3.1 Packing of the Kallo samples delivered to UPC Laboratory.

Samples were extracted from Kallo-1 well with coordinates X: 144287.22 and Y: 219656.6 East/North, respectively. Kallo town is part of the municipality of Beveren, which is located in the Belgian province of East Flanders. According to the geographical distribution presented in the previous chapter (Fig. 2.3), the Kallo region is part of the denominated "area of interest" and belongs to area II. In Table 3.1 the identification of samples used in this research, is summarised.

Table 3.1 Identification of samples used in the investigation.

Drilling	Core Identification	Formation	Member	Core depth (m)		L	Φ
				Top	Bottom	(m)	(m)
Kallo-1	53	Kortrijk	Roubaix	339.72	340.72	0.80	0.10
Kallo-1	83	Kortrijk	Roubaix	369.76	370.56	0.80	0.10

According to the original core description, in the depth interval between 336.76 – 341.72 m, pale calcareous silty clay, was identified. Unfortunately for the 369.56 – 370.56 m interval, this information is not available (Vandenberghe and Mohammad (2009) referred in KULeuven report (2011)).

Additional to the core description, geophysical logs were run by GEO-data (2008). In the depth interval of particular interest (between 339 - 371 m, approximately), samples were described as: *"clay, mostly hard, compact greasy, greenish grey. Slightly silty"* and the lithostratigraphy available information placed them within the Moen member (formally named the Roubaix member), which is part of the Kortrijk formation.

In general terms, as described in chapter 2, the Kortrijk formation is a predominantly clayey deposit that was formed in a marine environment. The succession of the different members and their composition varies from place to place. In Van Marcke and Laenen (2005), a lithostratigraphic interpretation of the Kallo well (BGD 27E/148), is presented.

The in situ pore water chemistry of the Ypresian clay of Kallo-1 well, is composed mainly by NaCl with low concentration of SO_4^{-2}, the average concentration of the sodium cation [Na^+] is 0.13 mol/L (SCK-CEN (2009), Personal communication).

3.2.2 X-ray diffraction analysis

To get a qualitative characterisation of the mineralogical composition of the studied material, an X-ray diffraction analysis was performed on air-dried randomly oriented powdered sample passing through sieve No. 200.

The main characteristics of the equipment used are listed below:

- Model: *X'Pert PRO MPD Alpha1* powder diffractometer (*PANalytical*).
- Incident radiation wavelength, λ: 1.5406 Å (Cu $K_{\alpha 1}$ radiation).
- Focalizing Ge (111) primary monochromator.
- *X'Celerator* Detector: Active length = 2.122 º.
- $\theta/2\theta$ scan from 4 to 80º 2θ with step size of 0.017º and measuring time of 50 seconds per step.

The identification of crystals using X-ray diffraction (XRD) is based on Bragg's law. Since two minerals do not have the same spacing of interatomic planes (d) in three dimensions, the angle at which diffraction occurs (θ) can be used for identification (Mitchell and Soga, 2005). In Figure 3.2, the results of XRD showing the intensity of diffracted beam (expressed in counts) as a function of angle 2θ are presented.

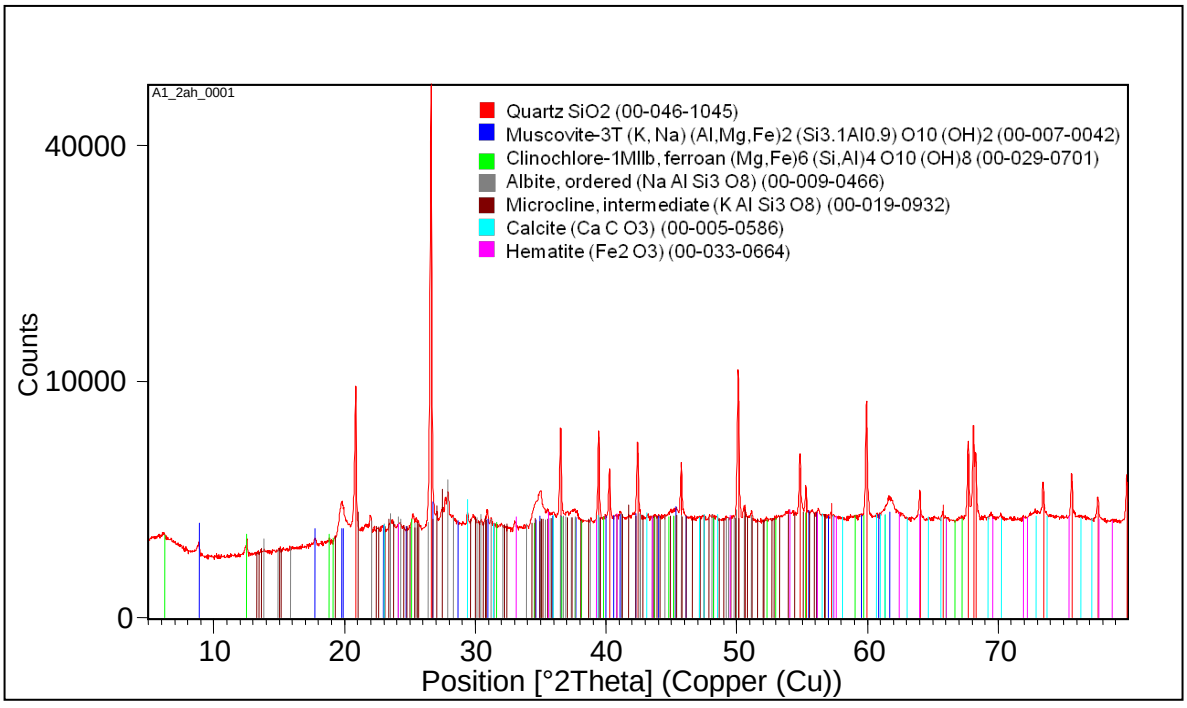

Figure 3.2 X-ray diffraction of the studied material.

Through the comparison between test pattern and the different patterns of known materials, it was possible to identify the presence of certain minerals according to three intensity levels, as follow:

- High intensity: quartz.
- Medium intensity: illite/ muscovite, chlorite, feldspar type plagioclase (albite), potassium feldspar, calcite, possible presence of hematite (not clear).
- Low intensity: possible presence of smectite (or similar) poorly crystallized.

According to Mitchell and Soga (2005), the powder method works because the very large number of particles in a sample ensures that some will always be properly oriented to produce a reflection. Nevertheless, an X-ray diffraction following oriented aggregates of particles method would be more appropriated to detect the clayey fraction.

3.3 GEOTECHNICAL CLASSIFICATION TESTS

According to ASTM standard procedures (Book of Standards Volume: 04.08-04.09), gravimetric water content (w), density of soil solids (ρ_s) and consistency limits (w_L and w_P) were determined in samples taken from core identification number 83. Based on core dimensions it was possible to estimate bulk density (ρ), dry density (ρ_d), void ratio (e), porosity (n) and degree of saturation (Sr).

Initial total suction was measured with a chilled-mirror dew-point psychrometer (Cardoso et al. (2007)).

Table 3.2 Basic geotechnical characterisation of samples used in the investigation.

Soil properties	Ypresian clay, Kallo samples Depth: 369.76-370.56 m
Density, ρ	1.97 to 2.02 Mg/m^3
Dry density, ρ_d	1.55 to 1.60 Mg/m^3
Gravimetric water content, w	26.0 to 26.6%
Initial total suction, Ψ	2 MPa
Density of soil solids, ρ_s	2.76 Mg/m^3
Void ratio, e	0.72 to 0.78
Porosity, n	0.418 to 0.438
Degree of saturation, Sr	94 to 98 %
Liquid limit, w_L	142 to 158 %
Plasticity index, PI	116 to 133%

3.4 GEOTECHNICAL PROPERTIES BASED ON PREVIOUS REPORTS

From previous analyses on Kallo samples performed by KULeuven (report, 2011), it is possible to get information on the grain size and the mineralogical composition of samples from depths equivalent to those tested in this research. The results are presented in Table 3.3.

Table 3.3 Grain size and mineralogical composition of Kallo samples (summary from previous reports).

Analysis type	Parameter	Unit	Kallo samples KULeuven (report, 2011) Interval depth (m)				
			331.42-331.54	341.35-341.47	350.35-350.47	361.23-361.35	373.07-373.19
Grain size	Sand 63µm-2mm	(%)	0.28	0.05	0.23	0.06	1.72
	Silt 2-63µm	(%)	44.25	43.79	43.3	38.69	43.56
	Clay <2µm	(%)	55.48	56.16	56.46	61.26	54.72
Bulk mineralogy	Quartz	(%)	32	45	36	31	43
	K-feldspar	(%)	6	4	7	6	5
	Plagioclase	(%)	6	5	6	5	6
	Calcite	(%)	1	3	0.8	0	0
	Dolomite	(%)	1	0.2	0.9	0.8	0.7
	Pyrite	(%)	0.4	0.5	0.7	0.4	0.3
	Anatase	(%)	0	0.7	1	0	0.8
	Opal CT	(%)	0	1	0	0	0
	Zeolite	(%)	0	1	0	0	0
	Total Non-Clays	(%)	46	61	52	43	56
	Kaolinite	(%)	2	1	5	3	3
	Chlorite	(%)	3	3	3	4	4
	2:1 Dioctahedral clays and micas	(%)	49	35	40	50	37
	Total Clays	(%)	54	39	48	57	44
	Total	(%)	100	100	100	100	100
Clay mineralogy	Randomly interstratified illite-smectite	wt%	24	24	24	22	24
	Illite	wt%	9	8	9	10	7
	Smectite	wt%	63	64	62	63	64
	Kaolinite	wt%	2*	2*	1*	2*	2*
	Chlorite	wt%	2	2	4	3	3

Figure 3.4 shows the situation map of Doel and Kallo towns in Belgium, which are relatively close (approximately 13 km by road).

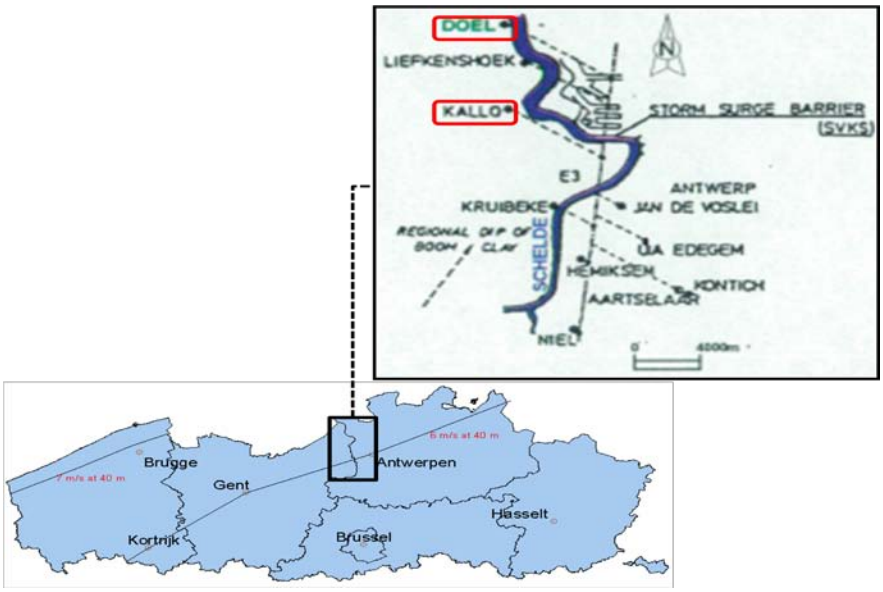

Figure 3.4 Situation map of Doel and Kallo towns in Belgium.

Taking into consideration the proximity between both towns, the lack of available geotechnical information in Kallo area and to allow for further comparisons, Table 3.4 synthesises the results obtained from Doel samples and presented in detail in chapter 2.

Table 3.4 Basic geotechnical properties of Doel samples (summary from previous reports).

Soil properties	Doel samples Van Marcke and Laenen (2005) Interval depth (m)	
	340.87-351.87	369.79-371.79
Density, ρ	1.85 to 1.90 Mg/m^3	1.87 to 1.98 Mg/m^3
Dry density, ρ_d	1.41 to 1.45 Mg/m^3	1.54 Mg/m^3
Gravimetric water content, w	30.5 to 34.9 %	27.9 to 29.3 %
Density of soil solids, ρ_s	2.63 to 2.79 Mg/m^3	2.70 to 2.75 Mg/m^3
Void ratio, e	0.81 to 1.03	0.76-0.86
Porosity, n	0.449 to 0.507	0.431 to 0.463
Degree of saturation, Sr	88.3 to 98.8 %	93.3 to 100 %
Liquid limit, w_L	189.9 %	96.3 %
Plasticity index, PI	150.2 %	66.5 %
Vertical water permeability (T=20ºC), k_{wv}	(1.4 to 8.0) x 10^{-12} m/s	4.6 x 10^{-12} m/s
Horizontal water permeability (T=20ºC), k_{wh}	(110 to 170) x 10^{-12} m/s	(100 to 130) x 10^{-12} m/s
Young's modulus, E	40.72 MPa	39.15 MPa
Poisson's coefficient, ν	0.10	0.41
Friction angle, ϕ (undrained)	8.1º	11º

CHAPTER 4

EXPERIMENTAL TECHNIQUES AND PROTOCOLS

4.1 INTRODUCTION

This chapter describes the experimental program carried out to characterise the thermo-hydro-mechanical THM behaviour of the material under study. A series of non-isothermal tests under controlled hydro-mechanical conditions and hydro-mechanical tests under temperature controlled conditions were performed. A brief description of the equipment used and protocols followed to achieve the proposed objectives is included.

The experimental program performed can be classified as follows:

- General hydraulic and mechanical characterisation:
  - Water retention curve determination using psychrometer measurements.
  - Estimation of the low-strain shear modulus using resonant column and bender elements tests.
  - Determination of the Young Modulus with ultrasonic pulse test.
- Hydro-mechanical characterisation under oedometer conditions:
  - Step-loading and unloading tests under saturated conditions (room temperature).
  - Stress-controlled continuous loading and unloading tests under saturated conditions at different temperatures (22 and 80ºC).
- Thermo-hydraulic characterisation:
  - Controlled-gradient water permeability tests at different temperatures (22, 40, 60 and 80ºC) using a constant volume (isochoric) cell immersed in a thermally controlled bath.
  - Controlled-gradient water permeability tests following different temperature paths and under constant effective vertical stress in odometer cell.
  - Heating pulse test.

In addition, mercury intrusion porosimetry MIP tests in some selected postmortem samples were performed to analyse the microstructural changes undergone after the macroscopic THM tests.

Tests were carried out using synthetic Ypresian clay water (SYCW) to match in-situ geochemistry conditions. This water was prepared based on the in situ pore water chemistry composition described in the previous chapter. Therefore, for 1 L of solution, 6.896 g of NaCl and 0.838 g of Na_2SO_4 were dissolved in degassed (oxygen free) water.

To take into account the anisotropic behaviour of the material, tests were systematically performed in vertical and horizontal sample orientations. A scheme of sample preparation and the orientation of the bedding planes is shown in Figure 4.1.

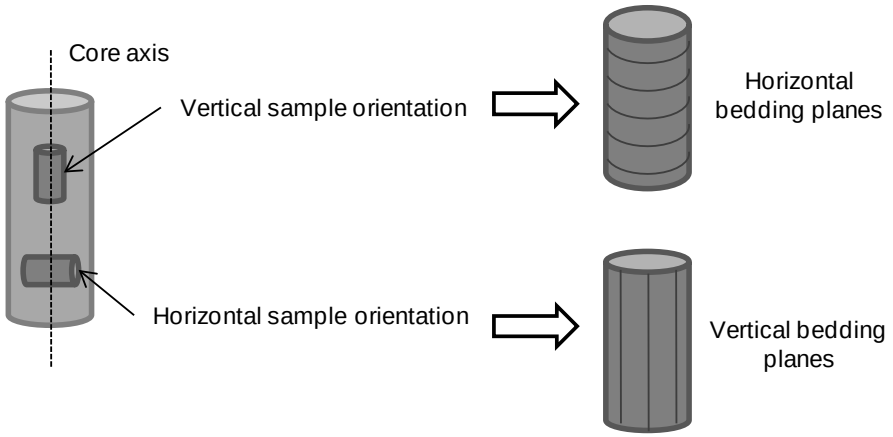

Figure 4.1 Scheme of sample coring and preparation.

4.2 MERCURY INTRUSION POROSIMETRY TEST

4.2.1 Brief description of the equipment

The mercury intrusion porosimetry MIP test provides information on the interconnected pore volume and its pore size distribution PSD.

The porosimeter used in the investigation was an 'AutoPore IV 9500' from *Micromeritics Instruments*. This equipment presents two pressure-generating systems: the low-pressure system works under dry nitrogen pressure in a range between 0.0025 and 0.2 MPa, whereas the high-pressure one uses oil for pressures in the range of 0.2 to 220 MPa (Fig. 4.2).

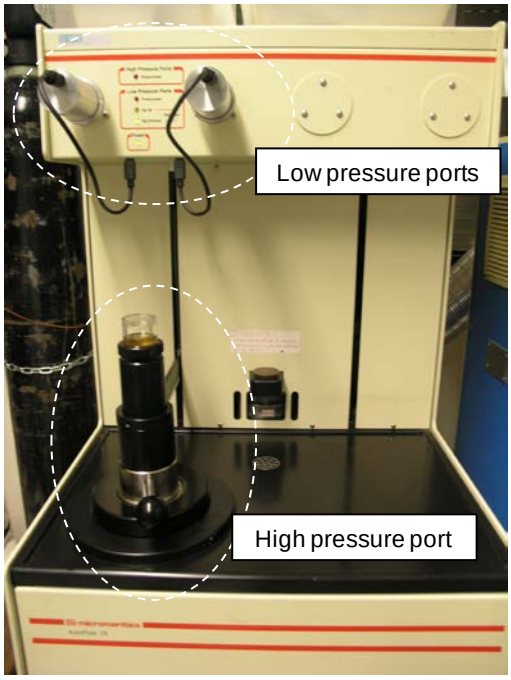

Figure 4.2 Mercury intrusion porosimetry equipment.

At different steps along the test, the injected mercury volume (per unit dry mass) and the total pressure applied are registered. The first gives information on the intruded void ratio of the sample and the second on the entrance pore size. For pores of cylindrical shape and parallel infinite plates, Washburn equation (Eq. 4.1) applies:

$$p = -\frac{n\,\sigma_{Hg}\,\cos\theta_{nw}}{x} \tag{4.1}$$

where p is the mercury total pressure applied, σ_{Hg} the surface tension of mercury, θ_{nw} the contact angle between mercury and the pore wall, and x the entrance or throat pore diameter (n = 4) or the entrance width between parallel plates (n = 2).

The background of MIP and limitations of the test are described in Romero and Simms (2008).

4.2.2 Test protocol

The size of the samples is conditioned by the size of the sample holder or penetrometer: cubical shape with an approximated size of 10 mm. Before testing in MIP equipment, samples are required to be dried. Freeze drying process seems to be appropriate, since surface tension effects induced by receding air-water interfaces are eliminated (Romero and Simms, 2008).

Following ASTM D4404-10 testing procedure, once the sample was trimmed and dried, it was weighed and installed in the low pressure port for a first vacuum application (the sample holder is filled with mercury). Then, mercury pressure was raised from 0.0025 to 0.2 MPa by filling first the larger pores. After this stage, the sample holder mass was measured (including the sample and the injected mercury mass) and placed inside the high pressure port to fill the smaller pores up to a maximum pressure of 220 MPa (entrance pore sizes around 7 nm). After completing this last filling stage, the extrusion path started to release mercury pressure. Some mercury was permanently entrapped in the constricted porosity after pressure release (Romero and Simms, 2008).

4.3 WATER RETENTION CURVE FROM PSYCHROMETER MEASUREMENTS

4.3.1 Brief description of the equipment

The chilled-mirror dew-point psychrometer measures the water potential through vapour transfer (total suction). The psychrometer used was a 'WP4-T Dewpoint PotentiaMeter' from *Decagon Devices Inc* (Fig. 4.3), which determines total suction from 1 to 300 MPa, with an accuracy of ±0.1 MPa from 1 to 10 MPa and ±1% from 10 to 300 MPa.

A soil sample in equilibrium with the surrounding air is placed in a sealed chamber, which contains a mirror with a photoelectric cell and a thermocouple attached to it. The first detects the exact point at which condensation first appears and the second one records the temperature at which it occurs. The condensation is induced with a thermoelectric (Peltier) cooler, which precisely controls the mirror temperature. Finally, the relative humidity is computed from the difference between the dew-point temperature of the air and the temperature of the soil sample (measured with an infrared thermometer). An internal fan is included to minimise the equalisation time.

The estimation of the soil total suction is based on the psychrometric law (Fredlund and Rahardjo, 1993):

$$\Psi = -\frac{RT\rho_w}{M_w}\ln(RH) \tag{4.2}$$

where ψ is the soil total suction, R the gas constant (8.314 J/(mol.K)), T the absolute temperature, M_w the molecular mass of water (18.016 kg/kmol), ρ_w the density of pure water (998 kg/m^3 at 293 K), and $RH=p_v/p_{v0}$ the relative humidity value of the vapour pressure, p_v, relative to the saturation vapour pressure, p_{v0}, at the same temperature.

More details, limitations and calibration of the equipment are described in Cardoso et al. (2007) and *Decagon Devices, Inc*. (2003).

4.3.2 Test protocol

A sample of approximately 12 cm^3 was analysed starting from its natural condition. It was then subjected to a multi-step air-drying process in a controlled environment with constant relative humidity of 47%, to obtain the drying branch of the curve. Once the maximum total suction was reached, the multi-step wetting process started by applying every day a drop of SYCW to the soil specimen. During drying and wetting processes a period of sample equalisation of 24 hours (sample hermetically closed) between each determination was allowed. As recommended by the manufactured, every day before using the equipment, the zero offset was adjusted with low concentration NaCl solution. The suction values were obtained directly from the display of the WP4-T equipment and adjusted according to correction proposed by Cardoso et al (2007).

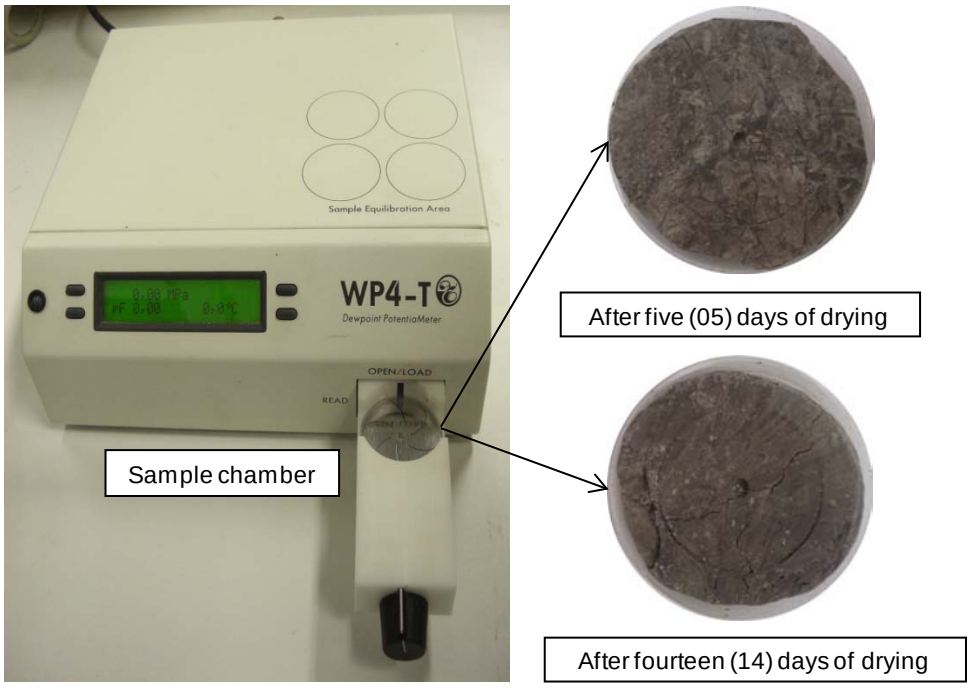

Figure 4.3 WP4-T equipment and sample.

4.4 RESONANT COLUMN TEST

4.4.1 Brief description of the equipment

The resonant column test gives information on the shear elastic modulus and damping properties of soils at small strains.

The working principle of the equipment used in this research is based on the transmission shear waves velocity through the soil, presented by Stokoe. Basically, a cylindrical specimen is fixed at one end and subjected to a cyclic shear solicitation at the opposite end. The torque is applied by friction to the upper surface of the specimen and is generated by an alternating current coil system, which induces cyclic oscillations with controlled amplitude and frequency. The cyclic shear solicitation generates shear strains, which is indirectly measured through an accelerometer fixed to the driving plate. The resonant frequency is obtained by varying the frequency of oscillation until the soil response (in terms of shear strain) is in phase with the excitation. The composition on the plane in terms of torque and shear strain gives an ellipse when they reach the resonance condition, which is observed on the oscilloscope screen (Fig. 4.4).

From the resonant frequency (f_n), the low-strain shear modulus (G) can be determined based on the following equation (Das, 1983):

$$G = \frac{4\,\pi^2\,L^2\,\rho\,{f_n}^2}{\alpha^2} \tag{4.3}$$

where L is the soil specimen length, ρ the density of the soil sample, and α is a dimensionless frequency factor. This last is a function of mass polar moments of inertia of soil (I) and of the driving system (I_0), both with respect to its own axis (Eq. 4.4)

$$\frac{I}{I_0} = \alpha \tan\alpha \;;\; I = \frac{\gamma\,\pi\,L\,D^4}{32\,g} \tag{4.4}$$

where γ is the unit weight, D the sample diameter and g is the acceleration of gravity.

The shear strain (γ) is not constant and an average shear strain ($\bar{\gamma}$) of 2R/3 is commonly used, being R the sample radius. According to Suriol (1993) the average shear strain can be determined from the equation 4.5.

$$\bar{\gamma} = k\,\frac{V_a}{{f_r}^2}\,\frac{2R}{L} \tag{4.5}$$

where V_a is the acceleration level of the driving plate and k a calibration factor.

Further specifications, limitations and advantages are described in Suriol (1993).

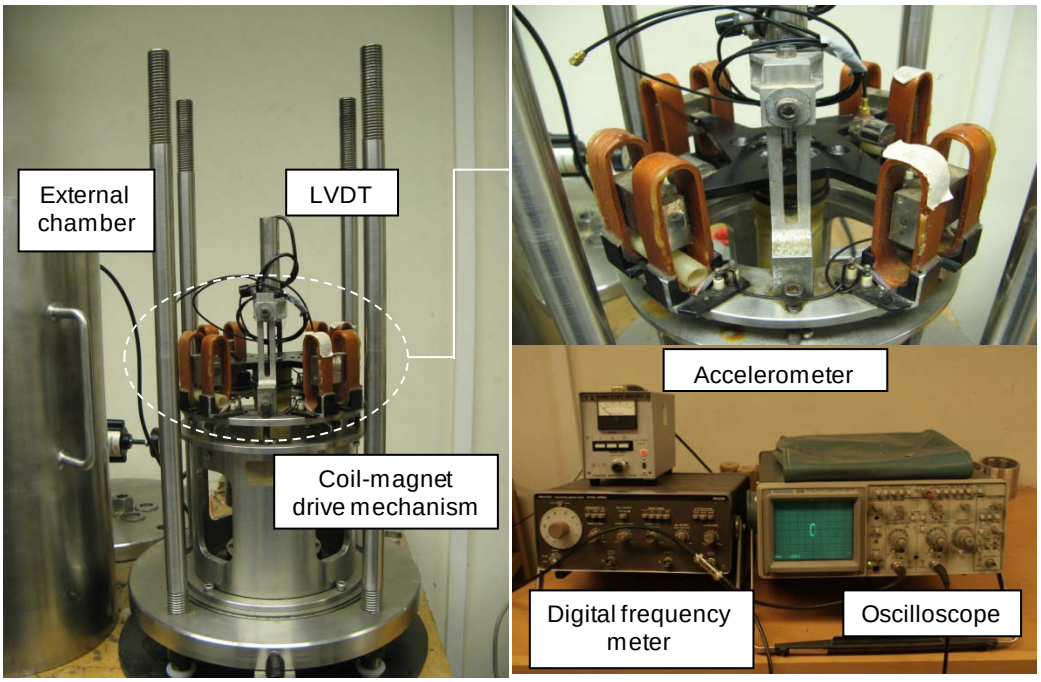

Figure 4.4 Resonant column equipment.

4.4.2 Test protocol

Two cylindrical soil samples were trimmed with approximately 38 mm in diameter and 76 mm high, one for each orientation (vertical and horizontal).

Multi-stage tests at different confining stresses, according to ASTM D4015-07 procedure, were performed on both samples.

Once the electric driving mechanism was connected and the external chamber closed, the sample was isotropically loaded to a total stress of 0.05 MPa and the frequency of excitation varied until resonance. Subsequently, the total stress was increased up to 0.2 and 0.7 MPa to perform the second and third resonant column measurements.

4.5 BENDER ELEMENTS TEST

4.5.1 Brief description of the equipment

Bender elements are used to estimate the shear elastic modulus at small strains of a soil specimen under unloaded condition by determining the velocity of propagation of a shear wave travelling through the tested sample.

The bender element transducers used were designed at the UPC Geotechnical Laboratory. The system is constituted by two polarised piezoceramic transducers (one transmitter and one receiver). An input signal is emitted by a programmable function generator attached to the transmitter element, which induces the shear wave. This wave travels through the soil specimen and causes the receiver element to vibrate, thus obtaining the arrival time of the shear wave. Input and output signals are acquired by a digital oscilloscope and the last one is amplified by an ultrasonic pre-amplifier (Fig. 4.5).

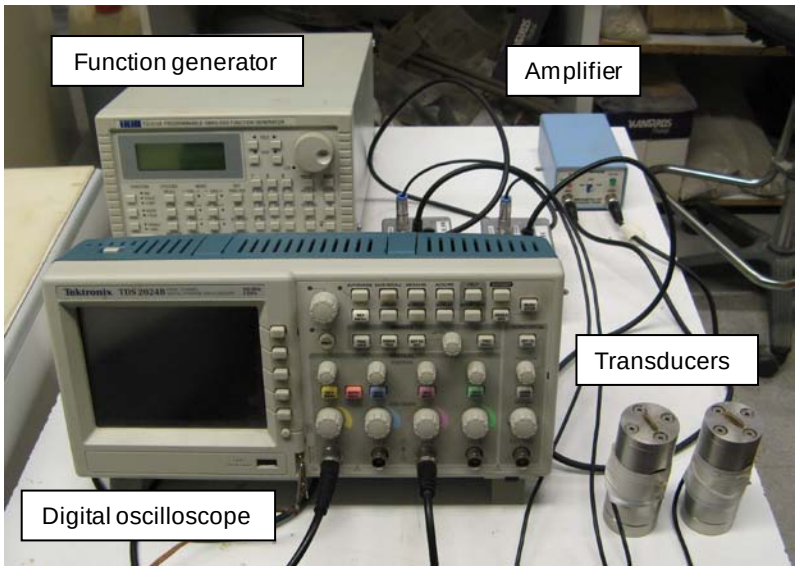

Figure 4.5 Bender elements testing equipment.

According to the elasticity theory, the low-strain shear modulus (G) can be determined as follow:

$$G = \rho V_s^2 \tag{4.6}$$

where ρ is the density of the soil sample and V_s is the shear wave velocity. This last can be determined using equation 4.7 based on the arrival time of the shear wave (t_S) travelling through the distance (l_i), commonly taken as the tip-to-tip distance between piezoceramics.

$$V_S = l_i / t_S \tag{4.7}$$

Specifications of the bender elements, calibrations and some difficulties associated with the test procedure are described in Arroyo et al. (2010).

4.5.2 Test protocol

Bender element tests were performed on the same samples tested in the resonant column equipment. To place the bender elements, slots were done on both sample ends. Particular care was taken preparing slots to minimise sample disturbance and to ensure a good alignment and contact between transducers and the soil.

Slots were performed by a X-power mini-drilling machine from *Afittol, S.L.* with a carbide coated miniature drill of 1.2 mm in diameter. To ensure the good alignment mentioned before, a copper sample-holder was also used (Arroyo et al., 2010). Figure 4.6 shows (a) the equipment used to drill the slots and (b) aspect of the sample once slots were done.

The sample was then covered with foil seal wired to the ground port of the oscilloscope and positioned between both transducers. Measurements were done using two different input frequencies (sine pulses) for each sample (vertical and horizontal orientations). The arrival time was estimated as the elapsed time between the start of voltage pulse input and the first deflection in the output signal.

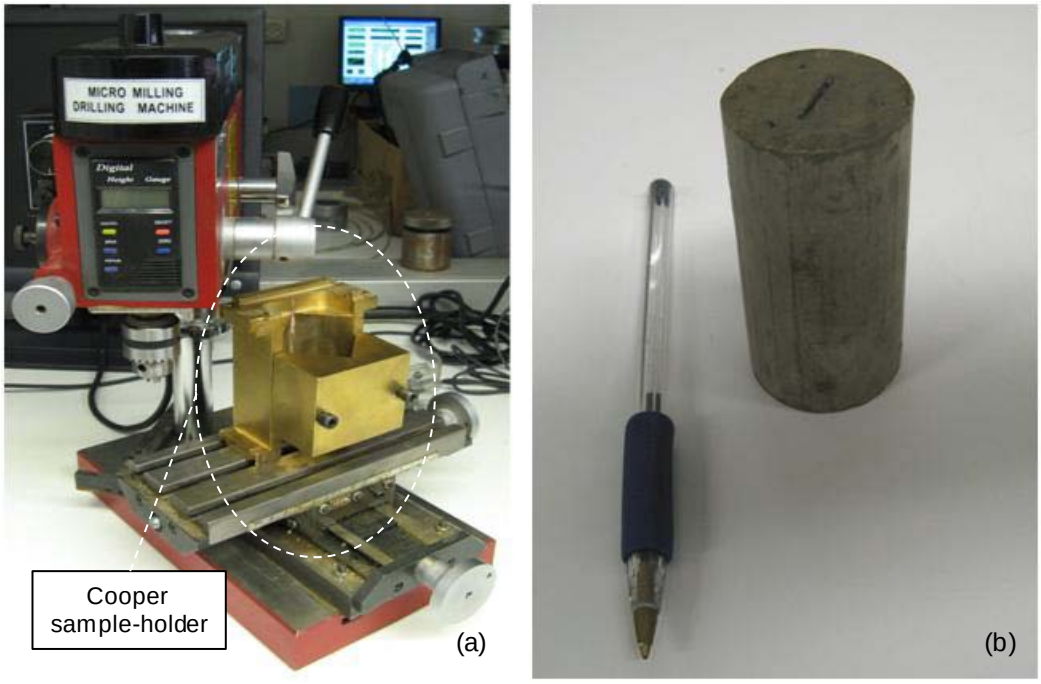

Figure 4.6 Drilling equipment and sample.

4.6 ULTRASONIC PULSE TEST

4.6.1 Brief description of the equipment

The ultrasonic pulse test provides information on the travel time of a longitudinal wave travelling through a soil specimen, which is useful to determine its low-strain Young modulus under unloaded condition.

The equipment used was a 'V-Meter-II' from *James Instruments, Inc*. Transducers are located at each end of the soil specimen, and the travel time (t_p) of a high frequency (54 kHz) and high voltage compression wave travelling alongside the sample axis is determined. With this information and the travel length of the compression wave (*l*, sample height), it is possible to determine the longitudinal wave velocity (V_L), which is used to estimate the unconfined Young modulus (E) using equations 4.8 and 4.9, where ρ is the total density (Pineda et. al, 2010).

$$V_{L=}\frac{l}{t_p} \tag{4.8}$$

$$E = \rho {V_L}^2 \tag{4.9}$$

4.6.2 Test protocol

Ultrasonic pulse tests were performed on the same samples tested first in the resonant column equipment and then with bender elements.

To minimise error on measurements, two basic recommendations were followed. First, the distance between the transducers was measured as accurately as possible and it was verified that surfaces were as smooth as possible. Second, to ensure adequate acoustic coupling of the transducers to the surface under test, a thin layer of couplant was applied between the transducer and the soil specimen. In Figure 4.7, the travel time measurement of the longitudinal wave travelling through one of the samples is displayed.

Details concerning the equipment characteristics, calibration and some recommendations associated with sample preparation are described in *James instruments, Inc.* (2011).

Figure 4.7 Ultrasonic pulse test equipment and sample.

4.7 CONTROLLED-GRADIENT WATER PERMEABILITY TESTS AT DIFFERENT TEMPERATURES USING CONSTANT VOLUME CELLS

4.7.1 Brief description of the equipment

The constant volume (isochoric) cell used in this research was developed at UPC Geotechnical Laboratory (Hoffmann, 2005). Figure 4.8 displays the main parts of the cell. Water inlet connections are located at the base and air release and water outlet ones at the top cap.

Figure 4.8 Constant volume cell pieces.

A constant piezométrica head gradient was used to induce water flow. The volume change (ΔV) per unit time (Δt) was measured using two volume/pressure controllers (GDS instruments) connected to both bottom and top caps, and registered with a data acquisition system (Fig. 4.9). Based on Darcy's law, the water permeability (k_w) can be estimated as follow:

$$k_w = \frac{q}{i} = \frac{\Delta V\ \gamma_w\ h}{\Delta t\ A\ \Delta_{pw}} \tag{4.10}$$

where γw is the water unit weigth, h is the sample heigh, A is the sample area and Δpw is the pressure difference between bottom and top ends.

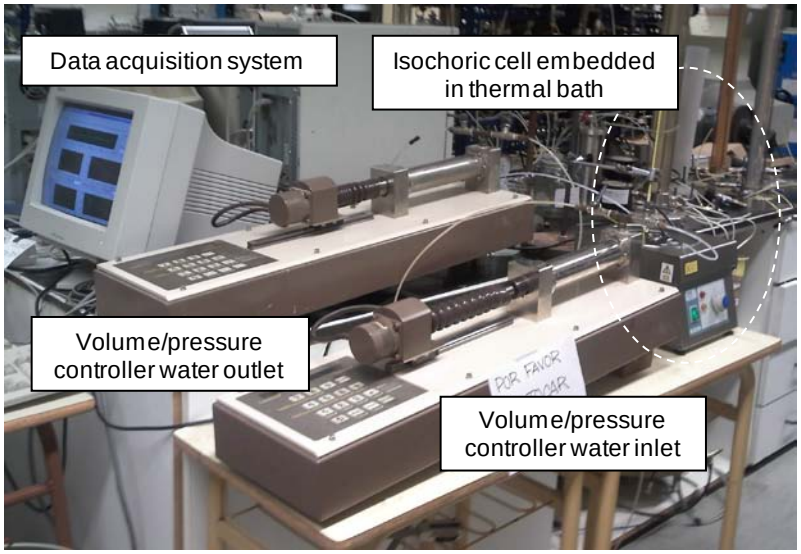

Figure 4.9 Controlled-gradient water permeability setup.

To study temperature effects, the isochoric cell was immersed in a thermal bath containing silicone oil, as shown in Figure 4.10.

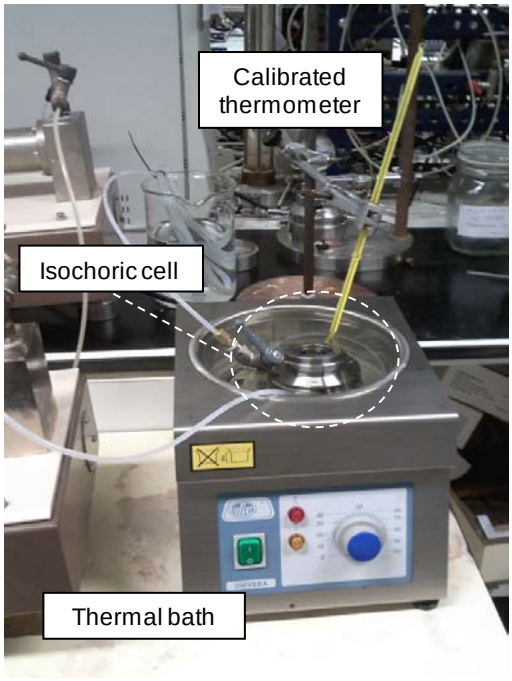

Figure 4.10 Thermal bath for water permeability determinations at different temperatures.

4.7.2 Test protocol

Once the sample was trimmed and placed into the cell ring (50 mm in diameter and 20 mm high), the top cap was adjusted to ensure the constant volume condition. The protocol followed can be divided into two stages, a first stage to ensure saturated conditions and a second one of water permeability measurement at different temperatures.

During saturation, a backpressure of 1 MPa was applied at the bottom along 6 days while maintaining the upper valve under atmospheric conditions (water outlet was observed at the top boundary ensuring saturated conditions).

In a second stage, another pressure/volume controller was connected to the upper valve and the isochoric cell was placed inside the silicone oil thermal bath to maintain thermal stability. Pressures of 1 MPa and 10 kPa were applied during water permeability measurements at bottom and top caps, respectively.

Water permeability tests were done at 22, 40, 60 and 80 ºC using the same sample. Once the desired temperature was reached, one-hour of thermal equalisation was allowed before starting the water volume change measurements.

Tests were performed in vertical (horizontal bedding planes) and horizontal sample orientations.

4.8 CONTROLLED-GRADIENT WATER PERMEABILITY TESTS AT DIFFERENT TEMPERATURES USING THE OEDOMETER CELL

4.8.1 Brief description of the equipment

To obtain water permeability measurements at different temperatures and under a constant vertical stress, a temperature and suction controlled oedometer cell developed by UPC Geotechnical Laboratory was used. The design of this oedometer cell with heating chamber is described in Romero (1999) and Lima (2011). The sample is surrounded by a silicone oil bath and a controlled-power helical electric heater of 500 W at 220 V. A programmable thermostat with type K thermocouples controls the temperature of the soil specimen.

Figure 4.11 presents the experimental layout of the equipment. Vertical stress is applied by a lever mechanism with an improved capacity of 20 MPa. Vertical displacements are measured using a LVDT. To apply the desired hydraulic conditions, a pressure/volume controller is used. These two outputs were logged by two independent data acquisition systems.

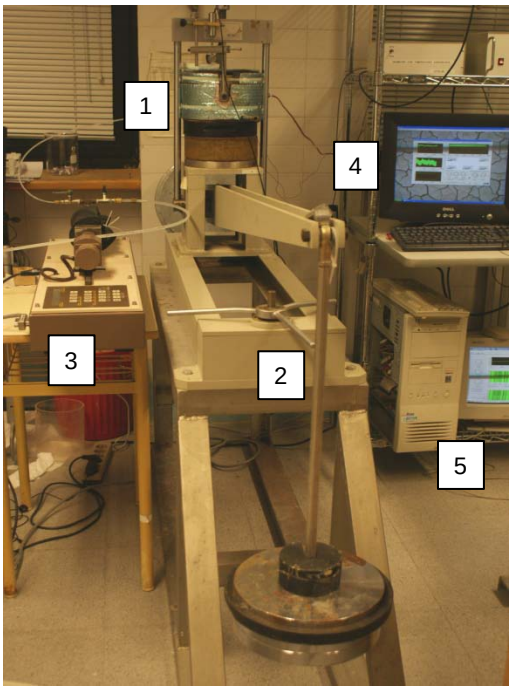

1. Temperature and suction controlled oedometer cell
2. Loading lever mechanism system
3. Pressure/volume controller
4. LVDT and temperature data acquisition system
5. Pressure/volume controller data acquisition system

Figure 4.11 Experimental layout of the equipment used to perform water permeability tests.

4.8.2 Test protocol

Horizontally and vertically oriented samples were tested (50 mm in diameter and 20 mm high). An initial vertical stress of 4MPa was applied before SYCW contact.

After one day of equalisation under a vertical stress of 4 MPa, a backpressure of 300 kPa was applied to the vertical sample orientation. After 10 days of hydration, several heating/cooling paths were performed and water permeability at different temperatures measured (refer to Table 4.1).

Table 4.1 Temperature paths followed in vertical sample orientation.

Path	Temperature (ºC)
A-B	22
	80
B-C	80
	22
C-D-E-F	22
	40
	60
	80
F-G	80
	22

For the horizontal sample orientation, an initial back pressure of 300 kPa was also applied at a vertical stress of 4 MPa. After 10 days of hydration, the vertical effective stress was increased by steps until reaching 20 MPa (steps of 10, 16, and 20 MPa) allowing for a minimum equalisation period of 24 hours between each step. Thereafter the backpressure was increased to 800 kPa until the saturated condition was reached and the water permeability at 22 ºC was measured. Then a heating/ cooling paths of 80 and 22 ºC respectively, measuring the water permeability were followed.

During all thermal paths a minimum period of equalisation of 24 hours between each thermal pulse were allowed.

4.9 STEP-LOADING/UNLOADING OEDOMETER TEST

4.9.1 Brief description of the equipment

Figure 4.12 shows the set-up of the equipment used to perform the oedometer tests with step-loading/unloading technique, which is similar to the layout described in the previous section, but without thermal control. In fact, the cell is similar to the isochoric one shown in Figure 4.8 with movable upper cap.

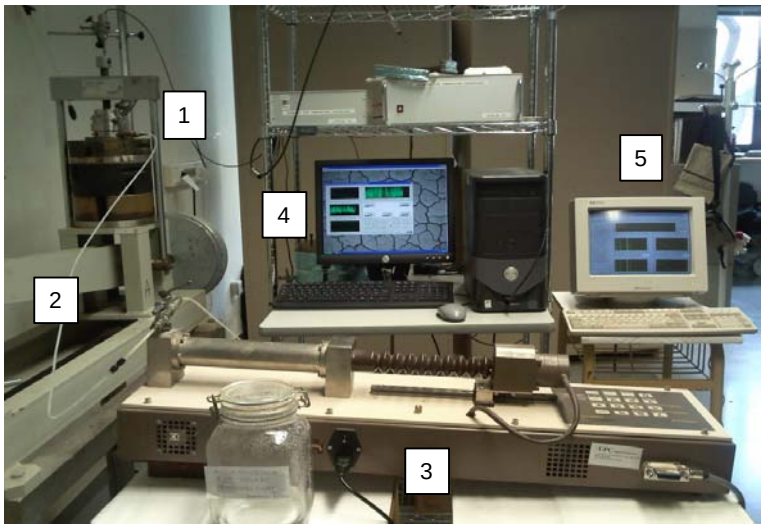

1. Oedometer cell
2. Loading lever mechanism system
3. Pressure/volume controller
4. LVDT data acquisition system
5. Pressure/volume controller data acquisition system

Figure 4.12 Set-up of the equipment used to perform step loading/unloading oedometer tests.

4.9.2 Test protocol

A trimmed sample was installed in the oedometer ring with metallic discs in both bottom and top caps. During loading and unloading paths, the bottom and top drainages were maintained open.

An initial vertical stress of 20 kPa was applied to ensure the proper contact between sample and loading system. The following steps were performed: 0.1, 1, 2, 4, 6, 10, 16, 20, 16, 10, 4 and 0.1 MPa, allowing for a minimum equalisation period of 24 hours between each step (deformation rates below 0.1%/day).

A constant backpressure of 100 kPa using SYCW was applied once sample was loaded to 4 MPa. After ensuring saturation, the water permeability at this point was measured.

Tests were performed in vertical and horizontal sample orientations. In addition, the horizontal one was subjected to another reloading and unloading cycle.

4.10 CONTINUOUS LOADING/UNLOADING OEDOMETER TESTS

4.10.1 Brief description of the equipment

To perform these tests, the temperature and suction controlled oedometer cells developed at UPC Geotechnical laboratory and described in Lima et al. (2010) and Lima (2011) were used. As shown in the scheme of Figure 4.13, the silicone oil thermal bath completely covers the oedometer cell. The thermal system is constituted by an immersion thermostat with automatic temperature control regulated by thermocouples located close to the sample.

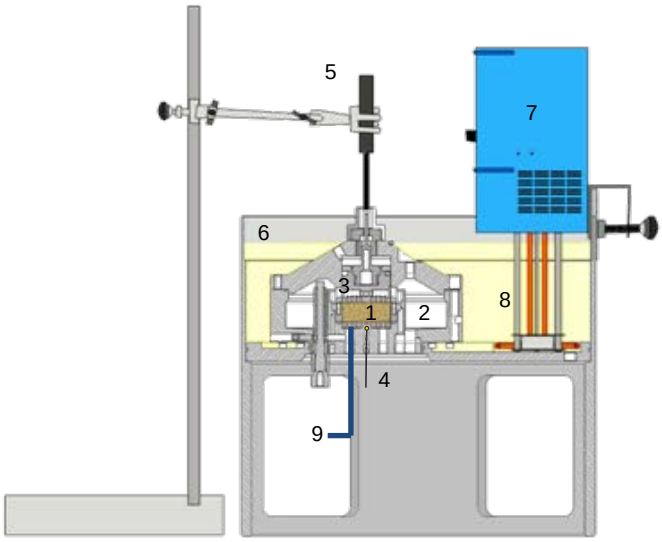

1. Soil sample
2. Annular vessel for saline solution. Capacity: 200 cm^3
3. Pneumatic axial loading piston / blocking system
4. Thermocouple
5. LVDT to monitor vertical displacements
6. Thermal bath
7. Thermostat
8. Silicone oil
9. Volume/pressure controller

Figure 4.13 Scheme of the temperature and suction controlled oedometer cell (Lima et al., 2010).

The vertical load is applied by a pneumatic axial piston with silicone oil connected to a volume/pressure controller and the vertical displacement is measure by an external LVDT that was calibrated for non-isothermal paths. Temperature and vertical displacement are recorded using a data acquisition system (Fig. 4.14). It is also possible to minimise evaporation effects using low concentration saline solutions placed in an annular vessel inside the cell (capacity of 200cm3).

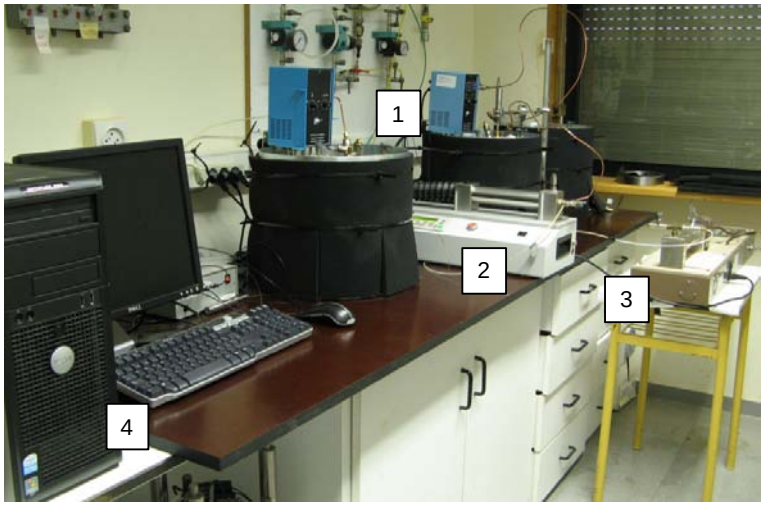

1. Temperature and suction controlled oedometer cell
2. Pressure/volume controller to apply vertical load
3. Pressure/volume controller to apply backpresure
4. LVDT and temperature data acquisition system

Figure 4.14 Set-up of the equipment used to perform continuous loading/unloading oedometer tests.

4.10.2 Test protocol

Stress-controlled continuous loading and unloading tests under saturated conditions at different temperatures (22 and 80ºC) for both sample orientations (vertical and horizontal) were performed. Samples were trimmed and placed into the odometer ring (50 mm in diameter and 20 mm high) between two metallic porous discs.

An initial vertical stress of 50 kPa was applied to ensure contact between the specimen and the loading system. Samples were continuously loaded up to 4 MPa, when a constant

backpressure of 50 kPa at bottom and top caps using SYCW was applied. After one day of equalisation, the loading stage was restarted up to a maximum vertical stress of 10 MPa and afterwards unloaded to 50 kPa.

A stress control rate of 0.46 kPa/min during loading up to 10 MPa and 0.90 kPa/min during unloading were initially used for vertical sample orientation tested at 22 ºC. Afterwards, a 0.5 kPa/min stress control rate (loading / unloading) for the remaining tests was used.

In tests performed at 80 ºC, once the backpressure was applied (at vertical stress of 4 MPa) and the equalisation period completed, the temperature was increased approximately from 22 ºC to 80 ºC in a period of 5 hours (temperature rate of 11ºC/hour). Before continuing with the loading stage, a period of 24 hours was allowed.

4.11 PULSE HEATING TEST

4.11.1 Brief description of the existing equipment

The heating cell was designed at UPC Geotechnical Laboratory to study the pore water pressure changes induced during controlled heating/cooling pulses.

A cylindrical soil sample is confined in a stainless steel ring of 75 mm in diameter and 100 mm in height and it is tightly closed with two lids screwed to the ring in bottom and top, where Viton “O”-rings ensure the hydraulic tightness. Sample is subjected to heating pulses by means of a controlled-power heater installed along the axis of the sample, in the lower part of the cell.

The ring has eight inlets that allow the installation of different types of transducers in contact with the soil specimen to monitor the soil response during the thermal load. To measure the pore water pressure and temperature evolutions, two pore water pressure transducers and two thermocouples are strategically located in four of those inlets at 25 and 75 mm from the bottom of the sample as indicated in Figure 4.15.

To apply the hydraulic conditions, two valves in both bottom and top caps of the cell were installed. In addition, porous discs of 3.0 mm thickness between the soil specimen and bottom/top lids were placed.

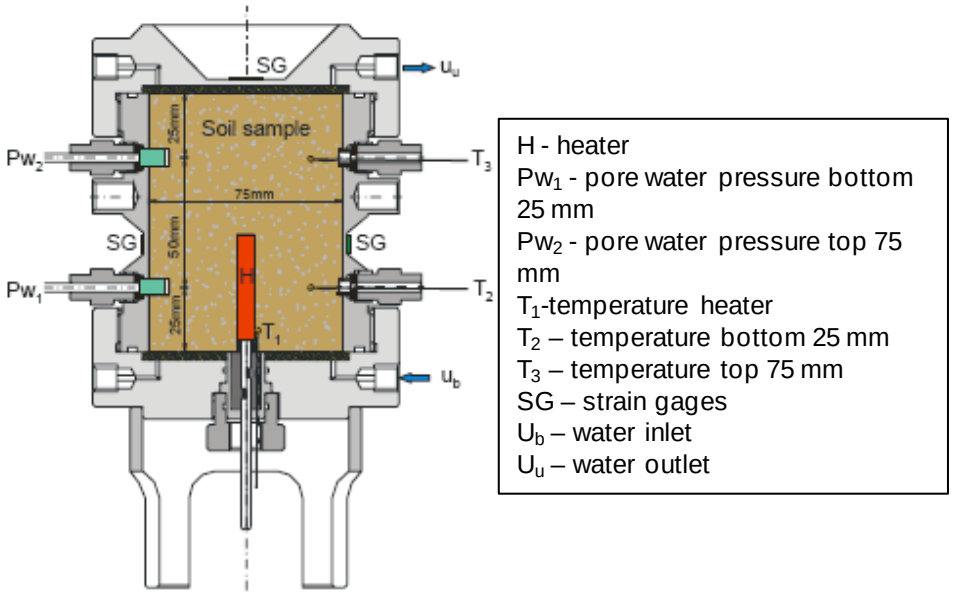

Figure 4.15 Scheme of the existing heating cell (Lima et al, 2010).

The initial configuration of the heating cell and details of the transducers used are described in Muñoz (2006). The equipment was further modified and updated by Lima (2011).

4.11.2 Update performed on the cell

Two main updates have been performed in the heating cell, namely the adaptation of new pore water pressure transducers and a new controlled-power heater with thermocouple included.

Two miniature pressure transducers from *HONEYWELL*, model A-105, designed to work in a pressure range from 0 to 5 MPa and under temperature conditions from -20 to 120 ºC were used. New adapters were designed to connect the transducers to the cell wall and to isolate the pore water pressure by special sintered filters.

As shown in Figure 4.16, the adapters are made of stainless steel to fit the transducer and the outlet hole of the cell. Between the transducer and sample, two sintered porous disc filters are included. To minimise the water volume between the filters a stainless steel cylinder is included. The hydraulic tightness is ensured by Viton “O”-rings.

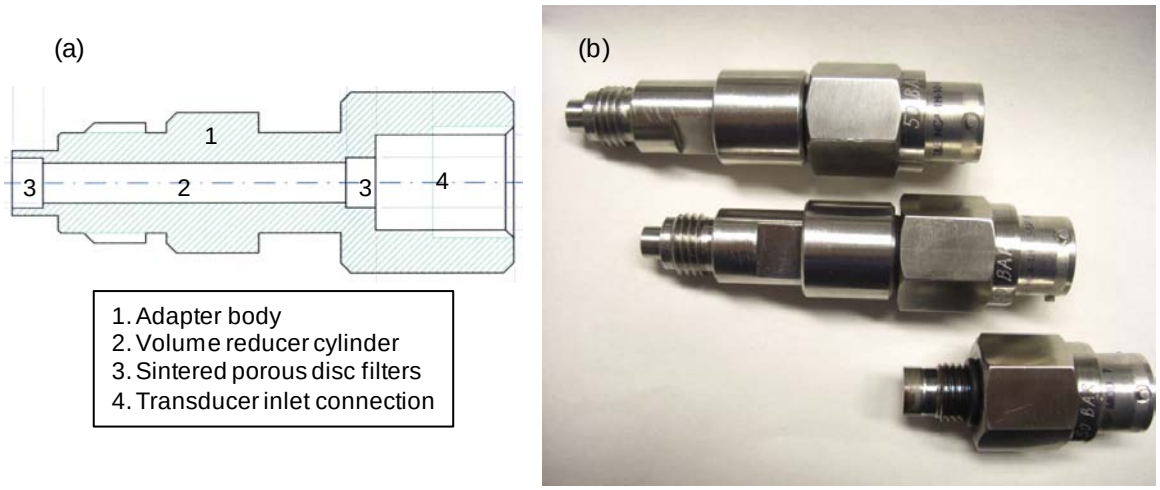

Figure 4.16 Adapters and transducers. (a) Schematic representation after Pérez (2010). (b) Photographs of the different connectors.

A new cartridge heater 6.5 mm in diameter and 40 mm length with type K thermocouple included (*Watlow*) was installed. It is connected to a power supply with variable voltage to regulate power input.

The set-up of the equipment with the updates performed in this research is shown in Figure 4.17. The hydraulic conditions are applied by two volume/pressure controllers (GDS instruments). The data acquisition system was modified to log the new transducers.

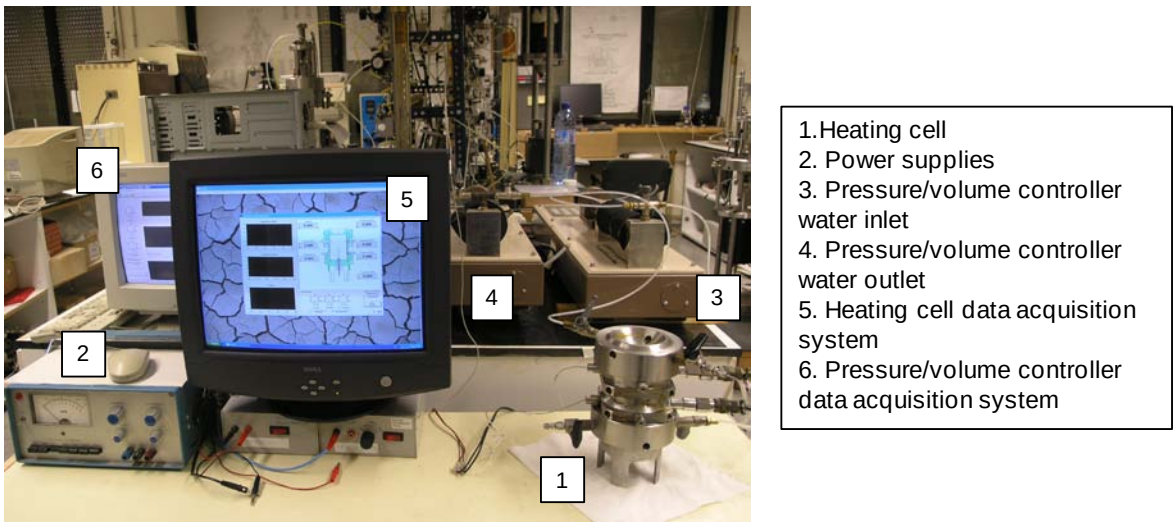

Figure 4.17 Set-up of the equipment used to perform heating pulse test.

4.11.3 Test protocol

A cylindrical sample with bedding planes perpendicular to the longitudinal axis was trimmed and placed into the cell ring (75 mm in diameter and 100 mm high). After the trimming process was completed, four holes were performed in the sample to embed thermocouples and pore pressure transducers.

An additional hole was made in the lower part of the sample to place the heater. A thin layer of silicone grease was applied along the heater-soil contact to ensure an adequate thermal conductivity.

Prior to sample preparation, wires of the thermocouple and heater were glued together with epoxy resin to avoid water leakage. Further details and recommendations for installation can be found in Muñoz (2006). To ensure hydraulic tightness, Viton “O”-rings were placed in all sensor connections.

The protocol of the test can be divided into three main phases: hydration, heating and cooling.

- Hydration phase. This phase can be also subdivided into two stages. In a first stage, the backpressure was increased in steps from 0.5 to 1 MPa (0.5 MPa for 2 days, 0.7 MPa for 5 days and 1 MPa for 7 days) with the upper valve open under atmospheric conditions. To verify the transducer readings and to eliminate possible occluded air in the transducer contact, in a second stage the upper valve was closed and a period of 10 days of transducer pressure equalisation was allowed. After this equalisation period, backpressure was increased until 1.2 MPa for 13 days. During the first stage, the water permeability under steady-state conditions was measured and determined using equation 4.10, presented in section 4.7.1.

- Heating and cooling phases. The programmed activities were to switch on the heater with controlled power input for a given period, and then switch it off for performing the cooling. However, the first heating path was interrupted due to heater failure (leakage of water damaged the heater) and it was not possible to complete the pulse program.

CHAPTER 5

EXPERIMENTAL RESULTS

5.1 MERCURY INTRUSION POROSIMETRY RESULTS

Based on Washburn equation presented in the previous chapter (Eq. 4.1), the entrance pore size, was determined. In the interpretation of the results, a surface tension σ_{Hg}= 0.484 N/m at 25ºC and a contact angle θ_{nw}=140º (usually assumed between 139º and 147º for clayey minerals; Diamond, 1970) were taken.

Further, from the volume of mercury per unit mass of solid intruded into the sample (V_{int}) it is possible to obtain information on the intruded non-wetting void ratio (e_{nw}) using the following expression:

$$e_{nw} = \rho_s V_{int} \tag{5.1}$$

where ρ_s is the density of solid particles.

Results are presented in terms of the pore size density function or frequency distribution (PSD, log differential intrusion curve versus entrance pore size), which makes easier the identification of the dominant pore modes and their evolution along the different paths followed.

As illustrated in Figure 5.1, the natural (as-retrieved) material presents two dominant pore modes, one at approximately 700 nm and another at around 80 nm. It is worth noting that distinct bimodal pore-size distributions are not common in natural soils, especially when referring to depositional and deep clay formations. In fact, natural Boom clay displays only one dominant pore mode at around 90 nm (see Appendix A).

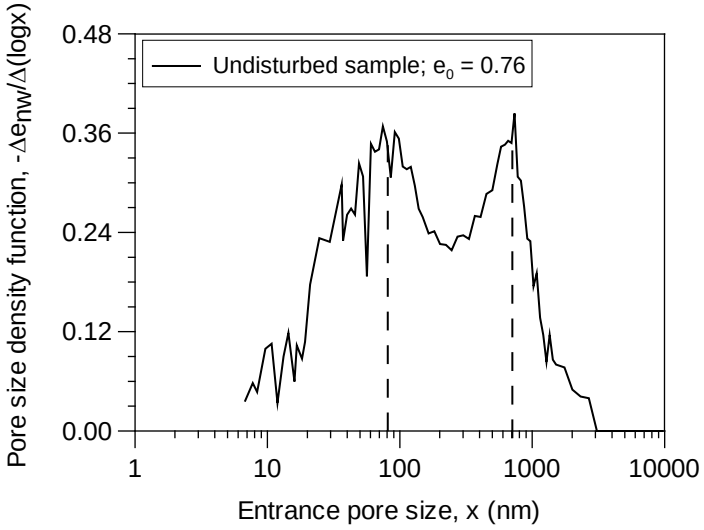

Figure 5.1 Pore size density function of undisturbed sample.

As mentioned in chapter 4, MIP samples were first subjected to a dehydrating process using freeze drying technique. To study the influence of air-drying process on the

microstructure, Figure 5.2 displays a comparison between freeze-dried and air-dried samples. It can be seen that the air-drying process does not affect the soil PSD, despite the shrinkage induced on this process.

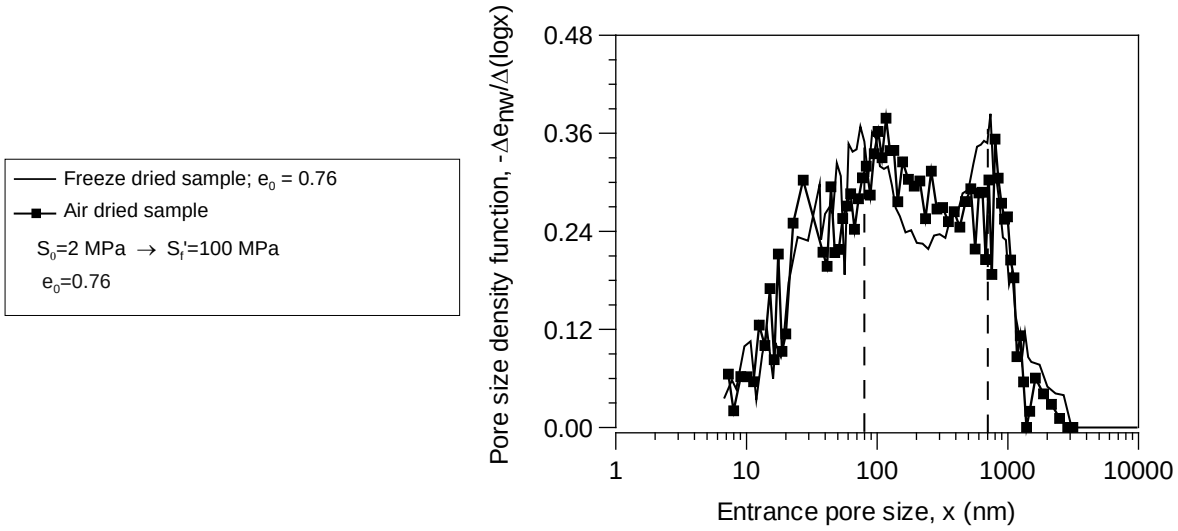

Figure 5.2 Pore size density functions of the air dried sample compared to the freeze dried sample.

To analyse the microstructural changes induced by the different paths followed, a series of MIP tests on post-mortem samples was performed. These results are presented in Figure 5.3, each one compared to the undisturbed state and briefly discussed below:

- Figure 5.3-a presents the microstructure after controlled-gradient water permeability test under constant volume using the isochoric cell at different temperatures (22, 40, 60 and 80ºC). When compared to the undisturbed sample, it is observed some increase in the macrostructure (larger pores) as a result of stress relief disturbances during sample extraction from the cell. During this process the water valves remained closed; however, it is possible that some water could have been taken from the saturated porous discs in contact with the sample.

- Figure 5.3-b displays a MIP test performed on a post-mortem sample after controlled-gradient water permeability tests following different temperatures paths and under a constant effective vertical stress of 4 MPa using odometer cell. In this case, the applied load partially reduces the macroporosity. During sample extraction, no water inlet was allowed (quasi-undrained unloading).

- Figure 5.3-c shows a MIP test carried out on a post-mortem sample tested in similar conditions than the results indicated in Figure 5.3-b but under a constant effective vertical stress of 20MPa. A significant decrease of the macro and microstructure associated with the applied load is observed. Again, during sample extraction, no water inlet was allowed (quasi-undrained unloading).

- Figure 5.3-d presents MIP results of a post-mortem sample consolidated up to 20MPa using the step-loading/unloading technique. In this case, a slightly decrease of the microporosity is detected. However, the water inlet valve remained open during sample extraction that induced an increase in the macroporosity. It is possible that for a longer

period of soil/water contact, the microporosity could also adsorb water and induce swelling.

- Figure 5.3-e shows the results of a MIP test performed after continuous loading under oedometer conditions (loading to 10MPa) at different temperatures (26-84-26ºC). The macro and microporosity are affected by the loading. These results are consistent with Figure 5.3-c, in which the sample was submitted to a higher load stress. During the sample extraction process of this test, the water inlet valve was closed.

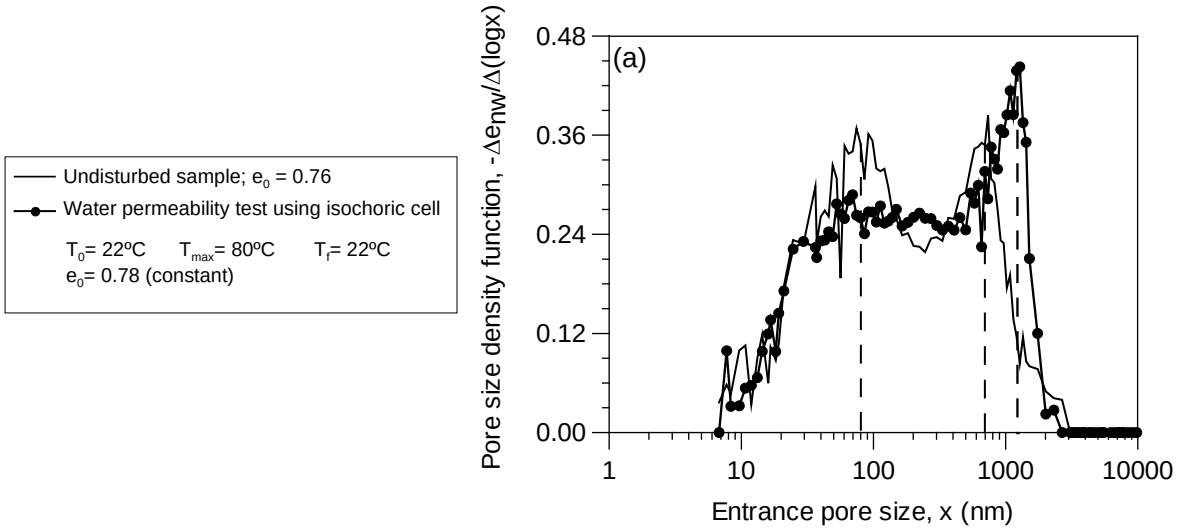

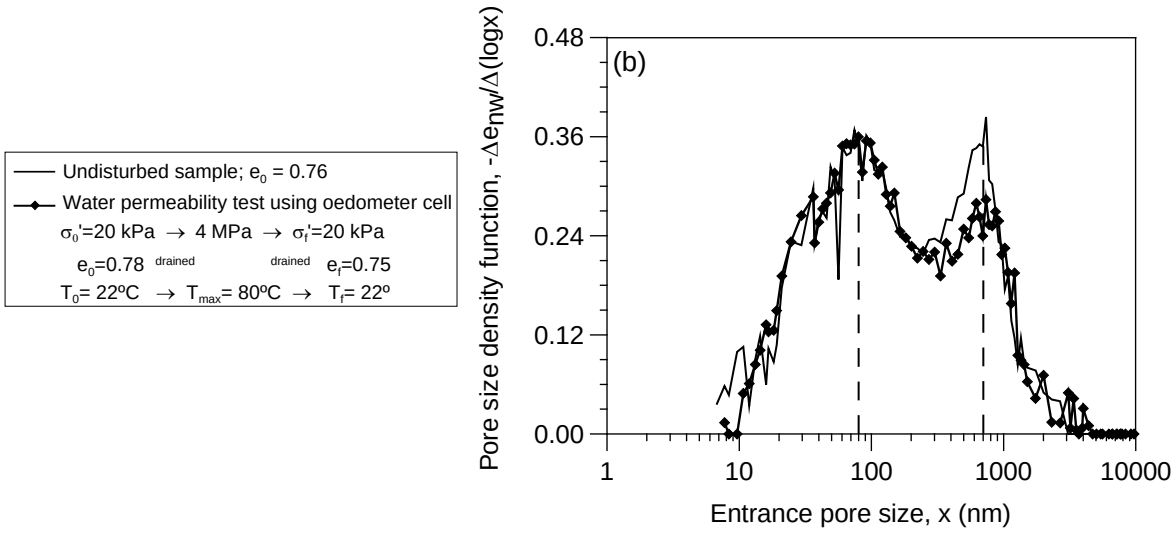

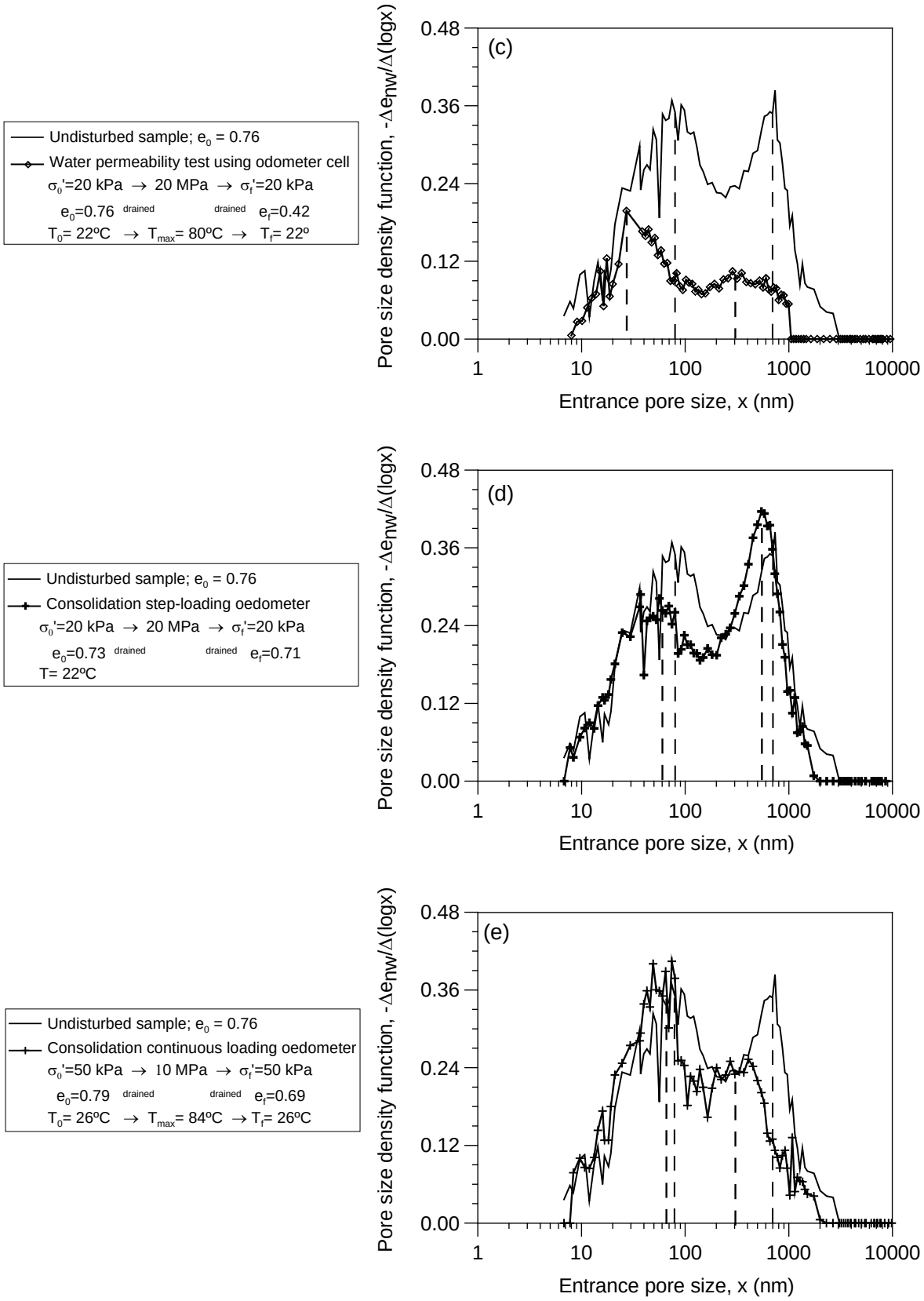

Figure 5.3 Pore size density functions of the material after undergoing different stress paths. The reference undisturbed test is included for comparison.

As illustrated in Figure 5.4, the intruded void ratio estimated under the maximum applied pressure does not coincide with the estimated void ratio of the sample. It is assumed that the non-intruded porosity (with pore sizes below 6 nm) is responsible for this discrepancy (i.e., it is assumed that the non-detected macroporosity with pore sizes larger than 400 µm is zero). Therefore, for further comparisons, PSD results were corrected by considering this constant value of the non-intruded porosity (Romero, E. (2011), Personal communication).

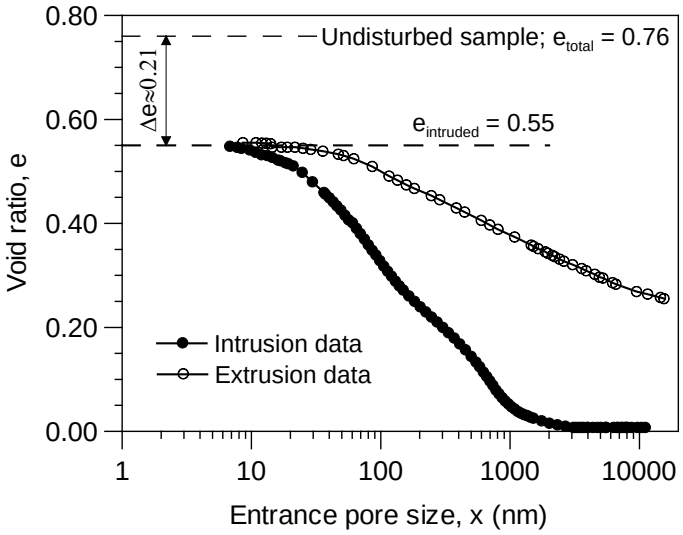

Figure 5.4 Cumulative void ratio during intrusion/extrusion cycle for the undisturbed sample.

5.2 WATER RETENTION CURVE

The water retention properties have been widely studied to get a better insight into the coupled hydro-mechanical response of the material. This curve is affected by porosity and pore size distribution changes, by the mineralogical composition, and by the hydraulic paths followed (drying and wetting).

In this section, the water retention curve of the material obtained under unstressed conditions by WP4 psychrometer measurements and back-analysis from MIP results is briefly discussed. For comparison with Boom clay, refer to the Appendix A.

5.2.1 Chilled-mirror dew-point psychrometer results

As shown in Figure 5.5, the material presents an important water retention capacity in wetting and drying paths associated with the high smectite content present in the clay fraction (see Appendix A for comparison with less active Boom clay). It also appears that Ypresian clay loses slightly larger water content (from the water storage capacity at saturation) compared to Boom clay, due to early desaturation effects at relatively low total suctions. This fact could be associated with the double porosity network and the larger pores detected on the undisturbed Ypresian material (section 5.1). In fact, this can explain why Ypresian clay presents a lower initial suction compared to Boom clay despite being retrieved at a larger depth (see Appendix A).

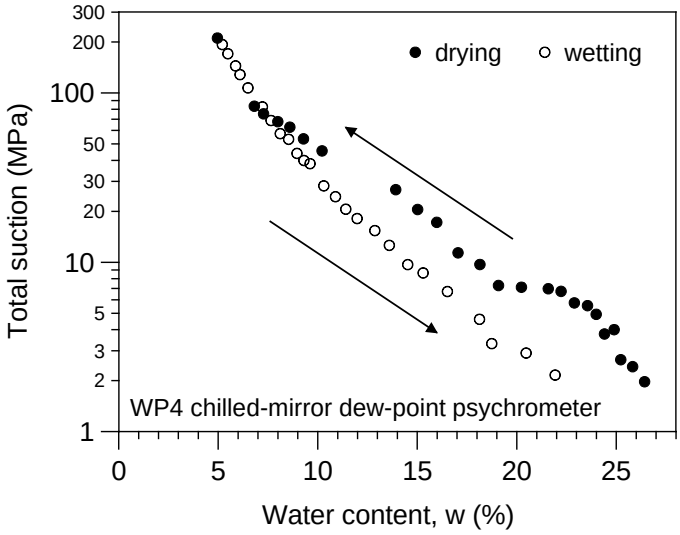

Figure 5.5 Water retention curve from psychometric measurements.

5.2.2 MIP-retention curve relationship

MIP results can be used to quantitatively derive the matric suction-saturation or water content relationships based on the assumption that mercury intrusion process is similar to air-intrusion during the desorption path of the water retention curve (Romero, 1999; Romero and Simms, 2008).

Based on previous considerations, the volume of pores not intruded by mercury can be used to evaluate the water content corresponding to the equivalent applied matric suction as follows:

$$Sr_{nw} + Sr = 1 \; ; \; w = w_{sat} \; (1 - Sr_{nw}) \tag{5.2}$$

where Sr is the degree of saturation and w_{sat} the water content at Sr=1. The degree of saturation of the non-wetting mercury, $Sr_{nw,}$ is determined using the following expression, where e_{nw} is the intruded void ratio by mercury and e_o is the initial void ratio:

$$Sr_{nw} = \frac{e_{nw}}{e_o} \tag{5.3}$$

Moreover, the relationship between the equilibrium mercury intrusion *p* and matric suction ($u_a - u_w$) can be obtained as follows (Romero, 1999):

$$(u_a - u_w) = \frac{4\,\sigma\,cos\,\theta_w}{x} \; ; \; p = -\frac{4\,\sigma_{Hg}\;cos\,\theta_{nw}}{\mathrm{x}} \tag{5.4}$$

$$(u_a - u_w) = -\frac{\sigma\,cos\,\theta_w}{\sigma_{Hg}\;cos\,\theta_{nw}}\,p \approx 0.196\,p$$

where σ is the water surface tension and $\cos\theta_w$=1 is the wetting coefficient for the air-water interface (σ_{Hg} and θ_{nw} are the equivalent values for mercury, which were given above).

Figure 5.6 displays the drying branch of the water retention curves estimated from MIP results and in terms of water content. It can be observed that the air-entry value associated with the macroporosity is around 0.4 MPa. This fact explains some of the early desaturation effects observed on Ypresian clay, and the relatively low initial total suction measured despite being retrieved at a larger depth. A more comprehensive analysis of the material water retention properties and the relationship with its microstructure can be found in Lima et al (2011) (see Appendix A).

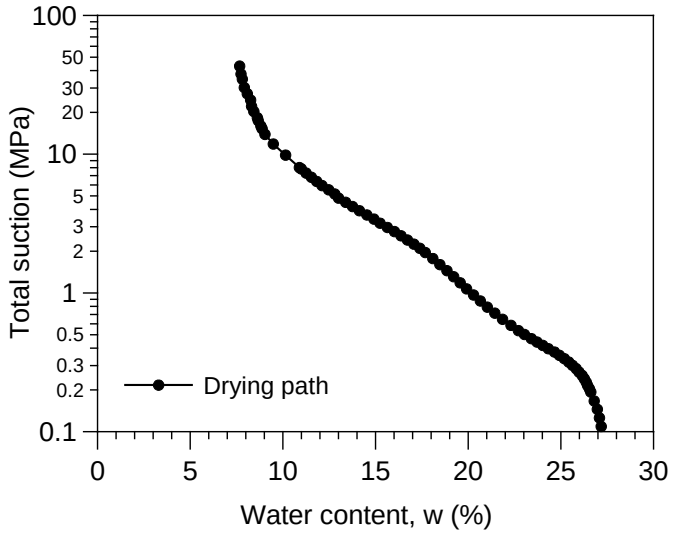

Figure 5.6 Water retention curve estimated from MIP data.

5.3 WATER PERMEABILITY RESULTS

The interpretation of temperature effects on water permeability in saturated soil is usually based on viscosity changes under free water considerations. According to Romero (1999) the relative water permeability due to temperature effects k_T based on viscosity changes can be estimated as follows:

$$k_T(T)|_{e,w} = \frac{\rho_w(T)\mu_w(T_0)}{\rho_w(T_0)\mu_w(T)} \approx 1 + \beta_T(T - T_0);\ T_0 = 22^oC \qquad (5.5)$$

where μ_w is the absolute viscosity and $\beta_T \approx 0.030\ C^{-1}$ is an empirical coefficient that fits relative viscosity data over the temperature range of 22º C $\leq T \leq$ 80º C.

5.3.1 Water permeability results from samples tested under constant volume condition

In Figure 5.7, vertical (k_{wv} - horizontal bedding planes) and horizontal (k_{wh} - vertical bedding planes) water permeability results including the water viscosity prediction are presented. This soil presents a slight anisotropy ($k_{wh} > k_{wv}$). In addition, it can be seen that the water permeability measured at different temperatures is higher than the water viscosity prediction in both directions.

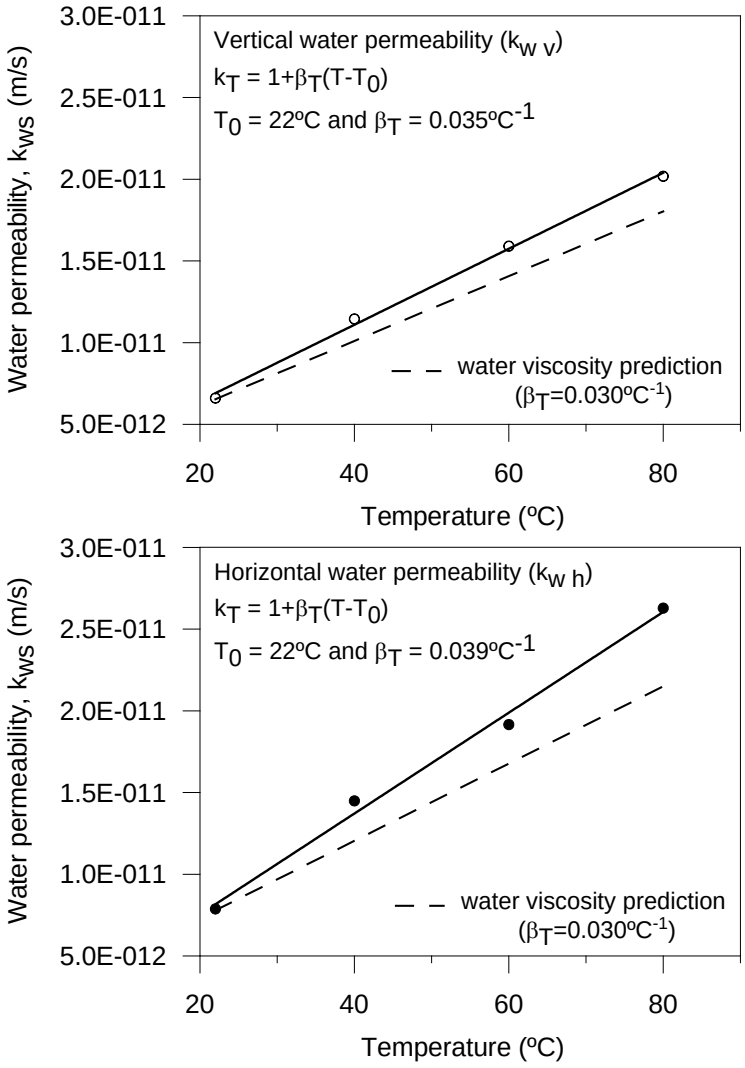

Figure 5.7 Vertical (k_{wv}) and horizontal (k_{wh}) water permeability results obtained from samples tested in the isochoric cell.

5.3.2 Water permeability results from samples tested under a constant vertical stress

Figure 5.8 shows the vertical controlled-gradient water permeability values measured at different temperatures and under a constant total stress of 4MPa. The prediction for different temperatures based on viscosity changes under free water considerations is also presented. It can be seen that β_T (water permeability slope for different temperatures), compared with viscosity changes under free water considerations (β_T=0.030ºC^{-1}), is slightly higher in all paths. It appears that progressive heating/ cooling cycles, do not affect the material water permeability properties exhibiting a clear reversible behaviour. Nevertheless, further cycles are needed to verify this conclusion.

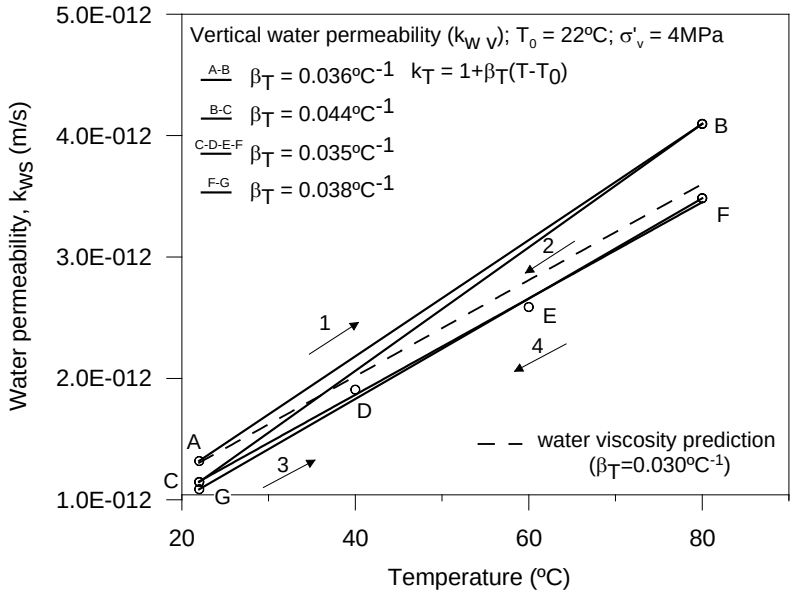

Figure 5.8 Vertical controlled-gradient water permeability measured during different temperatures under constant effective stress of 4MPa.

As shown in Figure 5.9, in the case of the horizontal water permeability measured at different temperatures under a constant total stress of 20MPa, the water permeability results at 22 ºC are lower compared to the vertical sample as a result of the applied stress. Water permeability slope for the first path AB is larger than 0.030ºC^{-1}, which probably is affected by certain uncertainty on the water permeability measured at A. The second path BC tends to a lower thermal sensitivity value tending to the water viscosity prediction under free water considerations. Further cycles are required to verify if this last slope is maintained or still reduces with the progression of cycles. The dependence of the water permeability at 22 ºC with void ratio is discussed on section 5.5.1

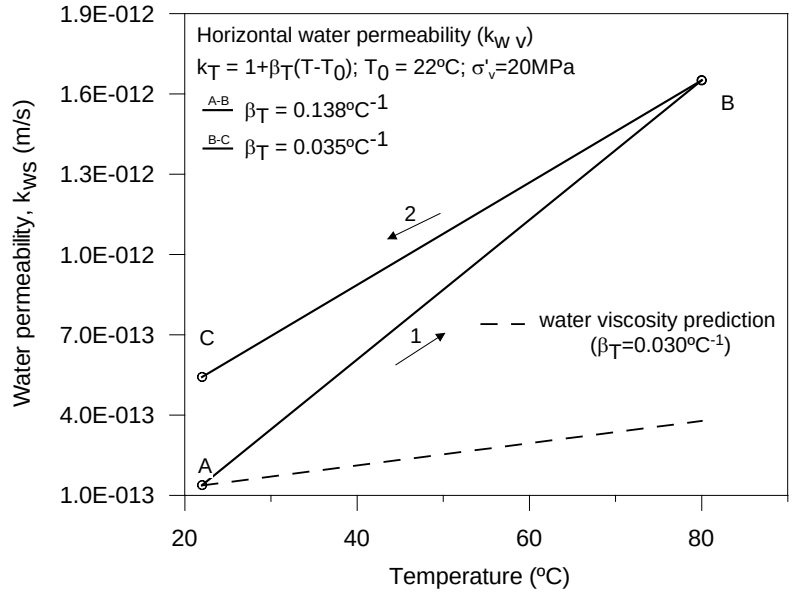

Figure 5.9 Horizontal controlled-gradient water permeability measured during different temperatures under constant total stress of 20 MPa.

Table 5.1 summarizes the controlled-gradient water permeability results on vertical (σ_v = 4 MPa) and horizontal sample orientations (σ_v = 20 MPa) compared with those obtained from tests performed under constant volume conditions.

Table 5.1 Summary of the controlled-gradient water permeability results.

Vertical sample orientation			
Path	Temperature (ºC)	Water permeability, k_{ws} (m/s)	
		σ_v'= 4 MPa (e_0 = 0.75)	Isochoric cell (e = 0.77, constant)
A-B	22	1.32E-12	6.61E-12
	80	4.10E-12	2.02E-11
B-C	80	4.10E-12	2.02E-11
	22	1.15E-12	6.61E-12
C-D-E-F	22	1.15E-12	6.61E-12
	40	1.91E-12	1.14E-11
	60	2.59E-12	1.59E-11
	80	3.48E-12	2.02E-11
F-G	80	3.48E-12	2.02E-11
	22	1.09E-12	6.61E-12
Horizontal sample orientation			
Path	Temperature (ºC)	Water permeability, k_{ws} (m/s)	
		σ_v'= 20 MPa (e_0 = 0.42)	Isochoric cell (e = 0.78, constant)
A-B	22	1.39E-13	7.88E-12
	80	1.65E-12	2.63E-11
B-C	80	1.65E-12	2.63E-11
	22	5.43E-13	7.88E-12

5.4 STIFFNESS MODULI

Low-strain shear moduli (G_0) were determined to analyse the material stiffness response. Resonant column test at constant water content were performed to obtain low-strain shear modulus variation under confined conditions on a wide range of small shear strains≤ 10^{-3} %, whereas bender elements allows to estimate G_0 values at a shear strain range lower than 10^{-5}%. Young's modulus was determinate by means of ultrasonic pulse test with compression wave. In this last case, the water stiffness is affecting the material stiffness response due to the elevated degree of saturation of the material.

5.4.1 Low-strain shear modulus

5.4.1.1. Resonant column results

Figure 5.10 displays the low-strain shear modulus plotted against the shear strain obtained from resonant column tests in both vertical and horizontal sample orientation. As observed, the shear stiffness consistently increases with confining stress. In addition, the G_0 values are slightly lower in the horizontal direction.

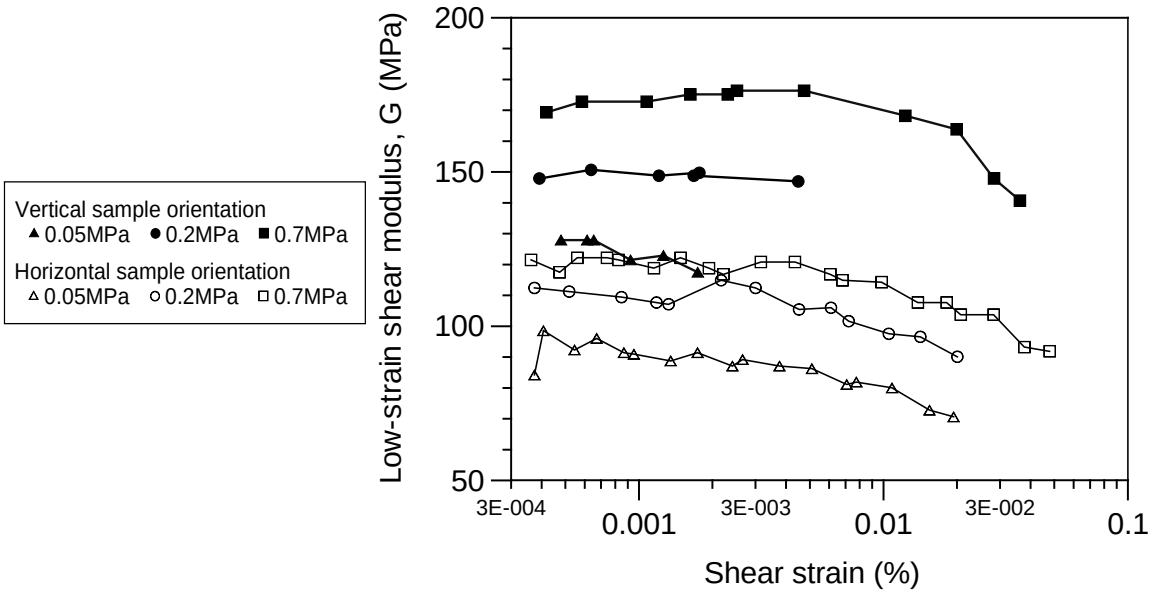

Figure 5.10 Variation of shear modulus G_0 with stress level at vertical and horizontal sample directions.

5.4.1.2. Bender element results

Results of bender element tests performed in vertical and horizontal sample orientations are summarised in Table 5.2. Low-strain shear modulus range results are consistent with those obtained from resonant column tests. Nevertheless, in this case G_0 values are slightly higher in the horizontal direction showing an opposed trend compared to resonant column results. It appears that no important anisotropy effects are detected on regard low-strain shear stiffness.

Table 5.2 Bender element test results.

Sample orientation	Frequency (kHz)	*h* (mm)	ϕ (mm)	Mass (*g*)	V (cm^3)	ρ_t (Mg/m^3)	l_i (mm)	t_S (μs)	Vs (m/s)	G_0 (MPa)
Vertical	10	75.16	38.19	168.86	86.09	1.96	67.16	230	292	167
	5							300	224	98
Horizontal	8	75.07	37.49	159.98	82.85	1.93	67.07	200	335	217
	4							240	279	151

5.4.2 Young modulus under unloaded condition

Table 5.3 presents ultrasonic pulse test result with compression wave obtained on vertical and horizontal sample orientations. These high Young moduli (around one order of magnitude higher) can be associated with the additional compression stiffness provided by water due to the high degree of saturation of the material. Again, a larger stiffness in the horizontal direction is obtained. To better define the trend and the anisotropic response, new tests need to be performed in vertical and horizontal sample orientations.

Table 5.3 Ultrasonic pulse test results.

Sample orientation	*h* (mm)	ϕ (mm)	Mass (*g*)	V (cm^3)	ρ_t (Mg/m^3)	t_p (μs)	V_L (m/s)	E (MPa)
Vertical	72.60	38.19	162.38	83.15	1.95	75.5	962	1806
Horizontal	74.13	37.49	156.77	81.81	1.92	54.4	1363	3559

5.5 THERMO-HYDRO-MECHANICAL OEDOMETER RESULTS

5.5.1 Step-loading/unloading results

Step-loading/unloading results (room temperature) at vertical and horizontal sample orientations in terms of volumetric strain versus vertical total / effective stress are shown in Figure 5.11 and Figure 5.12, respectively. Figure 5.13 complements the information on further reloading/unloading paths performed on horizontal sample orientation. Figure 5.14 shows the volume change comparison between both sample orientations.

Values of the compressibility parameter for both loading (at maximum post-yield conditions) and unloading (at initial unloading elastic conditions), defined as $\delta\varepsilon_v / \delta \ln(\sigma'_v)$, are shown in Figure 5.14. As observed in Figure 5.14, the compressibility parameters for loading and unloading are similar for both vertical and horizontal sample orientations. When comparing vertical and horizontal sample orientations, it appears that yielding occurred at a slightly lower stress for the horizontally oriented sample. As observed in Figure 5.13, on re-loading the compressibility (0.042) is larger than on first and second unloading (0.011 and 0.016, respectively). It is expected that on further post-yield loading the re-loading compressibility will attain a compressibility of 0.091.

Clear pre-yield (first loading and unloading) and post-yield (virgin loading) behaviour can also be identified in the curves plotted in Figure 5.14 for both sample orientations. However, care was taken in following a systematic procedure to identify the yield stress based on the cumulative volumetric work input per unit volume, as described in Romero 1999. Assuming an oedometer stress state defined by (σ_v-u_w), the work input to a saturated soil per unit of initial volume δW can be expressed as (Houlsby 1997):

$$\delta W = (\sigma_v - u_w)\delta\varepsilon_v \tag{5.6}$$

where positive compression results in positive work input. Figure 5.15 presents the evolution of the cumulative work input per unit volume versus the logarithm of the effective stress. The yield point was identified by the intersection of linear extrapolations of the pre and post-yield zones. A yield stress of approximately (σ_v-u_w) = 5.7 MPa and (σ_v-u_w) = 5.0 MPa were identified for the compression curves of vertical and horizontal sample orientations, respectively.

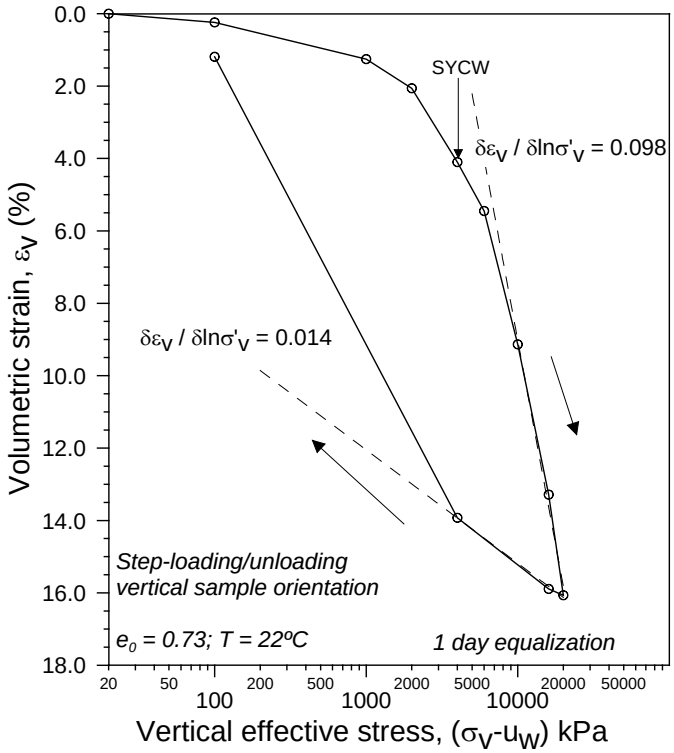

Figure 5.11 Step-loading/unloading paths at vertical sample orientation (room temperature).

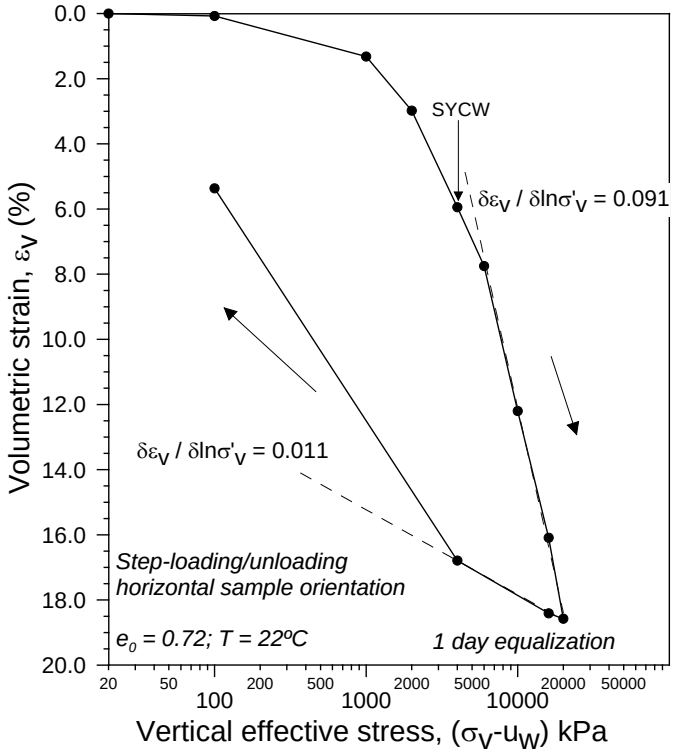

Figure 5.12 Step-loading/unloading paths at horizontal sample orientation (room temperature).

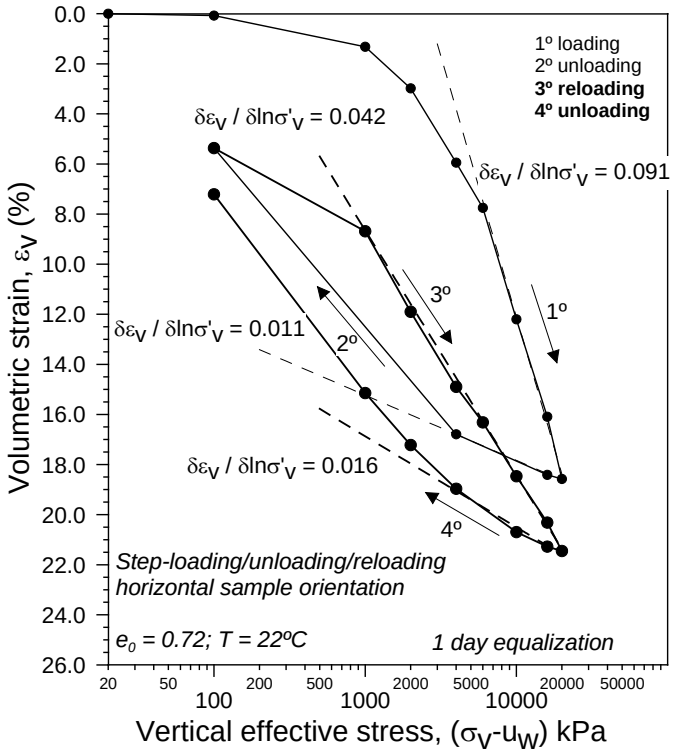

Figure 5.13 Step-loading/unloading/reloading on horizontal sample orientation (vertical bedding planes).

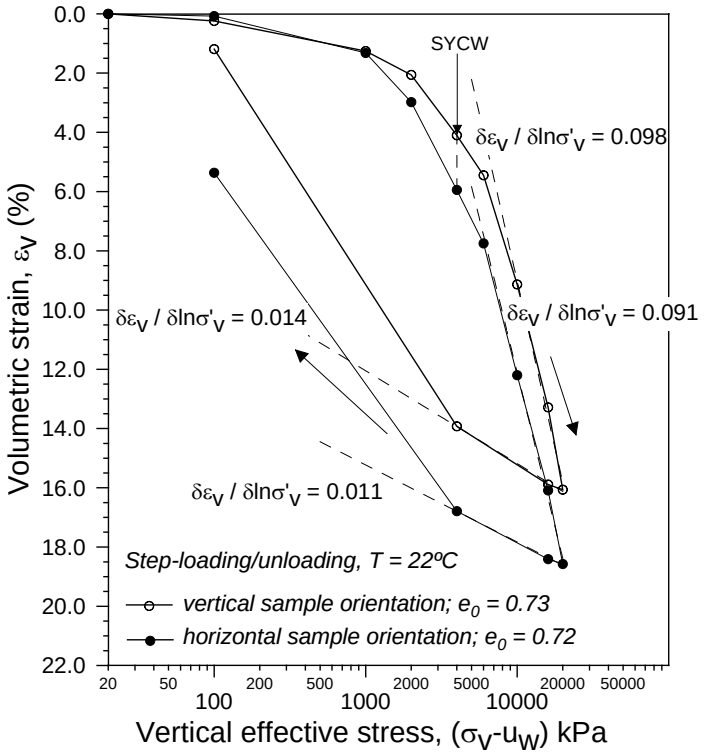

Figure 5.14 Comparison between vertical and horizontal sample orientations in step-loading/unloading tests.

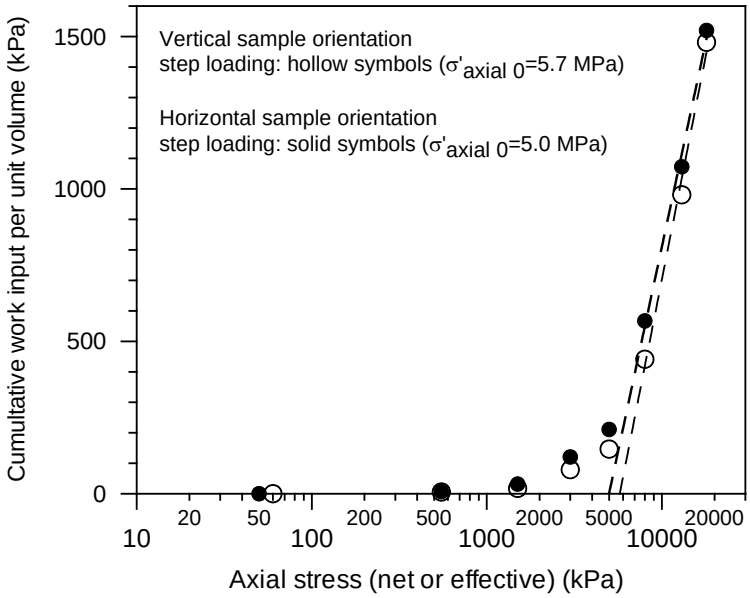

Figure 5.15 Cumulative work input per unit volume versus logarithm of total(net)/effective stress in step loading/unloading oedometer tests.

Figure 5.16 shows the time evolution of soil deformation undergone on the loading stages that were performed with water contact at a given pressure (in both vertical and horizontal sample orientations). In addition, the time evolution of soil deformation was interpreted using a non-linear curve-fitting algorithm to systematically determine the different parameters used in the primary consolidation analysis following Terzaghi's theory (Das, 1983). The soil vertical strain ε_v undergone by an vertical effective stress increment $\delta(\sigma_v - u_w)$ can be expressed as:

$$\varepsilon_v = \varepsilon_{v0} + \frac{1}{E_k'}\delta(\sigma_v - u_w)\,\bar{U}(t, C_v) + C_\alpha \log(t/t_{90}) \quad (5.7)$$

where ε_{v0} is the immediate deformation mainly due to equipment deformability and air entrapment, E_k' the drained constrained modulus, $\bar{U}(t, C_v)$ the average degree of consolidation that is a function of time t and the coefficient of consolidation C_v (Das, 1983), C_α the coefficient of secondary consolidation (creep under constant effective stress), and t_{90} the time required for 90% of average primary consolidation.

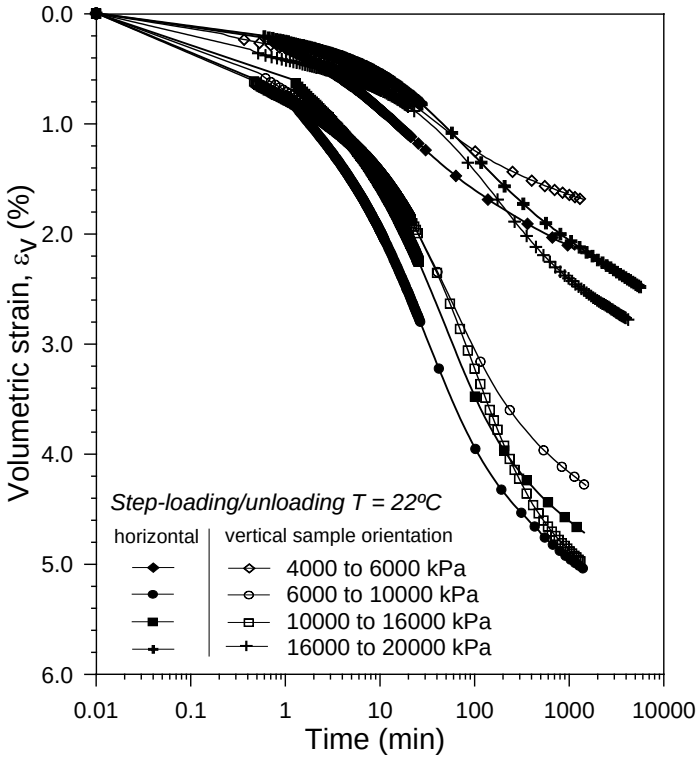

Figure 5.16 Time evolution of soil deformation on loading stages performed with water contact and known pressure in both vertical and horizontal orientations. Fitted consolidation curves according to Eq. (5.7).

Tables 5.4 and 5.5 present the different fitted parameters, which were classified according to the different loading stages at vertical and horizontal sample orientations. The fitted consolidation curves are depicted in Figure 5.16. Regarding C_v data, values on vertical and horizontal sample orientations are similar during de loading path. Likewise, C_α values are practically equal for both orientations. Low values of $C_\alpha \leq 0.006$ indicate a medium-low secondary compressibility (Mesri 1973).

Figure 5.17 shows the water permeability under saturated conditions k_{ws} for vertical and horizontal sample orientations. It can be seen that k_{ws} (for a vertical effective stress of 4 MPa) is higher for the horizontal orientation (k_{ws}=6.14x10^{-12} m/s) compared to the vertical one (k_{ws}=2.71x10^{-12} m/s). In addition, saturated water permeability values k_{ws} can be indirectly estimated from consolidation data, according to the following expression that is based on Terzaghi's theory of the rate of consolidation (Das, 1983)

$$k_{ws} = \frac{1}{E_k'} C_v \gamma_w \tag{5.8}$$

where γ_w = 9.8 kN/m^3 is the unit weight of water.

Water permeability values for the different loading stages with water contact for vertical and horizontal orientations are presented in Table 5.4 and 5.5, respectively. As observed, k_{ws} is consistently slightly larger for the horizontal orientation (vertical bedding planes). Figure 5.18 summarises the water permeability results under saturation obtained from step-loading/unloading oedometer tests (at a vertical effective stress of 4 MPa and from consolidation back-analysis) and those obtained from water permeability tests as a function of the corresponding void ratios.

Table 5.4 Primary and secondary consolidation parameters for vertical sample orientation.

Primary and secondary consolidation parameters				
Fitted parameters	4 MPa to 6 MPa	6 MPa to 10 MPa	10 MPa to 16 MPa	16 MPa to 20 MPa
δ_0 (μm)	28	82	92	62
E_m (MPa)	287	146	173	442
C_v (mm^2/s)	7.2×10^{-2}	1.9×10^{-2}	1.1×10^{-2}	2.9×10^{-2}
t_{90} (min)	26	101	173	64
C_α	0.5×10^{-2}	1.0×10^{-2}	1.0×10^{-2}	0.9×10^{-2}
k_{ws} (m/s)	2.5×10^{-12}	1.3×10^{-12}	6.1×10^{-13}	6.5×10^{-13}
e (average)	0.65	0.61	0.54	0.48

Table 5.5 Primary and secondary consolidation parameters for horizontal sample orientation.

Primary and secondary consolidation parameters				
Fitted parameters	4 MPa to 6 MPa	6 MPa to 10 MPa	10 MPa to 16 MPa	16 MPa to 20 MPa
δ_0 (μm)	10	83	68	32
E_m (MPa)	179	119	182	673
C_v (mm^2/s)	7.7×10^{-2}	2.7×10^{-2}	1.7×10^{-2}	6.5×10^{-2}
t_{90} (min)	25	69	110	29
C_α	0.6×10^{-2}	1.0×10^{-2}	1.0×10^{-2}	0.8×10^{-2}
k_{ws} (m/s)	4.2×10^{-12}	2.2×10^{-12}	9.2×10^{-13}	9.4×10^{-13}
e (average)	0.6	0.55	0.48	0.42

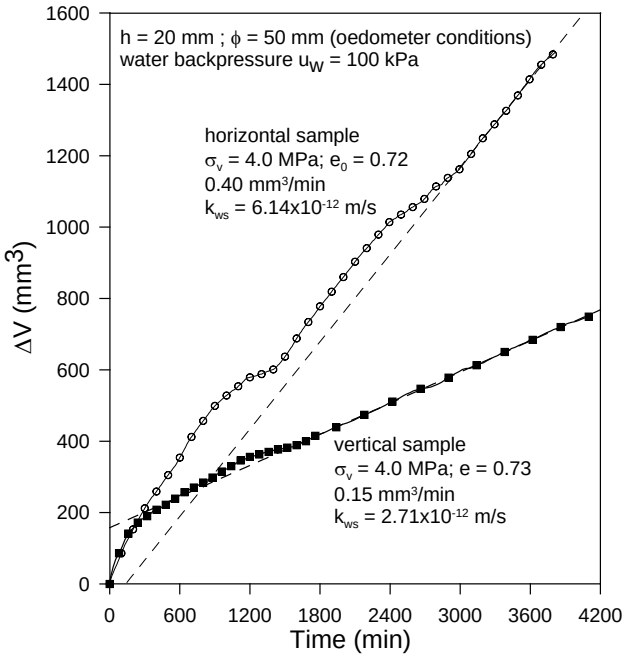

Figure 5.17 Water permeability under saturated conditions measured during oedometer tests for vertical and horizontal orientations (constant vertical effective stress of 4 MPa and at room temperature).

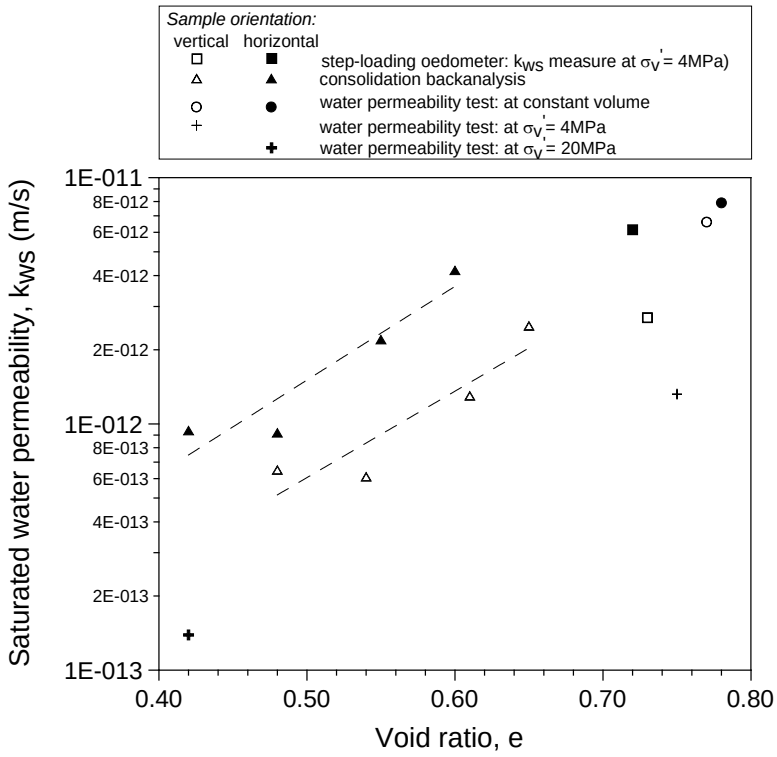

Figure 5.18 Comparison between water permeability results measured and those estimated from consolidation back-analysis.

5.5.2 Continuous loading/unloading results (T=22 and 80ºC)

Figure 5.19 shows continuous loading/unloading results (room temperature) on vertical oriented samples in terms of the variation of volumetric strain with vertical effective stress. A stress control rate of 0.46 kPa/min during loading up to 10 MPa and 0.90 kPa/min during unloading were used. At given vertical effective stresses of 4, 6.9 and 10MPa, the material was allowed equalising: volumetric strains of 0.14% (3 days equalisation), 0.31% (1 day equalisation) and 0.31% (2 days equalisation) were measured at these respective vertical effective stresses. Taking into account, a 0.5 kPa/min stress control rate (loading / unloading) for the remaining tests was used.

Figure 5.20 presents the comparison between the vertical and horizontal sample orientations at room temperature. Values of the compressibility parameter for both loading and unloading conditions at vertical and horizontal sample orientations, defined as $\delta\varepsilon_v / \delta\ln(\sigma'_v)$, are also shown in the figure. Similar compressibility parameters are obtained for both orientations. The last unloading stage (below 1 MPa), the volume change response is affected by the experimental system (viscosity effects of silicone oil in the lines connecting loading piston and pressure/volume controller). This way, only the first unloading stage (up to approx. 1 MPa) is considered representative of the material response.

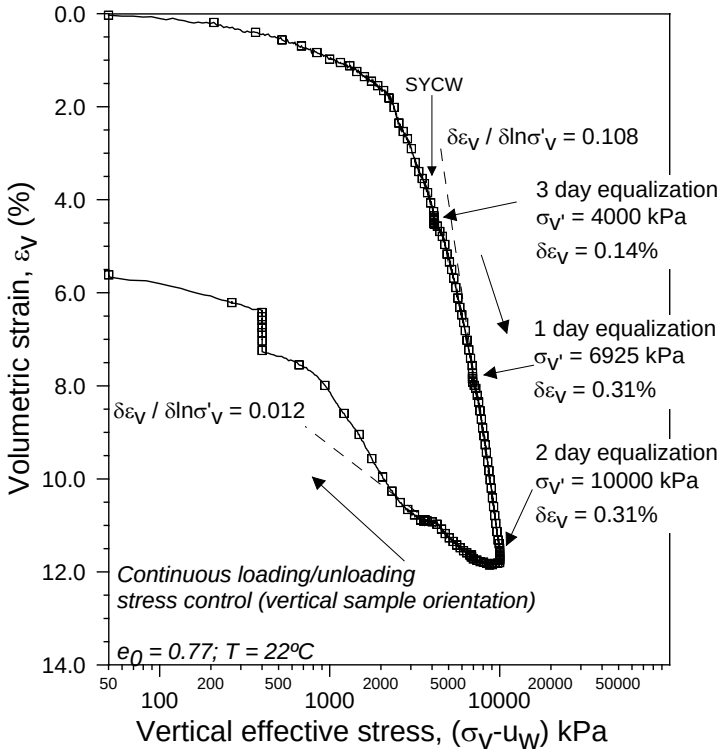

Figure 5.19 Continuous loading/unloading paths at vertical sample orientation (room temperature).

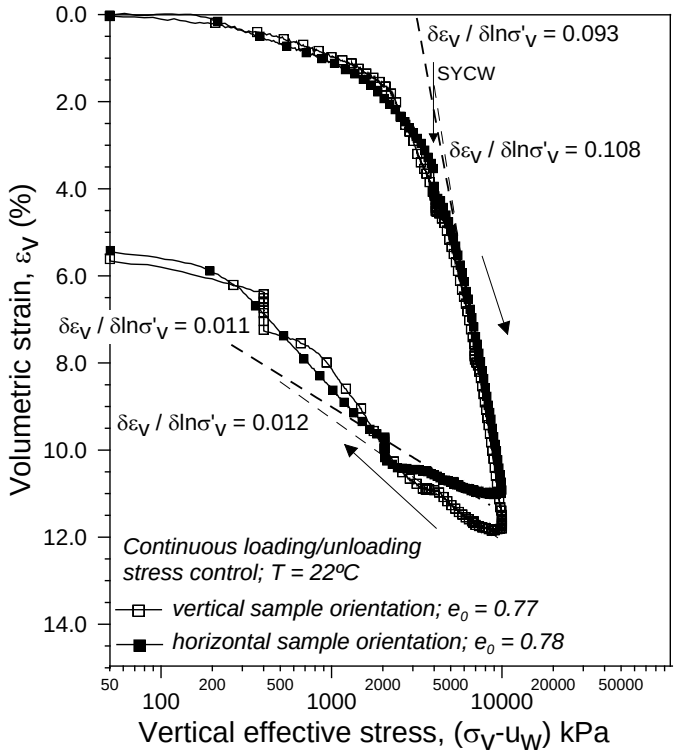

Figure 5.20 Comparisons between vertical and horizontal sample orientations in continuous loading/unloading tests.

Comparison of oedometer tests using continuous and step-loading/unloading techniques are shown in Figure 5.21. For a vertical effective stress of 10 MPa, the volumetric strains attained are similar with both techniques and for both sample orientations. Slightly larger

compressibility parameters are obtained on virgin loading with the continuous loading system. In addition, slightly larger values of post-yield compressibility parameter are obtained on the vertically oriented sample.

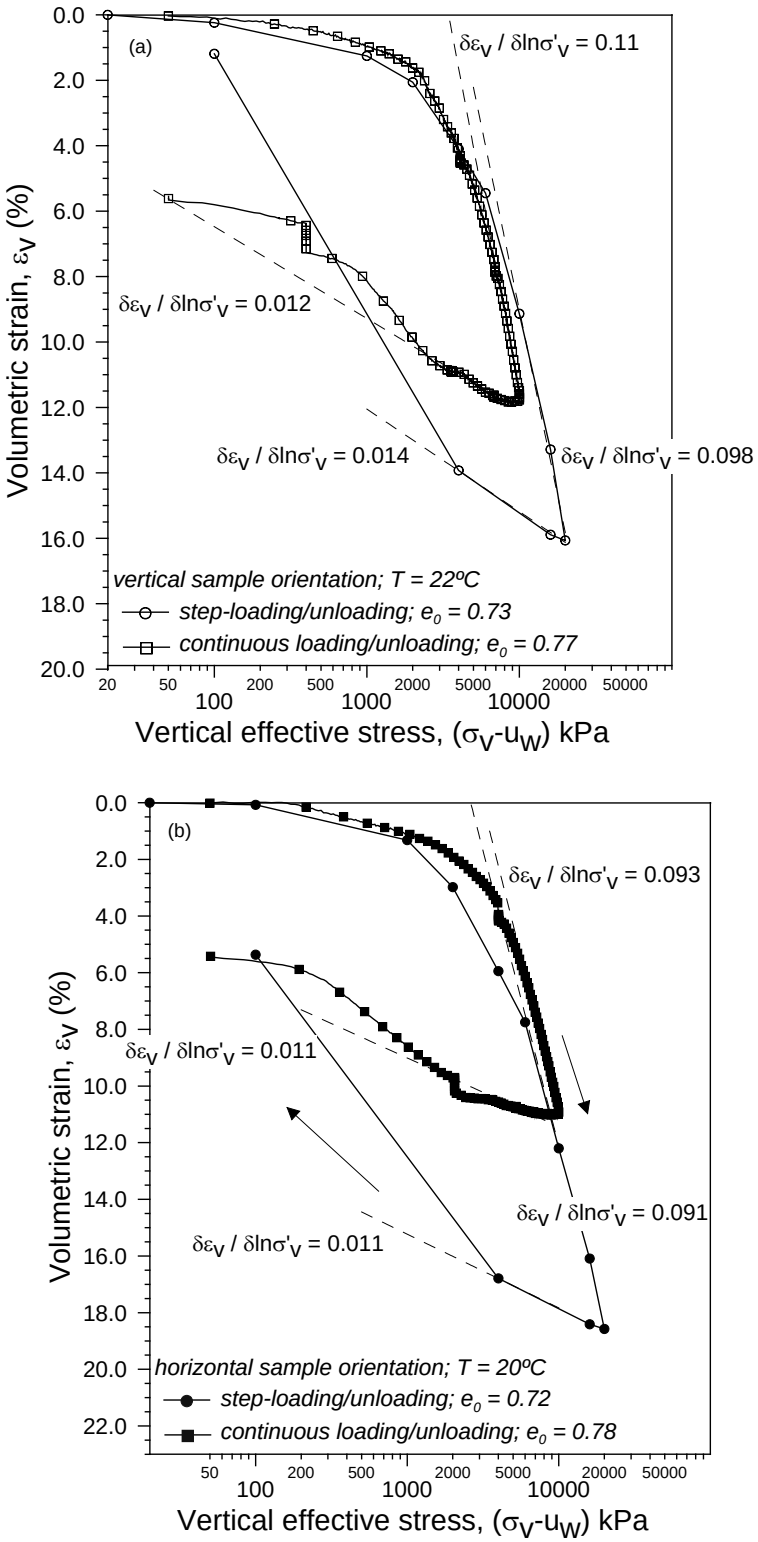

Figure 5.21 Comparisons between step-loading/unloading and continuous loading/unloading tests: (a) vertical sample and (b) horizontal sample orientation.

Continuous loading/unloading results at 80ºC for vertical sample orientation in terms of the variation of volumetric strain with vertical effective stress are shown in Figure 5.22. During temperature increase (26 to 80ºC) and after performing the respective thermal correction (see Appendix B), a soil thermal induced compression of 0.32% is detected. Likewise, Figure 5.23 shows the continuous loading/unloading results at 80ºC for horizontal sample orientation. In this case, an equivalent thermal induced compression of 0.34% is obtained. Comparisons between vertical and horizontal sample orientations are shown in Figure 5.24. This last figure also indicates temperatures effects on the compressibility parameter for both loading (post-yield) and unloading (first unloading stage) conditions at vertical and horizontal sample orientations. Soil volume change responses (thermal induced contraction) on drained heating are shown in Figure 5.25 for both sample orientations.

Comparison of oedometer tests using continuous loading/unloading at different temperatures (20ºC and 80ºC) are shown in Figure 5.26. As observed, no important temperature effects on post and pre-yield compressibility values are obtained.

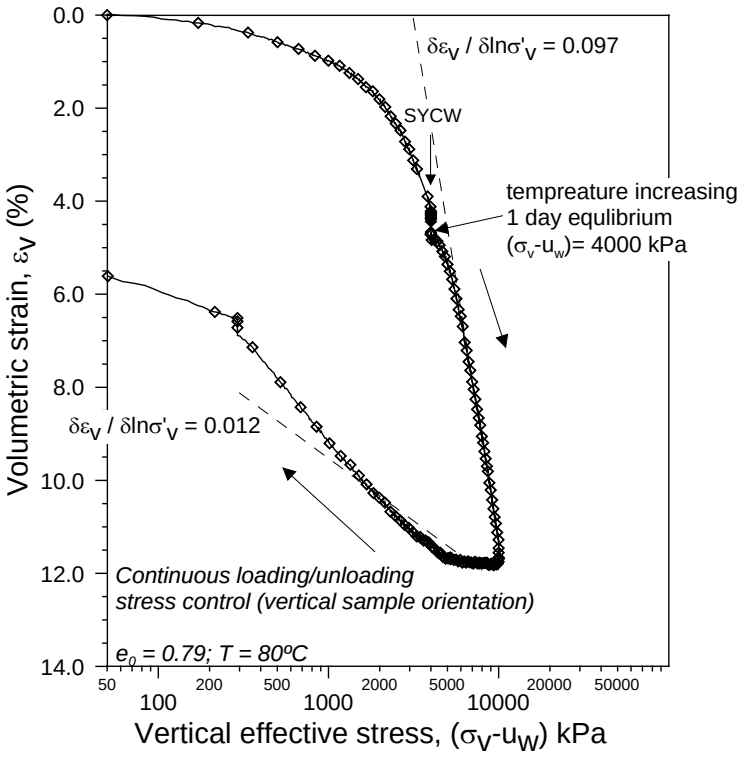

Figure 5.22 Continuous loading/unloading paths on vertical sample orientation at 80ºC.

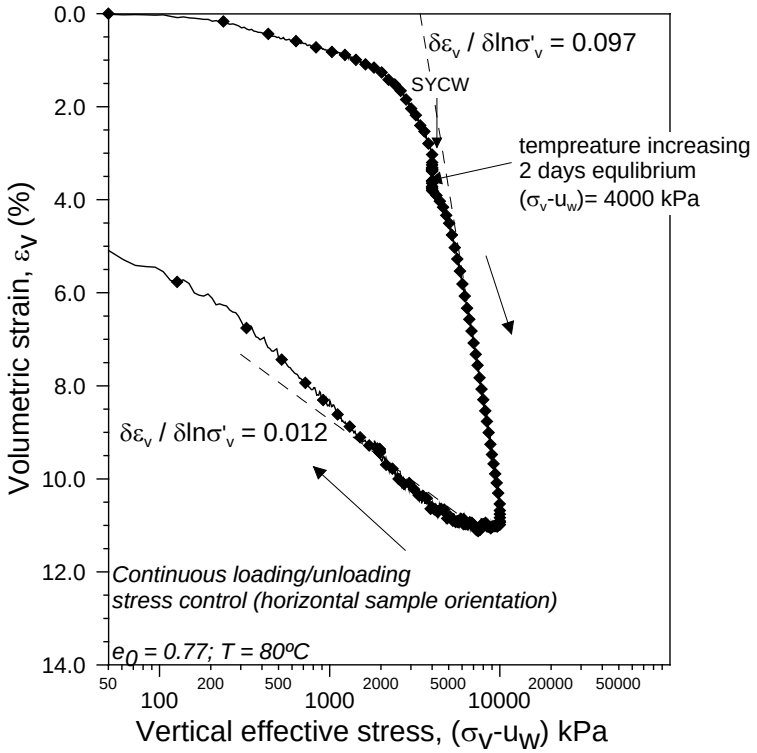

Figure 5.23 Continuous loading/unloading paths on horizontal sample orientation at 80ºC.

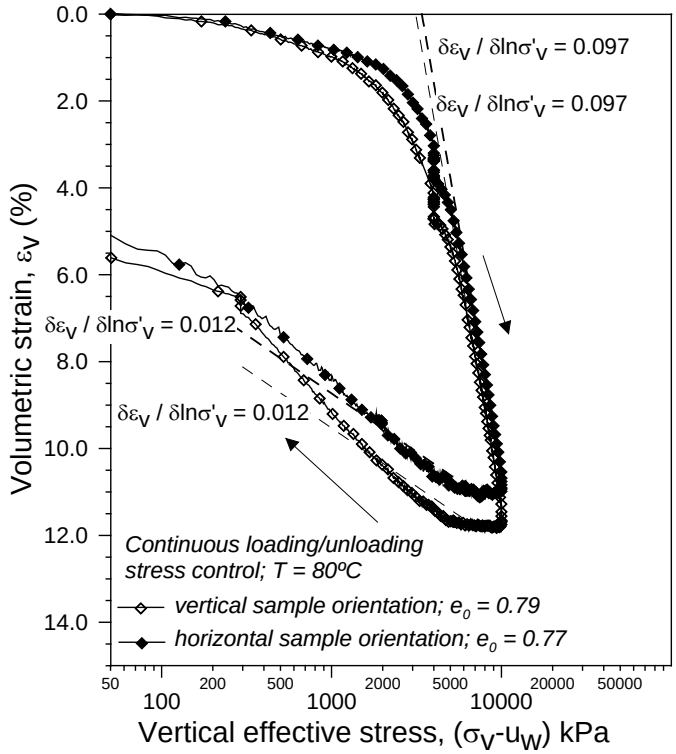

Figure 5.24 Comparisons between vertical and horizontal sample orientations in continuous loading/unloading tests at 80ºC.

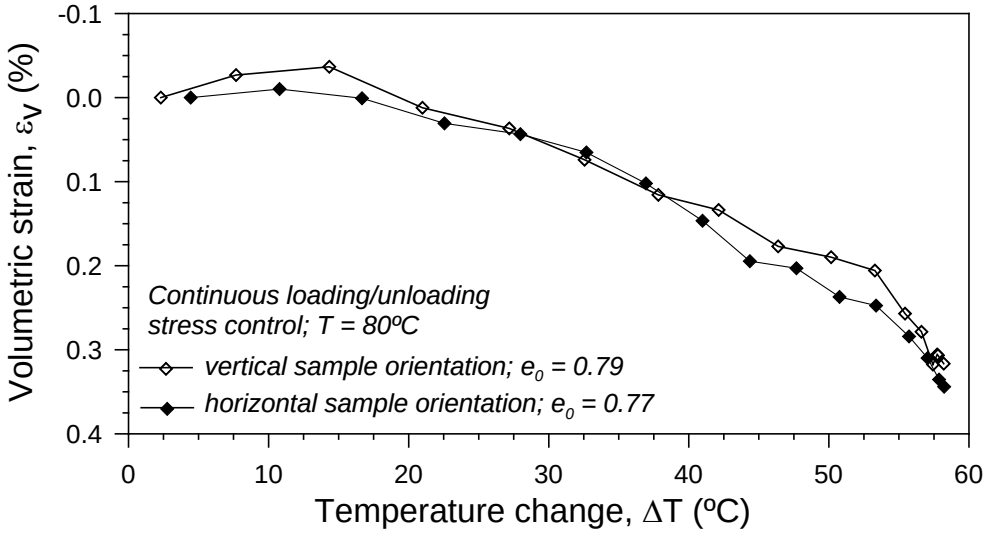

Figure 5.25 Volume change response during drained heating on vertical and horizontal sample orientations.

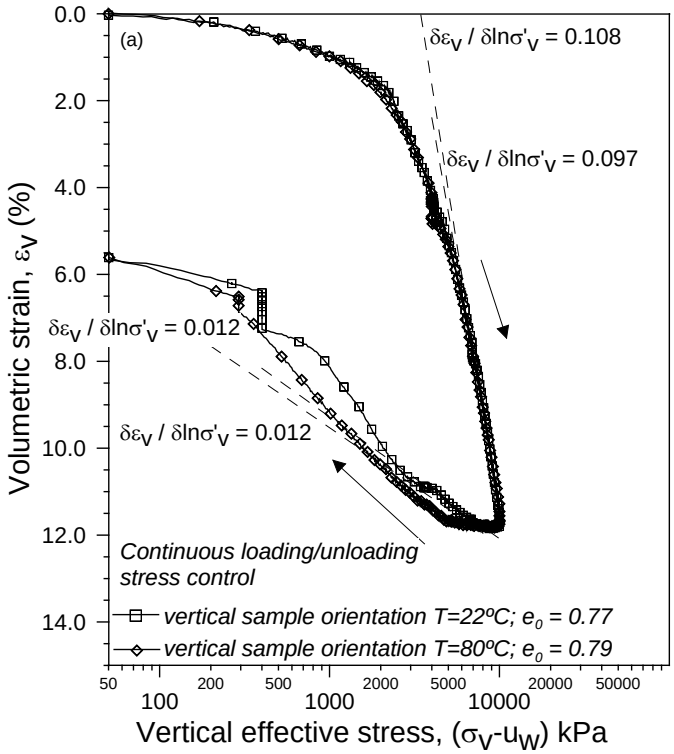

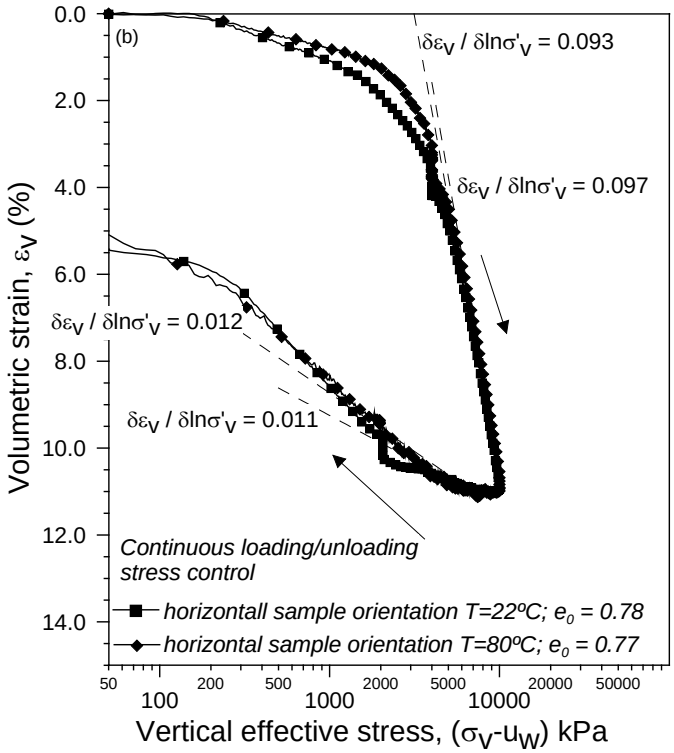

Figure 5.26 Comparisons between continuous loading/unloading tests at 22ºC and 80ºC: (a) vertical sample and (b) horizontal sample orientation.

Figure 5.27 presents the cumulative work input per unit soil volume versus the logarithm of net/effective stress according to Eq. 5.6. Yield stresses are also indicated in this figure for oedometer results of step-loading/unloading (vertical and horizontal orientations) and continuous loading/unloading (vertical and horizontal orientations) at two temperatures (T=20 and 80ºC).

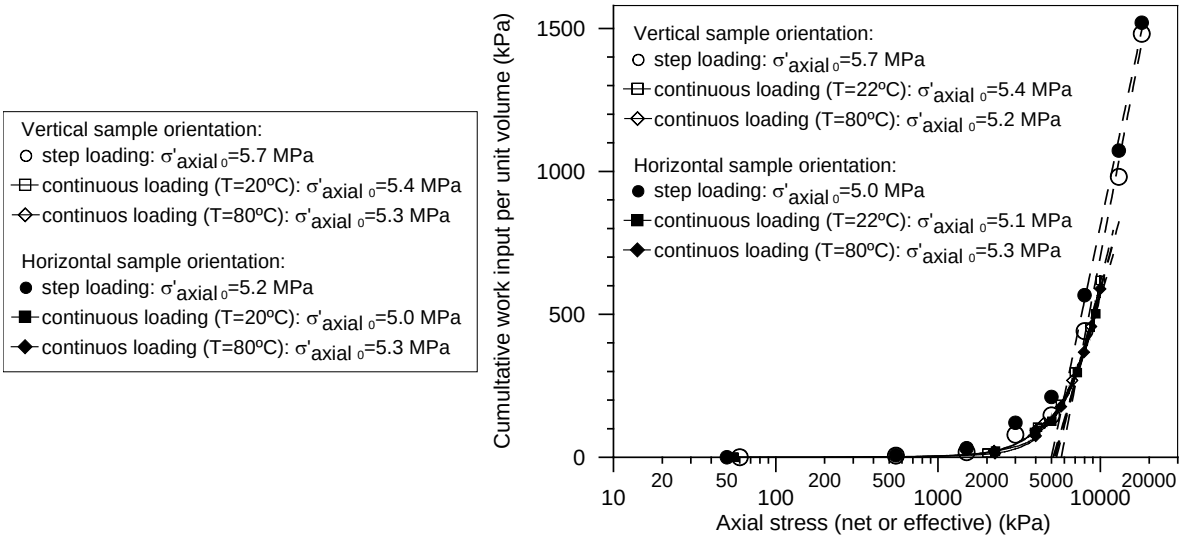

Figure 5.27 Cumulative work input per unit soil volume versus logarithm of the net(total)/effective stress for the whole oedometer program.

In addition, Table 5.6 summarises yield stresses, post-yield compressibility parameters on loading and pre-yield compressibility results (on the first unloading stage) of the different oedometer tests performed: step-loading/unloading (vertical and horizontal orientations) and continuous loading/unloading (vertical and horizontal orientations) at two different temperatures.

Table 5.6 Summary of results of the different oedometer tests performed: step-loading/unloading (vertical and horizontal orientations) at room temperature and loading/unloading (vertical and horizontal orientations) at two temperatures (20 and 80ºC).

Temperature (ºC)	Type of loading/unloadin	Sample orientation	e_0	σ'_{v0} (MPa)	σ'_{h0} (MPa)	$\delta\varepsilon_v/\delta\ln\sigma'_v$ loading	$\delta\varepsilon_v/\delta\ln\sigma'_v$ unloading
20	step	vertical	0.73	5.4-5.7	-	0.098	0.014
		horizontal	0.72	-	5.0	0.091	0.011
20	cont.	vertical	0.77	5.4	-	0.108	0.012
		horizontal	0.78	-	5.2	0.093	0.011
80	cont.	vertical	0.79	5.3	-	0.097	0.012
		horizontal	0.77	-	5.3	0.097	0.012

5.6 THERMO-HYDRAULIC HEATING CELL RESULTS

5.6.1 Hydration phase

As mentioned in the previous chapter (section 4.9.5), the hydration phase was divided into two stages. In first stage, backpressure was increased in steps from 0.5 to 1 MPa during 14 days with the upper valve open under atmospheric conditions. Figure 5.28-a and 5.28-b show the time evolution of temperature and pore water pressures during this initial hydration stage, respectively.

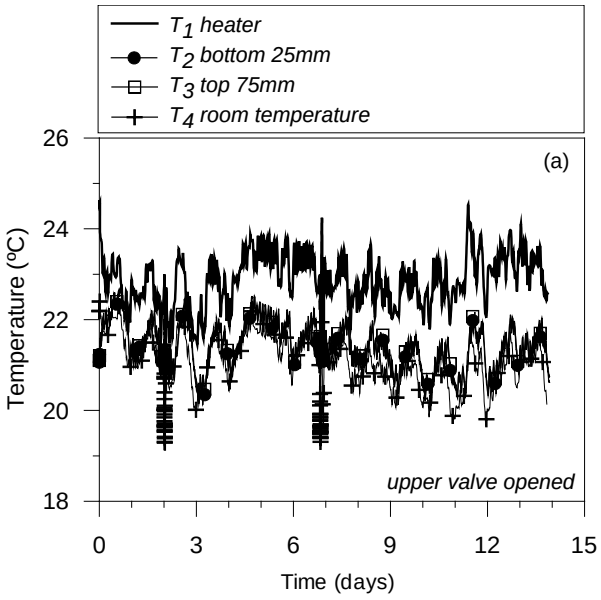

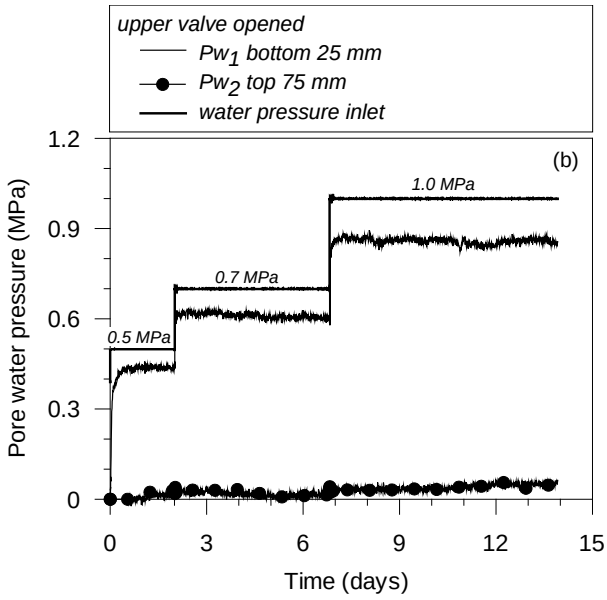

Figure 5.28 Hydration phase with upper valve open. (a) Time evolution of temperature. (b) Time evolution of pore water pressures at different locations.

Once this stage was completed, the saturated water permeability was measured under steady-state conditions. A value of 6.4×10^{-12} m/s was obtained, which is in agreement with the vertical permeability (bedding planes are perpendicular to the direction of axial symmetry) values reported in section 5.3.1. Figure 5.29 presents the time evolution of water inlet and outlet volumes under steady-state conditions and during the application of 1 MPa backpressure (at the bottom boundary).

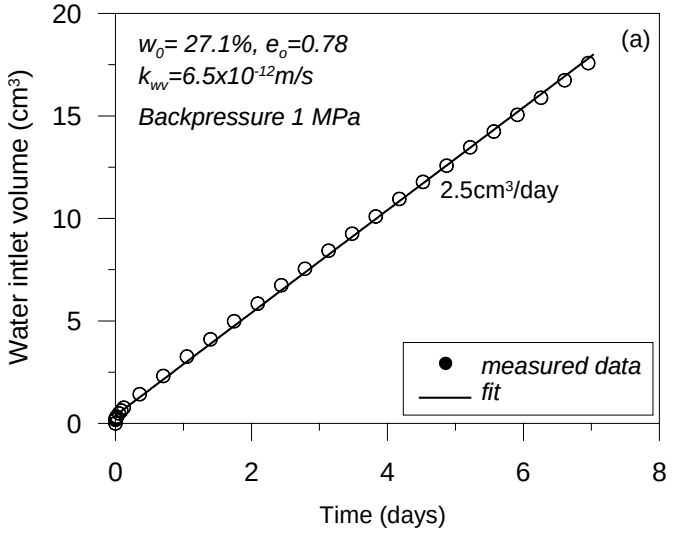

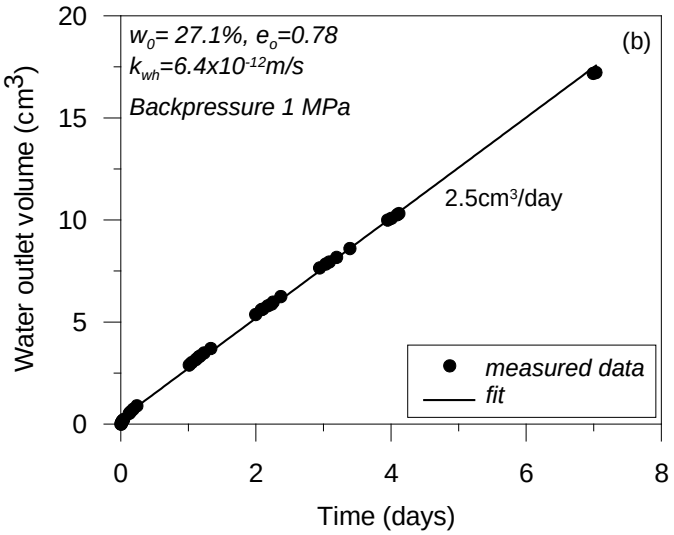

Figure 5.29 Time evolution of (a) water inlet and (b) outlet volumes under steady-state conditions (u_w = 1MPa at the bottom).

To verify the response of the pore pressure transducers and eliminate possible occluded air in the porous disc-soil contact, in a second stage the upper valve was closed and a period of 10 days of pore pressure equalisation was allowed. After this equalisation period, backpressure was increased up to 1.2 MPa for 13 additional days. The time evolution of temperature and pore water pressures are plotted in Figures 5.30-a and 5.30-b.

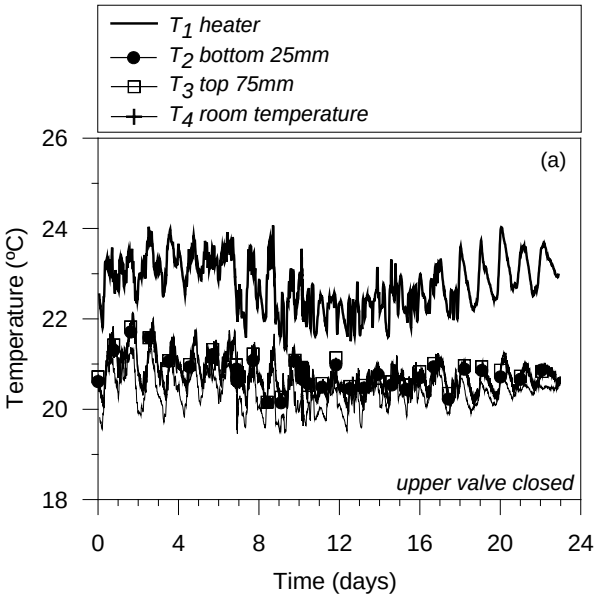

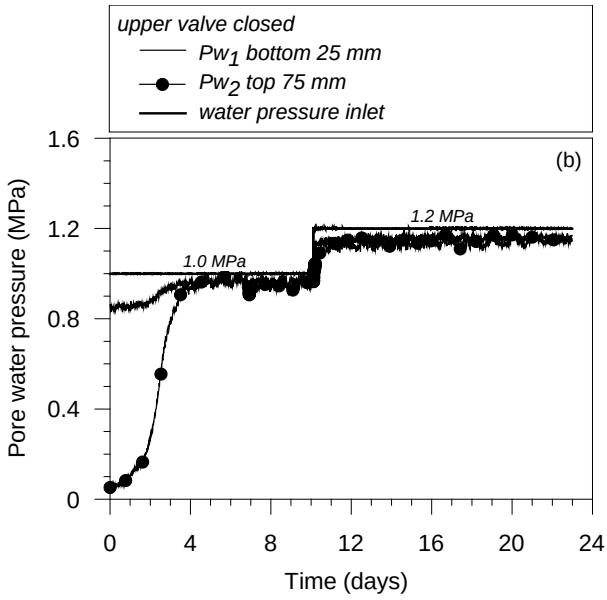

Figure 5.30 Hydration phase-upper valve closed. (a) Time evolution of temperature. (b) Time evolution of pore water pressures at different locations.

5.6.2 Heating and cooling phases

Figure 5.31-a shows the time evolution of temperature at different locations during the first heating and cooling phases, whereas Figure 5.31-b presents the time evolution of the pore water pressure during this thermal cycle. During the heating cycle the upper valve was maintained closed and the lower boundary at a constant backpressure of 1.2 MPa (1.17 MPa measured in the pore pressure transducers).

The maximum temperature reached in the heater was 36 ºC (Fig. 5.30-a). The heater failed at this maximum temperature (dilation of the heater casing occurred and water leakage affected the electrical connections).

The maximum pressure attained was 1.24 MPa for both pore water transducers (Pw_1 and Pw_2) during quasi-undrained heating. The faster dissipation of pore water pressure in Pw_1 is due to the proximity to the bottom draining boundary (25 mm to the backpressure boundary). During the quasi-undrained cooling and returning to the initial temperature, the pore water pressure Pw_1 decreased up to 1.14 MPa before tending to the initial value (1.17 MPa).

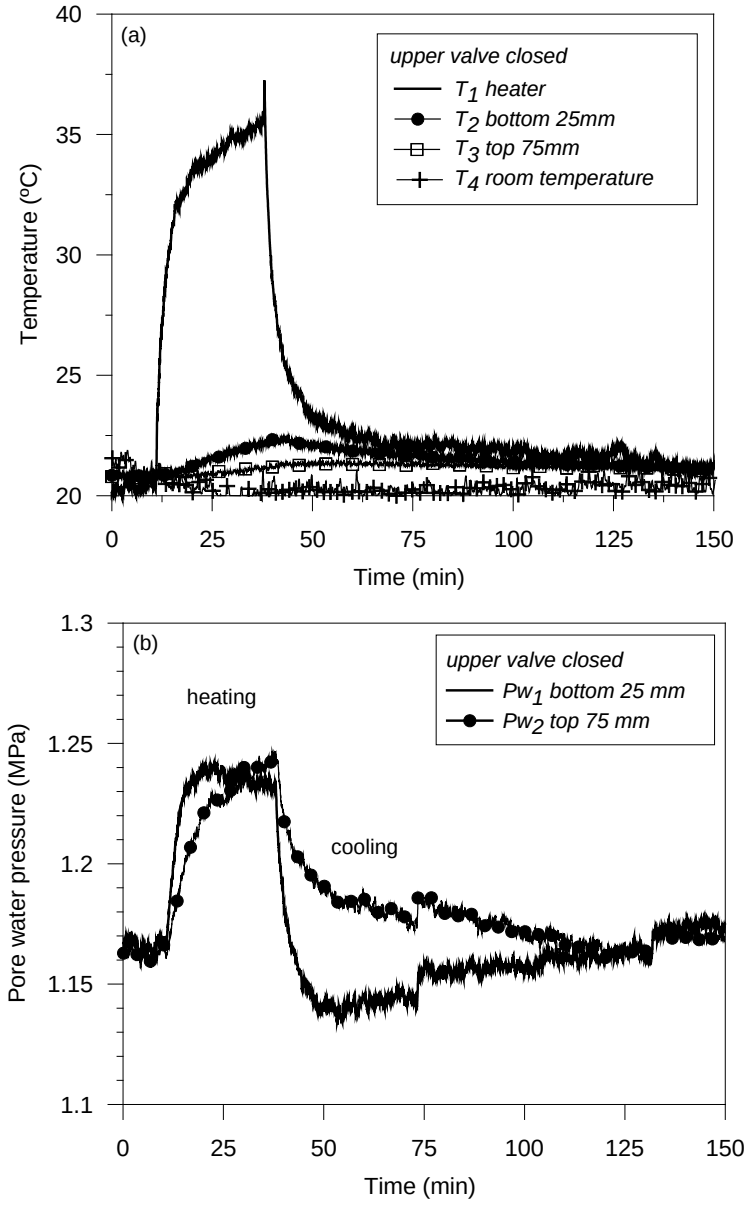

Figure 5.31 Heating and cooling phases. (a) Time evolution of temperature at different locations. (b) Time evolution of pore water pressures at different locations (u_w = 1.2 MPa at the bottom boundary).

In figure 5.32, the time evolution of quasi-undrained pressurisation coefficient during heating (a) and cooling phases (b) is presented. The maximum values reached of $\Delta u/\Delta T$ were 0.613 and 1.0 MPa.C^{o-1} corresponding to heating phase measurements at bottom and top, respectively; whereas for the cooling one, a $\Delta u/\Delta T$ value of 0.863 MPa.C^{o-1} was found.

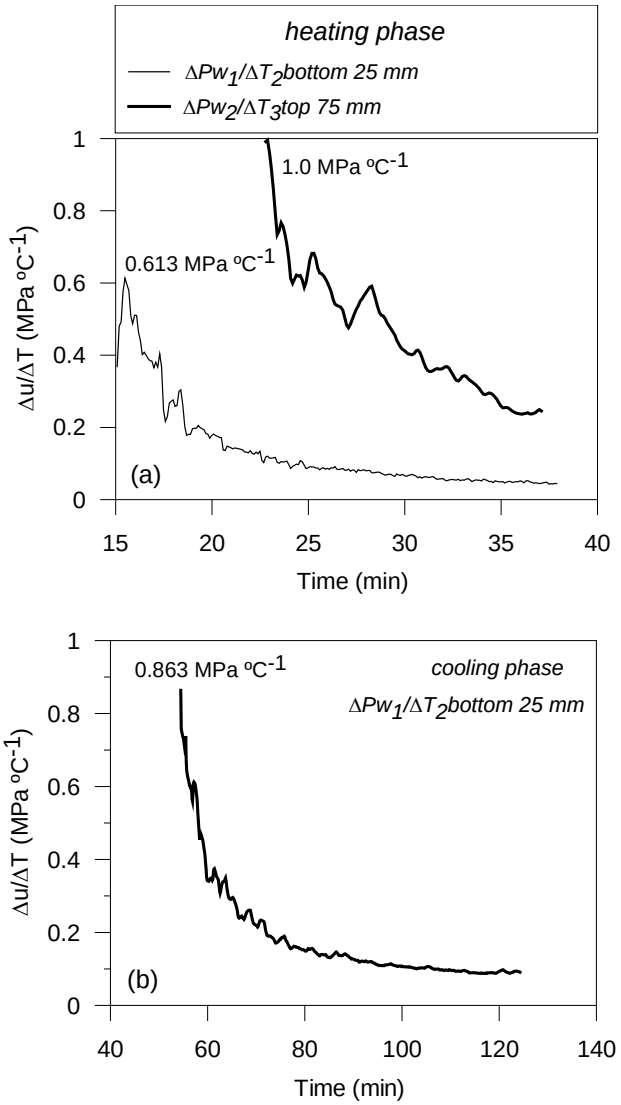

Figure 5.32 Time evolution of quasi-undrained pressurisation coefficient during heating (a) and cooling phases (b).

5.7 MICROSTRUCTURAL CHANGES INDUCED ON THE DIFFERENT LOADING PATHS FOLLOWED

Figure 5.33 shows a comparison of PSD results between the undisturbed material and two post-mortem samples consolidated up to vertical effective stress of 20 MPa, in which the sample extraction process has been performed under different hydraulic conditions. In one case, the water inlet valve was maintained open during unloading, whereas in the second case, the valve was kept closed (no water inlet was allowed on stress relief).

As observed in the figure, the applied load induces an important reduction of both micro and macroporosity when the valve is kept closed. Nevertheless, when water inlet into the sample is allowed, the material swells significantly (up to final void ratio of 0.76) and the macroporosity is recovered.

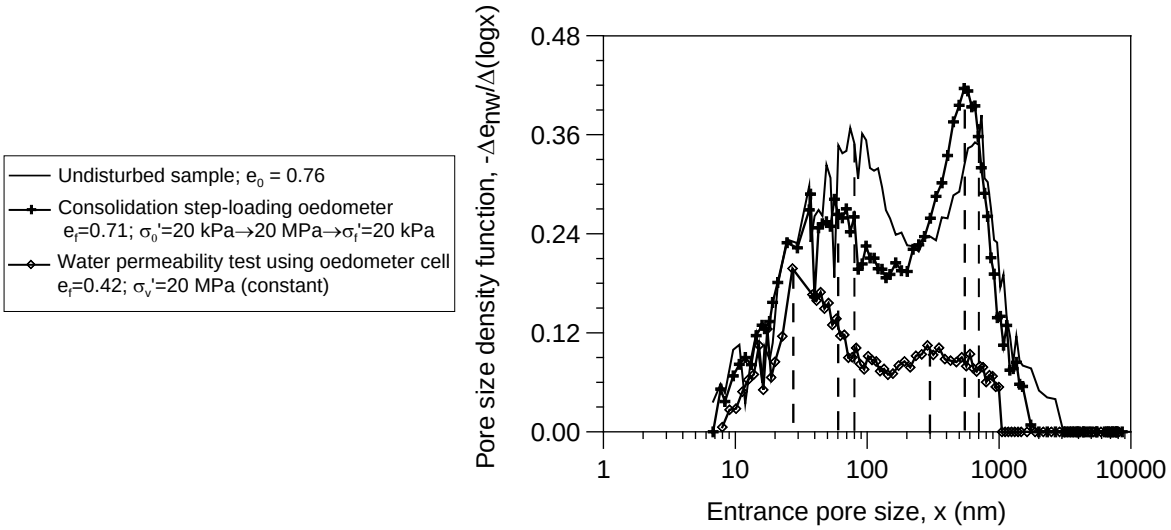

Figure 5.33 MIP comparisons between two samples loaded to an vertical effective stress of 20 MPa and then extracted following different procedures (with water inlet or with valve closed).

To have representative samples of the final loading stage, the water inlet valve during sample extraction processes should remained closed. Figure 5.34 presents the comparison between MIP results of the undisturbed material and three post-mortem samples consolidated to different effective vertical stresses (4, 10 and 20 MPa). In relation to loading effects, microstructural results are consistent showing a reduction of the macroporosity on stress increase up to a vertical effective stress of 10 MPa. On further loading the macroporosity is still reduced with some contribution of the microporosity (the microporosity begins to be reduced from a vertical effective stress of 10 MPa).

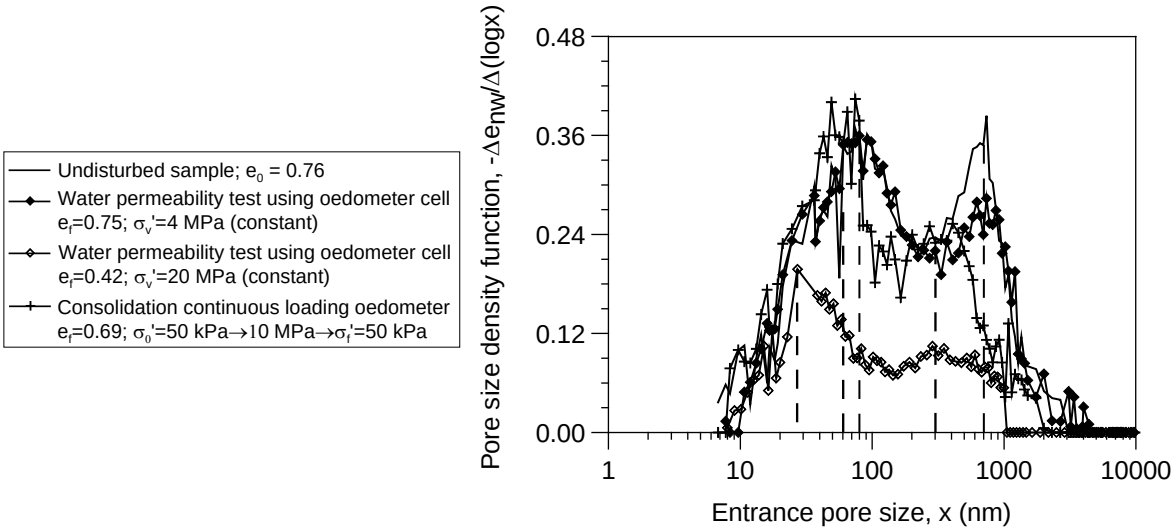

Figure 5.34 MIP comparisons of samples consolidated to different effective vertical stresses.

5.8 COMPARISONS BETWEEN GEOTECHNICAL PROPERTIES OBTAINED IN THIS RESEARCH AND PREVIOUS REPORTS

Based on the information presented in chapter 3, a brief comparison of results obtained in this investigation and those from previous reports is presented, basically concentrating on the properties at equivalent depth. This comparison complements the state of the art knowledge on Ypresian clay.

The main issues, which were compared, were the following properties:

- Basic geotechnical properties
- Clay mineralogy composition
- Microporosity
- Water permeability

Table 5.7 summarises the results of the basic geotechnical characterisation performed in this research (Kallo samples) and the one undertaken on Doel samples. As reflected by the results, the index properties of both materials are quite similar, being important to note that Kallo and Doel sample retrieval sites are within the same depositional area (area II, see section 2.2.2). Differences between both samples are found in the gravimetric water content, which is higher in Doel samples, and the in consistency limits values, which are considerably higher in Kallo samples. This last issue is associated with the high smectite content presented in Kallo samples (≈ 64%) in relation to the reported content in Doel samples (≈ 45%).

Table 5.7 Basic geotechnical properties. Comparison between Kallo (this research) and Doel samples at the same depth (around 370 m).

Soil properties	Kallo samples (present research) Depth: 369.76-370.56 m	Doel samples Depth: 369.79-371.79 m
Density, ρ	1.97 to 2.02 Mg/m^3	1.87 to 1.98 Mg/m^3
Dry density, ρ_d	1.55 to 1.60 Mg/m^3	1.54 Mg/m^3
Gravimetric water content, w	26 to 26.6%	27.9 to 29.3 %
Density of soil solids, ρ_s	2.76 Mg/m^3	2.70 to 2.75 Mg/m^3
Void ratio, e	0.72 to 0.78	0.76 to 0.86
Porosity, n	0.418 to 0.438	0.431 to 0.463
Degree of saturation, Sr	94 to 98 %	93.3 to 100 %
Liquid limit, w_L	142 to 158 %	96.3 %
Plasticity index, PI	116 to 133%	66.5 %

Regarding to the microporosity of the materials, the double porosity network observed in Kallo samples and presented in section 5.1 was also found in Doel samples, in which the characteristic pore sizes are smaller and around 10 and 70 nm. Doel samples were

analysed by INISMa using a mercury intrusion porosimeter 'AutoPore III' from *Micromeritics* (see section 2.3.3, chapter 2).

Finally, pulse injection experiments (vertical water permeability) and in situ pressure pulse tests (that can be approximated to horizontal water permeability) performed in Doel samples were compared to the water permeability results obtained in the present research. Table 5.7 present a comparison between both results. A quite good agreement is obtained in the vertical water permeability, and horizontal values are consistently higher compared to the vertical ones.

Table 5.8 Comparison of water permeability results between Kallo (present research) and Doel samples at the same depth (around 370 m).

Soil properties	Kallo samples (present research) Depth: 369.76-370.56 m	Doel samples Depth: 369.79-371.79 m
Vertical water permeability (T=20ºC), $k_{w\,v}$	6.6 x 10^{-12} m/s	4.6 x 10^{-12} m/s
Horizontal water permeability (T=20ºC), $k_{w\,h}$	7.9 x 10^{-12} m/s	(100 to 130) x 10^{-12} m/s

CHAPTER 6

SUMMARY, CONCLUSIONS AND FUTURE RESEARCH WORK

6.1 SUMMARY AND CONCLUSIONS

This research has been developed in the framework of the coupled thermo-hydro-mechanical characterisation of Ypresian clay (retrieved from the Kallo area) as an alternative host formation for deep disposal of high-level and/or long-lived radioactive waste in Belgium. In this section, a summary with main conclusions drawn from the experimental program is presented.

6.1.1 Initial geotechnical characterisation of the material

An initial geotechnical characterisation program was performed on samples taken from Kallo borehole extracted at a depth around 370 m (core identification: 83) by laboratory classification test (density, degree of saturation, water content and consistency limits), initial total suction (chilled-mirror dew-point psychrometer), X-ray diffraction and mercury intrusion porosimetry (pore size distribution curve of the intact material). A relevant issue of the classification program is the high plasticity of the material (liquid limit between 142 and 158% and plasticity index 116-133%), as a consequence of the high smectite content present in Kallo samples (around 64%). With respect to the initial total suction (2 MPa) induced on retrieval (undrained stress relief), it is lower than that measured on Boom clay, despite being Ypresian clay retrieved at a larger depth. This is a consequence of the water retention properties of Ypresian clay described later. Qualitative mineralogy characterisation performed on air-dried randomly oriented powdered sample allowed detecting the presence of illite and smectite (not fully identified) in the clay fraction, and a clear dominance of quartz in the non-clay fraction. Further DRXs with oriented aggregates are required to discriminate clayey phases. In relation to microporosity, the material presents two dominant pore modes, one at 700 nm and another in 80 nm. This is not usual at all when dealing with deep depositional clayey formations (Boom clay displays a mono-modal pore size distribution). This larger porosity induces some early desaturation of the material when total suction increases above 2 MPa on stress relief (the degree of saturation of the retrieved material is around 94 to 98%, displaying a total suction of 2 MPa).

6.1.2 General hydraulic and mechanical characterisation

Drying and wetting branches of the water retention curve were determined by chilled-mirror dew-point psychrometer readings. As previously indicated, a possible consequence related to the material double porosity is an early desaturation process at total suctions above 2 MPa. The drying branch of the water retention curve estimated from backanalysis of mercury intrusion results confirms this lower air-entry value (around 0.4 MPa), which is associated with the larger macropores.

Regarding the material low-strain stiffness properties, shear moduli values G_0 by resonant column test were found slightly lower in horizontal direction (between 90 and 120 MPa) compared to the vertical orientation (between 130 and 170 MPa). Low-strain shear

modulus results obtained with bender elements on unloaded samples are consistent with those obtained from resonant column tests. Nevertheless, in this case G_0 values are slightly higher in the horizontal direction showing an opposed trend compared to resonant column results. Despite these results, it appears that no important anisotropy effects are detected on regard low-strain shear stiffness.

6.1.3 Hydro-mechanical characterization under oedometer conditions

Hydro-mechanical oedometer tests under saturated conditions at different temperatures (22 and 80 ºC) and two different orientations (vertical and horizontal) using step loading/unloading and continuous loading/unloading techniques were performed, displaying both techniques similar results.

Pre-yield (first loading and unloading) and post-yield (virgin loading) behaviour could be clearly identified. Care was taken in following a systematic procedure to identify the yield stress based on the cumulative volumetric work input per unit volume. Yield stresses of approximately 5.4 - 5.7 MPa and 5.0 - 5.1 MPa were identified for the step loading and continuous loading compression curves at 22 ºC on vertical and horizontal sample orientations, respectively. Based on the same procedure, a yield stress between 5.2 - 5.3 MPa was determined for both orientations and at 80 ºC, indicating that temperature does not affect this value (at least within of the temperature range considered).

Systematically, slightly larger post-yield compressibility parameters ($\delta\varepsilon_v/\delta\ln\sigma'_v$) were obtained on vertical oriented samples (between 0.098 and 0.108) compared to horizontal compressibility within the range (0.091 to 0.093). Temperature did not affect the post-yield compressibility (around 0.097 for both orientations). Pre-yield compressibility values (for the first unloading stage) were within the range 0.011 to 0.014, and neither temperature nor orientation appeared to affect it.

Drained heating at a constant vertical effective stress of 4 MPa induced thermal contraction (around 0.33%), which was detected after applying the equipment correction during the heating path.

Time evolutions of deformation along different step loading stages were back-analysed to estimate different consolidation parameters. This back-analysis allowed determining the consistent variation of water permeability with void ratio for both sample orientations.

6.1.4 Thermo-hydraulic characterisation

The thermo-hydraulic characterisation of the material included the determination of the water permeability at different temperatures, orientations and void ratios. Water permeability values at different temperatures (22, 40, 60 and 80ºC) and under constant volume conditions were performed presenting a slight anisotropy ($k_{wh} > k_{wv}$) and a thermal dependence higher than the water viscosity prediction (β_T between 0.035 and 0.039ºC^{-1}, slightly larger than the prediction of 0.030ºC^{-1}). At room temperature and approximately at in situ void ratio the vertical water permeability (flow perpendicular to bedding planes) was around 1.1 to 6.6x10^{-12} m/s, whereas the horizontal was between 6.1 and 7.9x10^{-12} m/s. At 80ºC and approximately the same in situ void ratio, the vertical one raised up to 3.5x10^{-12} – 2.0x10^{-11} m/s.

To analyse the material double porosity features and temperature cycling on water permeability, controlled-gradient oedometer tests at constant vertical effective stresses of 4 MPa (vertical sample orientation) and 20 MPa (horizontal sample orientation) were performed. From these preliminary results it can be suggested that the material water permeability properties are not affected by progressive heating/ cooling cycles, but further tests should be done to confirm this trend.

On the other hand, the heating pulse test equipment was upgraded, which included the development of new acquisition software, the adaptation of new pore water pressure transducers with new connecting systems to the cell wall, and a new controlled-power cartridge heater with inner thermocouple included. All the systems were calibrated within the present research program. Furthermore, preliminary results of one heating/cooling pulse test were presented. The test was interrupted due to heater failure by leakage affecting electrical connections.

6.1.5 Microscopic analysis

Microstructural changes induced by the different stress paths followed were analysed by mercury intrusion porosimetry.

In relation to loading effects, microstructural results consistently showed a reduction of the macroporosity on stress increase up to a vertical effective stress of 10 MPa. On further loading to 20 MPa the macroporosity was still reduced with some contribution of the microporosity (the microporosity begins to be reduced from a vertical effective stress of 10 MPa). In addition, the unloading tests that were carried out with water inlet allowed, showed that the macroporosity was recovered on stress relief. This is consistent with macroscopic compressibility results, in which on drained unloading the initial void ratio is nearly recovered. On regarding thermal effects (and within the range considered in the tests), no important consequences were induced in terms of microstructural changes.

6.2 FUTURE RESEARCH WORKS

The main pending work dealing with this THM research is carrying out the heating pulse test program in the already updated constant volume cell and the interpretation of the results based on coupled numerical simulations. The interpretation will allow determining parameters (thermal conductivity, water permeability, linear elastic parameters) through back-analysis of test results, as well as comparing the obtained parameters with those determined in the present study. On the other hand, the new tests and simulations will benefit through the extensive THM characterisation programme already performed on intact Ypresian and presented in this document. In addition, a blind test prediction will be useful to verify the calibration of the results.

On regarding water permeability, further tests will help analysing thermal cycling and loading effects changing the double porosity features on this hydraulic parameter. These studies should be complemented with microstructural analyses using mercury intrusion porosimetry.

REFERENCES

Arroyo, M., Pineda, J. and Romero, E (2010). Shear wave measurements using bender elements in argillaceous rocks. Geotechnical Testing journal, vol. 33, núm. 6, p. 1-11.

ASTM (2011). Annual book of ASTM Standards, Vol. 04.08- 04.09, Philadelphia.

Cardoso, R., Romero, E., Lima, A. and Ferrari A. (2007). A comparative study of soil suction measurement using two different high-range psy-chrometers. Proc. 2nd Int. Conf. Mechanics of Unsaturated Soils. Weimar, T. Schanz (ed.). Springer-Verlag, Berlin, 79-93.

Das, B.M. (1983). Advanced soil mechanics. Hemisphere Publishing Corporation. Washington.

Decagon Devices, Inc. (2003). WP4Water Dewpoint Potentiometer. Operator's Manual, Version 2.2. Decagon Devices, Inc., Pullman (www.decagon.com).

Diamond, S. (1970). Pore size distributions in clays. Clays and Clay Minerals, 18: 7-23.

GEO-data (2008). Kallo 1 well, Belgium, technical 1:500 Log.

Hoffmann, C. (2005). Caracterización hidromecánica de mezclas de pellets de bentonita. estudio experimental y constitutivo. PhD Thesis. Universitat Politècnica de Catalunya, Spain.

Houlsby, G.T. 1997. The work input to an unsaturated granular material. Géotechnique, 47(1): 193-196.

IAEA (2001). The use of scientific and technical results from underground research laboratory investigations for the geological disposal of radioactive waste. IAEA-TECDOC-1243.

INISMa (1998). Technical report n°74.252. Mons, Belgium.

James Instruments, Inc. (2011). V-Meter-II ultrasonic pulse device. Operator's Manual.

KULeuven (2011). Lab for Applied Geology & Mineralogy, technical report. Belgium.

LGTH (1996). Inventarisatie van de kennis van de Ieperiaanklei in functie van onderzoek naar diepe berging van hoogradioactief afval. TGO 94/30 technical report.

Lima, A., Romero, E., Gens, A. and Li, X.L. (2010). Hydro-mechanical behaviour of boom clay under non-isothermal conditions. Clays in natural & engineered barriers for radioactive waste confinement 4th international meeting. Nantes, France, 781-782.

Lima (2011). Thermo-hydro-mechanical behaviour of two deep Belgium clay formations: Boom and Ypresian clays. PhD Thesis. Universitat Politècnica de Catalunya, Spain (in preparation).

Mesri, G. (1973). Coefficient of secondary compression. J. Soil Mech. Found. Div., ASCE, 99(1): 123-237.

Mitchell, J.K. and Soga, K. (2005). Fundamentals of soil behavior. John Wiley & Sons, Inc., Hoboken, New Jersey, 3rd ed.

Muñoz, (2006). Thermo-hydro-mechanical analysis of soft rock: application to a large scale heating test and large scale ventilation test. PhD Thesis. Universitat Politècnica de Catalunya, Spain.

Pineda, J.A, Lima, A. and Romero, E. (2008). Influence of hydraulic paths on the low-strain shear modulus of a stiff clay. Proc. First European Conference on Unsaturated Soils: Advances in Geo-Engineering, July 2-4, 2008, Durham, UK. D. Toll, C. Augarde, D. Gallipoli & S. Wheeler (eds.). Taylor & Francis Group, London: 519-523.

Pineda, J.A., Mitaritonna, G., Romero, E. and Arroyo, M. (2010). Effects of hydraulic cycling on the stiffness response of a rigid clay. Unsaturated Soils-Alonso & Gens (eds). Taylor & Francis Group, London: 1465–1470.

Romero, E. (1999). Characterisation and thermo-hydro-mechanical behaviour of unsaturated Boom clay: an experimental study. PhD Thesis. Universitat Politècnica de Catalunya, Spain.

Romero, E. and Simms, P.H. (2008). Microstructure investigation in unsaturated soils: A review with special attention to contribution of mercury intrusion porosimetry and environmental scanning electron microscopy. Journal of Geotechnical and Geological Engineering 26(6), 705-727.

Romero, E. (2011). Personal communication. Universitat Politècnica de Catalunya, Spain.

SCK-CEN (2005). Determination of the hydraulic conductivity, ηR and the apparent diffusion coefficient on Ieper Clay and Boom Clay cores from the Doel-1 and Doel-2b drillings. SCK-CEN-R-3589, technical report. Mol, Belgium.

SCK-CEN (2009). Personal communication. Mol, Belgium.

Suriol, J. (1993). Medida de la deformabilidad de suelos mediante el equipo de columna resonante. Revista de Obras Públicas, n 3 (319) 140, pp. 57-66, Madrid.

Van Marcke, P. and Laenen, B. (2005). The Ypresian clays as possible host rock for radioactive waste disposal: an evaluation. ONDRAF/NIRAS technical report, publication NIROND 2005-01.

APPENDIX A

Water retention properties of two deep Tertiary clay formations within the context of radioactive waste disposal

Water retention properties of two deep Tertiary clay formations within the context of radioactive waste disposal

Lima, A.
Department of Geotechnical Engineering and Geosciences, Universitat Politècnica de Catalunya, Barcelona, Spain, analicelima@hotmail.com

Romero, E.
Department of Geotechnical Engineering and Geosciences, Universitat Politècnica de Catalunya, Barcelona, Spain, enrique.romero-morales@upc.edu

Piña, Y.
Department of Geotechnical Engineering and Geosciences, Universitat Politècnica de Catalunya, Barcelona, Spain, p.yessenia@gmail.com

Abstract: Belgium investigates the design for disposal of its 'High-Level Radioactive Waste' in two deep clay formations; the Boom clay at Mol, considered the reference host formation, and Ypresian clay at Kallo as the alternative one. The water retention properties of these deep low-porosity formations have been investigated for two main reasons. High suctions develop as a consequence of sample retrieval (at depths between 223 and 350 m), which affect the hydro-mechanical response of these materials, especially at low stress levels. In addition, water retention properties have also been studied to better assess possible desaturation effects due to venting of the disposal facility galleries. After a description of their main properties at intact state and their microstructural features (pore size distributions), the water retention properties of both clays covering a wide suction range and using different complementary techniques are presented and discussed.

Keywords: deep clay formation; water retention properties; microstructure

1 INTRODUCTION

Belgium investigates the design for disposal of its 'High-Level Radioactive Waste' in two deep clay formations. Boom clay is considered the reference host formation and the objective of an extensive research programme. In order to study this clay, located between 160 and 270 m deep, an Underground Research Laboratory at 230 m depth was constructed near Mol (Belgium). On the other hand, Ypresian clay is the alternative host formation that is beginning to be studied to investigate its thermo-hydro-mechanical properties. Two different sites are being considered as potential deposits: Doel and Kallo (near Antwerp, Belgium), where this clay is located between 300 and 450 m deep.

Particular attention has been focused on the water retention properties of these deep low-porosity formations for two main reasons. On one hand, high suctions develop as a consequence of sample retrieval, which affect the hydro-mechanical response of these materials (important swelling have been observed on liquid contact at low stress levels despite being completely saturated). On the other hand and from an operational viewpoint, water retention properties have also been studied to better assess possible desaturation effects due to venting of the disposal facility galleries.

This paper describes the main properties of Boom and Ypresian clays at intact state and their microstructural features obtained by mercury intrusion porosimetry. These clays display quite contrasting microstructural properties, which have important consequences on their hydraulic properties. Specifically, the paper presents the water retention properties, which were obtained using complementary techniques (vapour equilibrium method, chilled-mirror and transistor psychrometers) and discussed within the light of their different microstructural features.

The paper also discusses the different air-entry values obtained when expressing the retention properties in terms of degree of saturation and water content.

2 TESTED MATERIALS AND EXPERIMENTAL PROGRAMME

2.1 Boom and Ypresian clays

The Boom clay is the youngest sea sediment, which was deposited during the Rupelian stage (Northwest European Tertiary Basin), 36 to 30 million years ago (Horseman *et al*., 1987). Its mineralogy mainly consists of clay minerals (average 55%) dominated by illite (20-30%), kaolinite (20-30%) and smectite (10 %). The non-clayey fraction is dominated by quartz (25 %) and feldspar (Coll, 2005; ONDRAF/NIRAS, 2005).

The Ypresian clay is also constituted by marine sediments deposited during the Ypresian stage (Eocene series, 54 to 49 million years ago) as reported by ONDRAF/NIRAS (2005). It presents a clay fraction of 45%. Smectite is the dominant phase (25%), followed by illite (15%) and a small amount of kaolinite and chlorite. Non-clayey fraction is constituted predominantly by quartz (45%) and feldspar (5%).

The studied block and borehole samples of Boom and Ypresian clays were retrieved at depths of 223 m and 350 m, respectively. The location of the retrieval sites is shown in Figure 1.

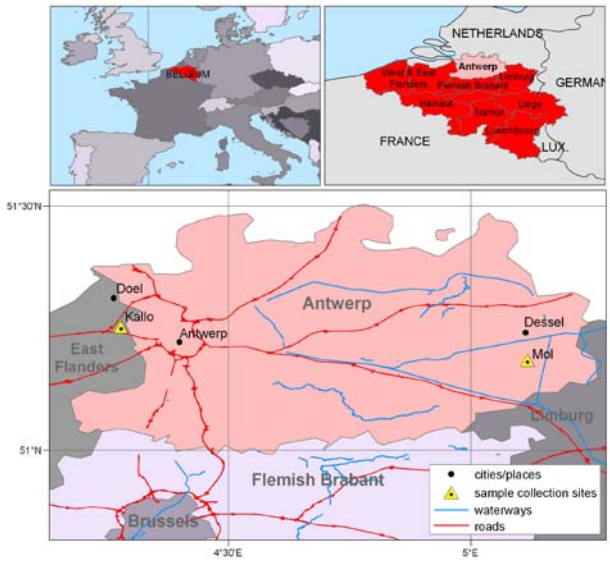

Figure 1. Location of sample retrieval sites.

Table 1 summarises the basic characterisation and the main volumetric and gravimetric properties of the intact materials, which are lightly overconsolidated and saturated stiff clays. As observed in the table, Ypresian clay displays a larger liquid limit, which is consistent with the important smectite content. Another important aspect to highlight, which can be also associated with this higher smectite content, is the larger void ratio of Ypresian clay, despite being formed at a larger depth.

Table 1 also indicates an important initial total suction for the retrieved quasi-saturated soils. In the case of Boom clay, the *in situ* condition at the sampling depth is characterised by a vertical total stress σ_{vi}=4.50 MPa and a water pressure u_{wi}=2.25 MPa (vertical effective stress σ'_{vi}=2.25 MPa). From oedometer tests on undisturbed material (Lima, 2011), it is possible to determine a preconsolidation vertical effective stress $\sigma'_v{}^{max}$=5.2 MPa at the end of the deposition process that includes diagenesis and creep effects, resulting in an overconsolidation ratio *OCR*=2.3. Based on a drained friction angle of the natural material ϕ'=20° (Lima, 2011), the earth pressure coefficient at rest K_0 can be estimated as (Della Vecchia *et al*., 2010):

$$K_0^{SC} = (1-\sin\phi')\sqrt{OCR} \approx 1 \quad (1)$$

The mean effective stress at the *in situ* condition is:

$$p'_i = \frac{1}{3}\left(1+2K_0^{SC}\right)\sigma'_{vi} = 2.25MPa \quad (2)$$

On sample retrieval, total mean stress change is:

$$\Delta p = -p_i = -p'_i - u_{wi} \quad (3)$$

Assuming a constant mean effective stress ($\Delta p'$=0), the pore water pressure change on sample retrieval can be estimated as

$$\Delta u_w = \Delta p = -4.5\,MPa \quad (4)$$

$$u_{wf} = u_{wi} + \Delta u_w = -2.25\,MPa \quad (5)$$

where u_{wf} is the final pore water pressure after retrieval, which in principle should be similar to the initial suction measured under laboratory conditions.

In the case of Ypresian clay and following the same reasoning, the vertical stress and pore water pressure under *in situ* conditions are σ_{vi}=7.8 MPa, u_{wi}=4 MPa, σ'_{vi}=3.8 MPa. A vertical effective preconsolidation stress $\sigma'_v{}^{max}$=5.50 MPa was determined from oedometer tests (Piña, 2011), which results in an overconsolidation ratio *OCR*=1.4. An earth pressure coefficient at rest $K_0{}^{SC}$≈0.85 was estimated considering ϕ'=16º (Nguyen, 2011) that allowed determining the mean effective stress at the *in situ* condition p'_i=3.4 MPa. The pore water pressure change after sample retrieval can be estimated in Δu_w=-7.4 MPa, which results in a final pore water pressure u_{wf}=-3.4 MPa.

The final pore water pressures induced on stress relief should be compared with the initial suctions reported in Table 1. In the case of Boom clay, a

similar initial total suction was measured under laboratory conditions using psychrometers. For Ypresian clay, despite being retrieved at a larger depth, the measured initial total suction is somewhat lower (1.9 MPa). This fact is a consequence of the lower air-entry value of this clay, which will be discussed in the next section. This means that for Ypresian clay the final water pressure that was calculated based on stress relief considerations (u_{wf}=-3.4 MPa), cannot be sustained under saturated conditions (refer to Table 1, in which a somewhat lower degree of saturation is detected for the retrieved condition).

Table 1. Main properties of Boom and Ypresian clays.

Property	Boom clay	Ypresian clay
Density, ρ *(Mg/m^3)*	around 2.05	1.97 to 2.02
Dry density, ρ_d *(Mg/m^3)*	1.65 to 1.67	1.55 to 1.60
Gravimetric water content, *w (%)*	around 25	26 to 26.6
Initial total suction, Ψ *(MPa)*	2.0-2.5	1.9
Density of soil solids, ρ_s *(Mg/m^3)*	2.67	2.76
Void ratio, *e*	0.60 to 0.62	0.72 to 0.78
Porosity, *n*	0.37 to 0.38	0.42 to 0.44
Degree of saturation, *Sr (%)*	around 100	94 to 98
Liquid limit, w_L *(%)*	56	142 to 158
Plastic limit, w_p *(%)*	29	26
Plasticity index, *PI (%)*	27	116 to 132
Vertical water permeability, k_{wv} *(m/s)*	2.4 x 10^{-12}	6.6 x 10^{-12}

These high initial total suctions have important consequences on the hydro-mechanical response of these materials when subjected to stress levels below the *in situ* mean effective stress. Consider as an example Figure 2, which shows a stress-controlled isotropic loading –far below the *in situ* mean stress– on Boom clay under drained conditions. As observed in the figure, the clay underwent an important expansion despite being isotropically loaded and starting from an initial saturated state (Table 1). This expansion is a clear consequence of suction reduction effects due to water contact at low stress levels. To minimise these effects, the materials were always loaded to a total mean stress equivalent to the geostatic condition and only then put in contact with water under atmospheric pressure to restore *in situ* effective stress.

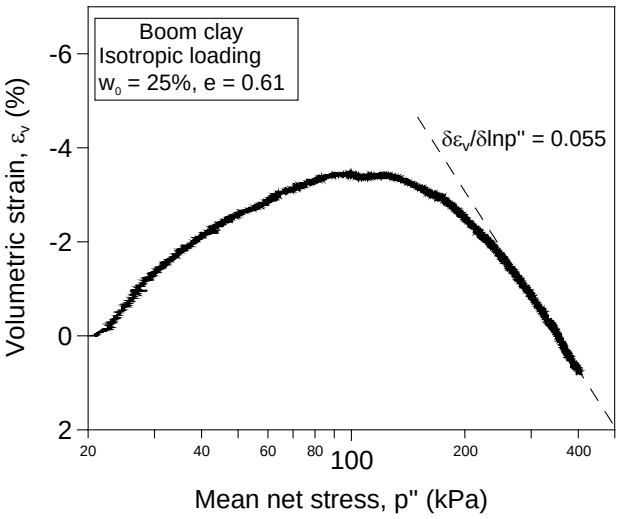

Figure 2. Isotropic loading on retrieved Boom clay under drained conditions. Sample put in contact with water at low stress levels.

Mercury intrusion porosimetry tests were performed using an 'AutoPore IV 9500 – Micromeritics Instrument Corp.' porosimeter to characterise the porosity network on freeze-dried samples –to preserve the pore structure–. Figure 3 presents the pore size distribution PSD curves of both clays. In the case of Boom clay, the plot shows one dominant pore mode at around 90 nm, as expected for a matrix type microstructure. On the contrary, Ypresian clay presents two dominant pore modes, one at 700 nm and another at 80 nm. This structural feature that has been consistently observed at different depths (Piña, 2011) is not typical for a deep clay formation, which has undergone a depositional sequence similar to Boom clay. Besides void ratio effects, this dual porosity has notable effects on the hydraulic response of Ypresian clay. On one hand, larger water permeability values are expected on Ypresian clay as indicated in Table 1, not only as a consequence of its higher void ratio but also due to its macroporosity features. On the other hand, water retention properties will be also affected, as discussed in the next section.

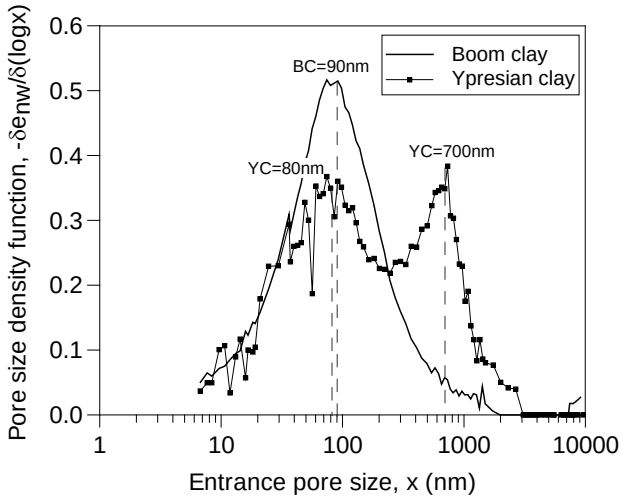

Figure 3. Pore size distribution curves of Boom and Ypresian clays.

2.2 Experimental programme

Laboratory tests were carried out on undisturbed material, which were trimmed (15 mm in diameter and 12 mm high) from retrieved Boom clay blocks and Ypresian clay borehole samples.

Water retention properties under unstressed conditions were first determined using chilled-mirror dew-point (WP4, Decagon Devices Inc, USA) and transistor (SMI, Australia) psychrometers. Details on the working principle of both psychrometers, as well as the different calibrations carried out, have been extensively described in Cardoso *et al*. (2007). The tests using WP4 were carried out following a multi-stage procedure, in which the same sample was first subjected to a main drying path and then to a wetting one. Only water content changes were measured along these multi-stage paths to avoid solid mass loss. During drying, samples were let to evaporate for one hour at controlled relative humidity (around 40%) and then allowed for equilibrating for one day under hermetic conditions and before taking the readings with the psychrometer. The total suction measuring time was around 10 minutes and water contents were determined using the initial and final masses (the sample holder is not completely tight to vapour losses). Wetting paths were performed by adding small drops to the sample. An equalisation period of one day under hermetic conditions was afterwards performed and before the determination of the total suction.

Boom clay results were complemented with vapour equilibrium technique using samples installed in hermetic jars. Partially saturated aqueous solutions of NaCl were used to apply different relative humidity values (Romero, 1999) below a total suction of 38 MPa. In the upper range, a saturated solution of $NaBr.2H_2O$ was also used to apply a total suction of 75 MPa (Delage *et al*., 1998; Romero, 2001). Multi-stage drying and subsequent wetting paths at the following steps 5, 10, 20, 38 and 75 MPa were carried out. At specific intervals of the equalisation process the mass of the sample was registered.

3 EXPERIMENTAL RESULTS

Figure 4 presents the time evolution of the changes in soil mass for Boom clay along the different wetting steps using vapour transfer under pure diffusion. As observed in the figure, longer equalisation periods are required for the lower total suction changes. Equalisation is reached after three weeks for the total suction step 10 to 5 MPa, whereas it is completed in less than one week for the total suction step 75 to 38 MPa. Similar results were reported by Merchán *et al*. (2011) on reconstituted Boom clay samples. These authors contrasted their experimental results using numerical simulations to study these longer periods required, in which a consistent trend was also obtained in the simulated results. Total suction equalisation depends on the vapour density (or mass fraction of vapour in gas) gradient, the exchange properties between the evaporating surface and the chamber atmosphere, and the material cross sectional area available for vapour to flow –volume of air to soil total volume, which is larger at the driest condition–.

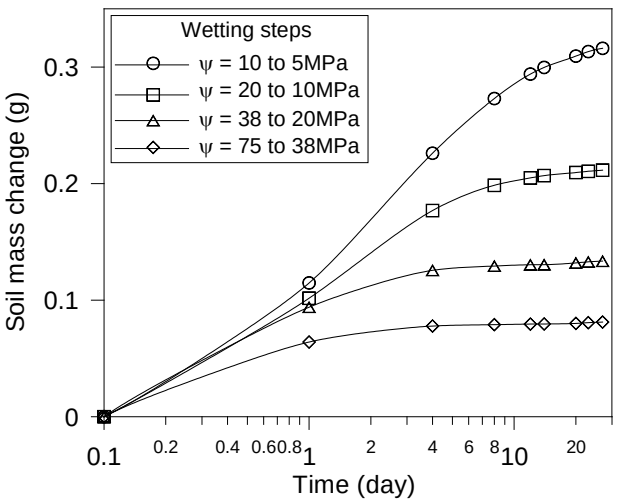

Figure 4. Time evolution of changes in Boom clay mass along wetting steps.

Figure 5 summarises the water retention results obtained on Boom clay. Generally speaking, a good consistency in the results using different techniques is observed. Nevertheless, vapour equilibrium and transistor psychrometer results systematically occurred below WP4 psychrometer readings. The systematic higher total suctions measured with WP4

psychrometer for given water contents can be explained in terms of the hydraulic paths undergone by the soil during the measurement process. As discussed by Cardoso *et al*. (2007), the sample placed inside the equalisation chamber of the WP4 psychrometer undergoes some drying along the suction measuring period, which can explain these systematic higher values.

Besides hydraulic hysteresis, volume change effects are also affecting the differences observed between drying and wetting paths. The low-suction zone of the retention curve (below 10 MPa) is dependent on void ratio and is consequently sensitive to the stress paths followed (Romero & Vaunat, 2000).

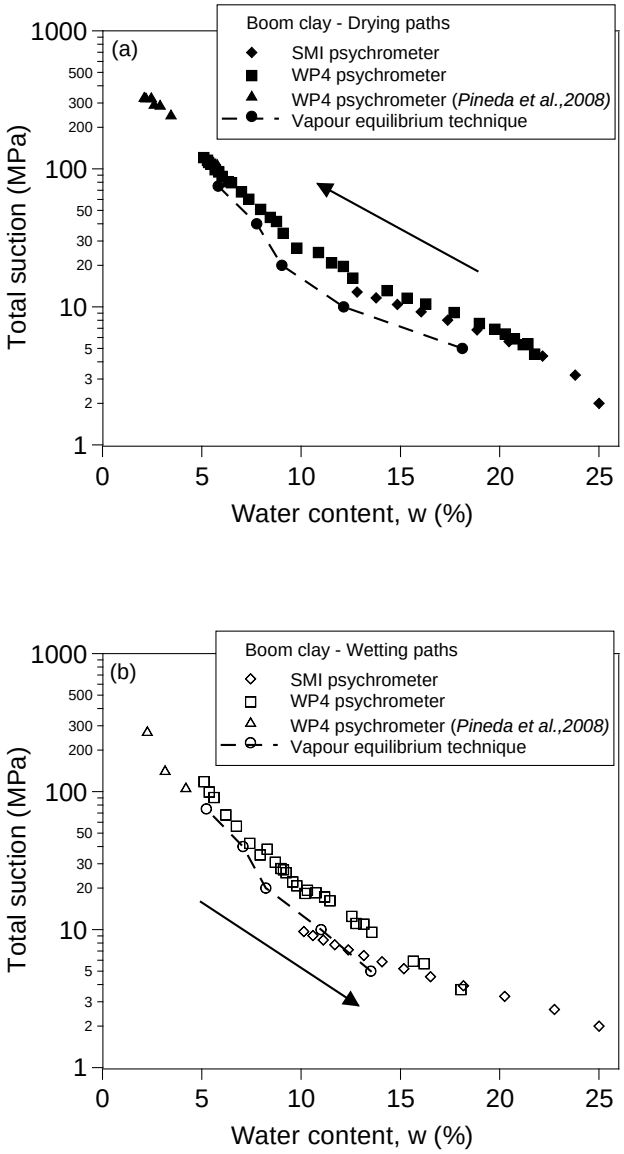

Figure 5. Retention curves of Boom clay using different techniques. (a) Drying paths and (b) wetting paths.

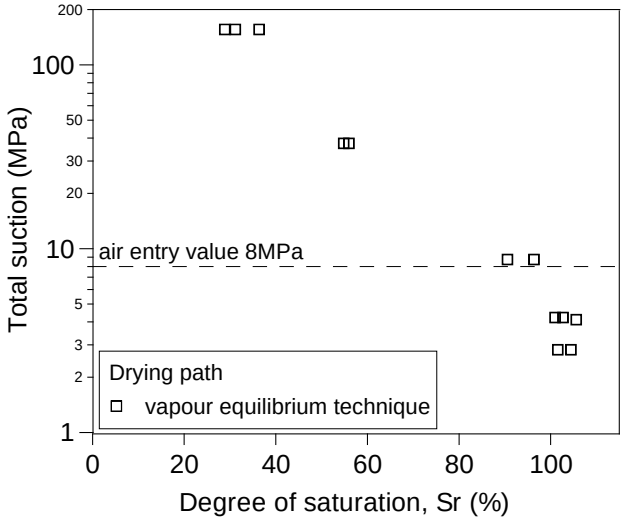

Figure 6. Retention curves of Boom clay in terms of degree of saturation using vapour equilibrium technique (Le *et al*., 2008).

As observed in Figure 5a and with reference to psychrometer readings on drying, important changes in water content occur when total suction is above 4 MPa, indicating some kind of air-entry value for Boom clay in terms of water content. Le *et al*. (2008) studied the water retention curve of undisturbed Boom clay in terms of degree of saturation. In their study, volume changes were measured along the hydraulic paths, displaying the results plotted in Figure 6. As observed in this figure, relatively high total suctions could be maintained without inducing appreciable desaturation on the material, suggesting a larger air-entry value in terms of degree of saturation. This aspect is a consequence of the shrinkage undergone by the material on drying. Despite losing water, the material also undergoes volume reduction, and a relatively high degree of saturation is still maintained at around 8 MPa (refer to Fig. 6).

Figure 7 shows the water retention curve of Ypresian clay compared to Boom clay obtained from WP4 psychrometer readings. As indicated in Table 1, the initial water content of Ypresian clay is slightly larger, which is also reflected at the starting point –water storage capacity at saturation– of the drying curve (Fig. 7a). Ypresian clay also presents a larger water retention capacity in both wetting and drying paths, as a consequence of the dominant smectite phase of the clay fraction. It also appears that Ypresian clay loses slightly larger water content (from the water storage capacity at saturation) when applying a total suction of 8 MPa (Fig. 7a). As also observed in this figure, at a total suction around 3 MPa, an early desaturation process seems also to occur on Ypresian clay. This desaturation process is associated with the double porosity network detected on Ypresian clay and its effects on air-entry value (Fig. 3). To better interpret the consequences of this double porosity structure, Figure 8 plots the

water retention curves estimated from mercury intrusion results and in terms of water content. In this case, the drying paths are assimilated to the non-wetting mercury intrusion (Romero & Simms, 2008). Boom clay displays an air-entry value consistent with the one estimated in terms of water content (Fig. 5a). Nevertheless, Ypresian clay presents a much lower air-entry value compared to Boom clay, as a consequence of the developed macroporosity. The air-entry value for Ypresian clay obtained from MIP and associated with macropores is around 0.4 MPa (early desaturations were also observed at a total suction around 3 MPa, as shown in Fig. 7a).

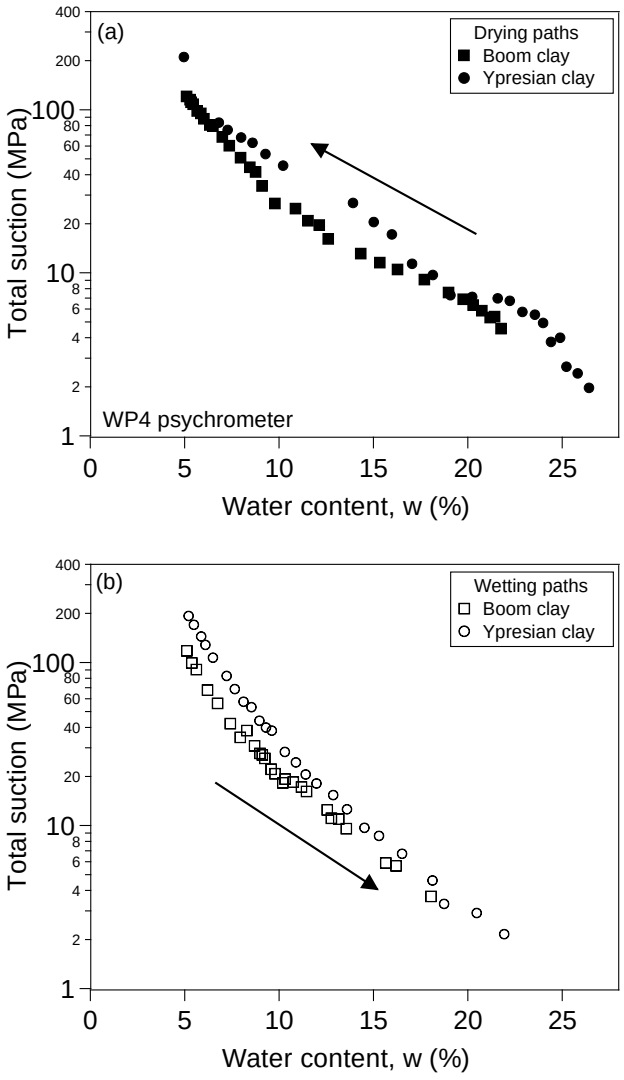

Figure 7. Comparison between water retention curves of Ypresian and Boom clays obtained from WP4 psychrometer. (a) Drying paths and (b) wetting paths.

The lower air-entry value of Ypresian clay affects the maximum total suction measured of the retrieved material. The estimated pore water pressure after retrieval is u_{wf}=-3.4 MPa (refer to section 2.1), which is higher (in suction terms) than the predicted air-entry suction and cannot be sustained under saturated conditions. The estimated degree of saturation corresponding to a total suction of 3.4 MPa is around 90% (lower than the degree of saturation reported in Table 1). The initial total suction reported in Table 1 of 1.9 MPa is consistent with the degree of saturation range indicated in Table 1. In the case of Boom clay, since the estimated water pressure after retrieval is -2.25 MPa (lower in suction terms than the estimated air-entry value), then this total suction can be sustained and the fully saturated condition maintained.

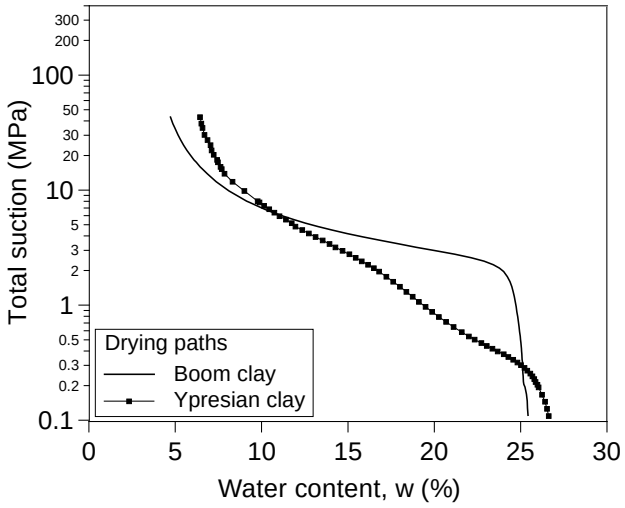

Figure 8. Water retention curves estimate from MIP data, comparison between Boom and Ypresian clays.

4 CONCLUSIONS

Two deep clay formations from Belgium, Boom clay (160 to 270 m deep) and Ypresian clay (300 to 450 m deep), are being investigated as host formations for disposal of high-level radioactive waste. The initial total suction is of importance when interpreting the state of the material after retrieval, which remains under nearly saturated conditions. These high total suctions affect the hydro-mechanical response of the materials, particularly at low stress levels (on water contact, the materials undergo swelling despite starting from nearly saturated state).

One important aspect to highlight is that both clays, which share a common depositional sequence, display quite different microstructural features. Boom clay displays a matrix type microstructure with dominant pore mode at around 90 nm. On the contrary, Ypresian clay presents two dominant pore modes, one at 700 nm and another at 80 nm, which have important consequences on the hydraulic response of the material.

The retention properties have been studied using psychrometer and vapour equilibrium techniques.

The consistent results on Boom clay show an air-entry value around 4 MPa when expressing water retention properties in terms of water content and slightly larger (around 8 MPa) when considering the volumetric variable degree of saturation. The difference between both values has been explained in terms of the shrinkage undergone by the material on drying, in which a relatively high degree of saturation is still maintained at around 8 MPa.

The macroporosity developed on Ypresian clay induces a lower air-entry value, despite being retrieved at a larger depth. The estimated pore water pressure after retrieval (-3.4 MPa) is higher (in suction terms) than the predicted air-entry suction and cannot be sustained under saturated conditions (early desaturations were observed at a total suction around 3 MPa, as shown in Fig. 7a). A total suction of 1.9 MPa is finally measured on Ypresian clay after retrieval (below the early desaturation suction of 3 MPa).

5 ACKNOWLEDGEMENTS

EIG EURIDICE (European Underground Research Infra-structure for Disposal of nuclear waste In Clay Environment, Belgium) and ONDRAF/NIRAS (Belgian Agency for Radioactive Waste and Enriched Fissile Materials) are gratefully acknowledged for funding the work presented in this paper.

6 REFERENCES

Cardoso, R., Romero, E., Lima, A. and Ferrari A. (2007). A comparative study of soil suction measurement using two different high-range psy-chrometers. Proc. 2nd Int. Conf. Mechanics of Unsaturated Soils. Weimar, T. Schanz (ed.). Springer-Verlag, Berlin, 79-93.

Coll, C. (2005). Endommagement des Roches Argileuses et Perméabilité Induite au Voisinage d'Ouvrages Souterrains, PhD Thesis, Université Joseph Fourier, Grenoble.

Della Vecchia, G., Lima, A., Jommi, C., Romero, E. (2010). Some remarks on the hydro-mechanical constitutive modelling of natural and compacted Boom clay. Proc. 5th Int. Conf. on Unsaturated Soils. Barcelona. Taylor and Francis Group, London, 803-809.

Delage, P., Howat, M. D. and Cui, Y. J. (1998). The relationship between suction and swelling properties in a heavily compacted saturated clay. Engineering Geology 50, 31-48.

Horseman, S.T., Winter, M.G., Entwistle, D.C. (1987). Geotechnical characterisation of Boom clay in relation to the disposal of radioactive waste. Final report. EUR10987. Luxembourg: Commission of the European Communities.

Le, T.T., Lima, A., Delage, P., Romero, E., Cui, Y.J., Gens, A., Tang, A.M., Li, X.L. (2008). Water retention properties of Boom clay. A comparison between different experimental techniques. Proc. 1st Eur. Conf. Un-saturated Soils – Advances in Geo-engineering. Durham, United Kingdom. Taylor and Francis Group, London, 229-234.

Lima (2011). Thermo-hydro-mechanical behaviour of two deep Belgium clay formations: Boom and Ypresian clays. PhD Thesis. Universitat Politècnica de Catalunya, Spain (in preparation).

Merchán, V., Romero, E., Vaunat, J. (2011). An adapted ring shear apparatus for testing partly saturated soils in the high suction range. Accepted for publication in in Geotechnical Testing Journal, ASTM.

Nguyen, X.P., Cui, Y.J., Tang, A.M., Li, X.L. (2010). THM behaviour of Ypresian clay. 3rd Ypresian clay meeting. Universitat Politècnica de Catlunya, December 2010, Spain.

ONDRAF/INIRAS (2005). The Ypresian clays as possible host rock for Radioactive Waste Disposal: an evaluation. Publication NIROND 2005-01.

Pineda, J., Lima, A., Romero, E. (2008). Influence of hydraulic paths on the low-strain shear modulus of a stiff clay. Proc. 1st European Conf. Unsaturated Soils – Advances in Geo-engineering. Durham, United Kingdom. Taylor and Francis Group, London, 519-523.

Piña, Y. (2011). Thermo-hydro-mechanical behaviour of Ypresian clay. Master's Thesis in Geotechnical Engineering. Universitat Politècnica de Catalunya, Spain (in preparation).

Romero, E. (1999). Characterisation and thermo-hydro-mechanical behaviour of unsaturated Boom clay: an experimental study. PhD Thesis. Universitat Politècnica de Catalunya, Spain.

Romero, E. (2001) Controlled suction techniques. Proc. 4º Simposio Brasileiro de Solos Nao Saturados. Gehling and Schnaid (eds.). Porto Alegre, Brasil, 535-542.

Romero, E. and Vaunat, J. (2000). Retention curves of deformable clays. Proc. Int. Workshop on Un-saturated Soils: Experimental Evidence and Theoretical Approaches, Trento, Tarantino & Mancuso (eds). Balkema, Rotterdam, 91-106.

Romero, E. & Simms, P.H. (2008). Microstructure investigation in unsaturated soils: A review with special attention to contribution of mercury intrusion porosimetry and environmental scanning electron microscopy. Journal of Geotechnical and Geological Engineering 26(6), 705-727.

APPENDIX B

TEMPERATURE CALIBRATION OF CONTINUOUS LOADING/UNLOADING OEDOMETER CELL FOR NON-ISOTHERMAL PATHS

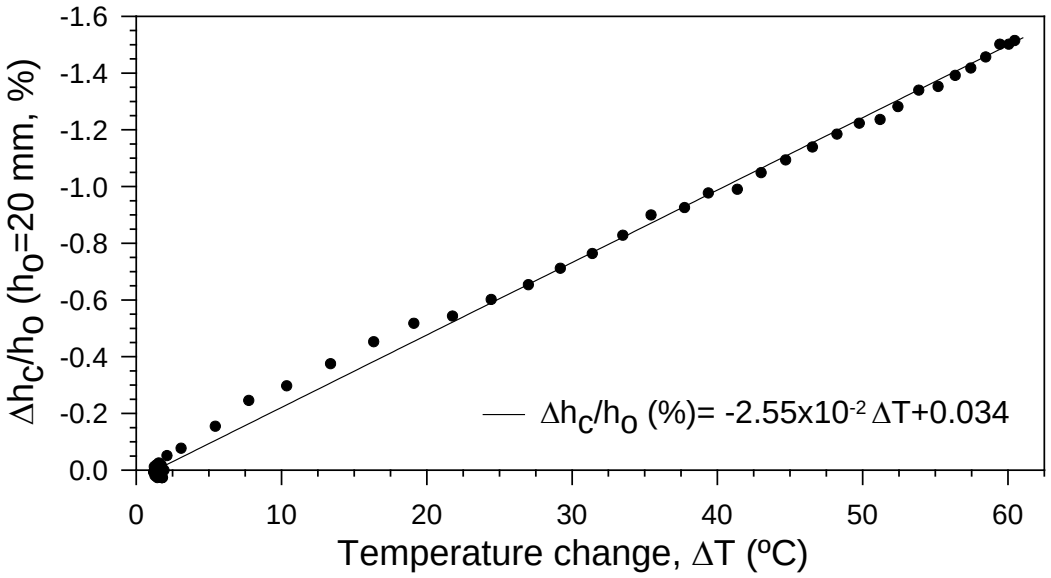

Figure B.1 Calibration for vertical thermal expansion of oedometer cell for non-isothermal paths.